SYNTHESIS OF ZINC OXIDE NANOPARTICLES BY AQUEOUS METHODS AND EFFECT OF METAL INCORPORATION ON THE STRUCTURAL/FUNCTIONAL PROPERTIES OF NANOPARTICLES

A THESIS SUBMITTED TO
THE GRADUATE SCHOOL OF NATURAL AND APPLIED SCIENCES
OF
MIDDLE EAST TECHNICAL UNIVERSITY

BY

ÖZLEM ALTINTAŞ YILDIRIM

IN PARTIAL FULFILLMENT OF THE REQUIREMENTS
FOR
THE DEGREE OF DOCTOR OF PHILOSOPHY
IN
METALLURGICAL AND MATERIALS ENGINEERING

DECEMBER 2014

Approval of the thesis:

SYNTHESIS OF ZINC OXIDE NANOPARTICLES BY AQUEOUS METHODS AND EFFECT OF METAL INCORPORATION ON THE STRUCTURAL/FUNCTIONAL PROPERTIES OF NANOPARTICLES

submitted by **ÖZLEM ALTINTAŞ YILDIRIM** in partial fulfillment of the requirements for the degree of **Doctor of Philosophy in Metallurgical and Materials Engineering Department, Middle East Technical University** by,

Prof. Dr. Gülbin Dural Ünver _____
Dean, Graduate School of **Natural and Applied Sciences**

Prof. Dr. Cemil Hakan Gür _____
Head of Department, **Metallurgical and Materials Eng.**

Prof. Dr. Caner Durucan _____
Supervisor, **Metallurgical and Materials Eng. Dept**., **METU**

Examining Committee Members:

Assoc. Prof. Dr. H. Emrah Ünalan _____
Metallurgical and Materials Eng. Dept., METU

Prof. Dr. Caner Durucan _____
Metallurgical and Materials Eng. Dept., METU

Assoc. Prof. Dr. Y. Eren Kalay _____
Metallurgical and Materials Eng. Dept., METU

Assoc. Prof. Dr. Emren Nalbant Esentürk _____
Chemistry Dept., METU

Assist. Prof. Dr. Hasan Akyıldız _____
Metallurgical and Materials Eng. Dept., SU

Date: 23.12.2014

I hereby declare that all information in this document has been obtained and presented in accordance with academic rules and ethical conduct. I also declare that, as required by these rules and conduct, I have fully cited and referenced all material and results that are not original to this work.

Name, Last name: Özlem Altıntaş Yıldırım

Signature:

ABSTRACT

SYNTHESIS OF ZINC OXIDE NANOPARTICLES BY AQUEOUS METHODS AND EFFECT OF METAL INCORPORATION ON THE STRUCTURAL/FUNCTIONAL PROPERTIES OF NANOPARTICLES

Altıntaş Yıldırım, Özlem
PhD, Department of Metallurgical and Materials Engineering
Supervisor: Prof. Dr. Caner Durucan

December 2014, 176 pages

Zinc oxide (ZnO) nanostructures have attracted considerable attention in many electrical, optoelectronic and magnetic applications due to their unique properties originating form characteristic wide band gap and large exciton binding energy of ZnO. Electrical, optical and magnetic properties of ZnO nanostructures strongly depend on their size and morphology. Therefore, there has been a strong interest in the synthesis of ZnO nanostructures with well-controlled size and shape. These synthesis approaches should allow morphological control and size modification for the resultant ZnO nanostructures. Meanwhile, simple experimental conditions without any sophisticate equipment requirements are critical for achieving economically feasible and large-scale production. The main objective of this study was to establish such synthesis routes for obtaining ZnO nanostructures. This study focuses on two main topics: (i) investigation of solution based synthesis methods for size and morphology controlled ZnO nanostructures and (ii) investigation of functional properties of ZnO nanostructures with silver (Ag) and copper (Cu) incorporation.

Synthesis of pure ZnO nanostructures was carried out using two different generic aqueous routes; microemulsion and precipitation. In microemulsion technique, ZnO nanoparticles were synthesized by using sodium bis(2-ethylhexyl)

sulfosuccinate:glycerol:n-heptane microemulsion system. The formation of ZnO nanoparticles was achieved after calcination of microemulsion products in air at various temperatures. Size and morphology of the nanostructures were controlled with applying different microemulsion formulations and calcination temperatures. Synthesis of ZnO nanoparticles was also achieved by low temperature precipitation method due to intrinsic yield problem of microemulsion approach. The precipitation system was formed using zinc acetate dihydrate as zinc source, ethylene glycol or water as solvent, and polyvinyl pyrrolidone as chelating agent. The size and shape of the ZnO nanoparticles were manipulated by the choice of precipitation temperature, amount of the chelating agent and type of the solvent, which essentially change the nature of adsorption events between ZnO crystals and organic molecules leading to changes in nucleation and growth events during precipitation.

The precipitation method was further expanded in order to realize chemical modifications of ZnO nanostructures for tailoring their functional properties. Both Ag and Cu doped ZnO (ZnO:Ag and ZnO:Cu) nanoparticles were synthesized by room temperature precipitation method without any subsequent thermal treatment. A rigorous structural analyses Rietveld and electron microscopy techniques have been performed on these chemically modified particles to explain the nature and mechanism of metal doping in ZnO crystal lattice. In addition, the effect of metal ion doping on the functional properties, such as photocatalytic activity (for ZnO:Ag) and room temperature ferromagnetism (for ZnO:Cu) have been demonstrated.

Keywords: Zinc oxide, microemulsion method, precipitation method, silver doped zinc oxide, copper doped zinc oxide.

ÖZ

SU BAZLI METOTLARLA ÇİNKO OKSİT NANO PARÇACIKLARIN SENTEZİ VE METAL KATKISININ NANO PARÇACIKLARIN YAPISAL/FONKSİYONEL ÖZELLİKLERE ETKİSİ

Altıntaş Yıldırım, Özlem
Doktora, Metalurji ve Malzeme Mühendisliği Bölümü
Tez Yöneticisi: Prof. Dr. Caner Durucan

Aralık 2014, 176 sayfa

Çinko oksit (ZnO) nano yapılar geniş bant aralığı ve yüksek elektron-hol bağ enerjilerinden kaynaklı özelliklerinden dolayı elektriksel, optik ve manyetik uygulamalarda yaygın bir kullanıma sahiptir. ZnO nano yapıların yapısal, optik ve manyetik özellikleri çoğunlukla bu parçacık boyut ve morfolojisine bağlıdır. Bu nedenle kontrollü ve tekrarlanabilir olarak ZnO nano yapıların sentezlenmesi büyük önem taşımaktadır. Söz konusu sentez yöntemlerinin, oluşturulan ZnO nano parçacıkların boyut ve şekil kontrolüne imkan vermesinin yanında, sofistike ekipman ve altyapı gerektirmeden uygulanabilir olması ekonomik olarak verimli ve yüksek miktarda üretim sağlanması açısından önemli diğer bir husustur. Bu çalışmada temelde konu edilen bu tür sentez süreçleridir. Çalışma genel olarak iki ana konuya odaklanmıştır; (i) boyut ve şekil kontrollü ZnO nano parçacıkların çözelti bazlı yöntemlerle sentezlenmesi, ve (ii) gümüş (Ag) ve bakır (Cu) katkılı ZnO nano parçacıkların sentezlenerek fonksiyonel özelliklerinin belirlenmesi.

Saf ZnO nano yapıların sentezlenmesi çözelti-esaslı farklı yöntemler kullanılarak gerçekleştirilmiştir; mikro emülsiyon ve çökeltme tekniği. Mikro emülsiyon tekniğinde ZnO nano parçacıklar sodyum bis(2-ethylhexyl) sulfosuccinate: gliserol:n-heptan sistemi kullanılarak üretilmiştir. ZnO nano parçacıkların oluşumu ısıl işlem

görmemiş mikro emülsiyon ürününün hava ortamında farklı sıcaklıklarda kalsine edilmesiyle sağlanmıştır. Nano parçacıkların boyut ve şekilleri farklı miktarda bileşen içeren mikro emülsiyon formulasyonları ve kalsinasyon sıcaklıkları uygulanarak kontrol edilebilmiştir. Mikro emülsiyon tekniğinin miktarsal anlamda verimsizliğinden dolayı ZnO nano parçacıklar, alternatif olarak çökeltme yöntemi kullanılarak da elde edilmiştir. Çökeltme sisteminde çinko asetat dehidrat çinko kaynağı, etilen glikol çözücü ve polivinil prolidon (PVP) ise şelatlama malzemesi olarak kullanılmıştır. ZnO nano parçacıkların boyut ve şekilleri çökeltme sıcaklığının seçimi, PVP miktarı ve kullanılan çözücü tipi ile kontrol edilmiştir. Bu değişkenlerin temel olarak çökeltme sırasında oluşmakta olan ZnO kristalleri ve organik moleküller arasındaki adsorpsiyon farklılaşmalara neden olduğu ve bunun sonucunda gerçekleşen farklı çekirdeklenme ve büyüme olayları sonucunda çökelen ZnO parçacıklar için boyutsal ve şekilsel değişimlerin sağlanabileceği ortaya konulmuştur.

Bu tezde ayrıca, çökeltme tekniği kullanılarak ZnO nano yapılar için bazı kimyasal modifikasyonların sağlanarak fonksiyonel özelliklerin değiştirilmesi yönünde çalışmalar yapılmıştır. Bu bağlamda, herhangi ek bir ısıl işlem uygulamadan oda sıcaklığında çökeltme yöntemi kullanılarak ZnO yapılara gümüş (ZnO:Ag) ve bakır (ZnO:Cu) katkılaması gerçekleştirilmiştir. Rietveld ve elektron mikroskop yöntemleri kullanılarak yapılan kapsamlı yapısal analizlerle her iki metal iyonunun ZnO kristal yapısına yerleşme mekanizması ve kristal yapıda oluşturdukları değişimler belirlenmiştir. Ek olarak, metalik iyon ilavelerinin ZnO'in foto katalitik aktivitesi (gümüş-katkılı durumda) ve oda sıcaklığında ferro manyetik (bakır-katkılı durumda) davranımı gibi fonksiyonel özelliklere etkisi gözlemlenmiştir.

Anahtar Sözcükler: Çinko oksit, mikro emülsiyon, çökeltme tekniği, gümüş eklenmiş çinko oksit, bakir eklenmiş çinko oksit.

To Mehmet and my lovely child Demir…

ACKNOWLEDGMENTS

I would like to express my gratitude to my supervisors Dr. Caner Durucan for his supervision, support, guidance and encouragement during this study. He trusted in me, gave the chance of doing independent research and helped me get over every obstacle on the way. I extend my sincere thanks to Dr. M. Vedat Akdeniz, Dr. Abdullah Öztürk and Raşit Turan for allowing me to use their lab facilities. I would like to thank Dr. H. Emrah Ünalan and Dr. Y. Eren Kalay for their intense help. I am thankful to Mehmet Yıldırım for their assistance in Rietveld refinement analyses.

I sincerely acknowledge to my colleagues; Betul Akkopru Akgun, Nusret Serhat Un, Onur Rauf Bingöl, Hakan Yavaş, Tümerkan Kesim, Gözde Alkan, Barış Alkan, and Ekim Saraç for making this long journey fun. I would also like to thank Hasan Akyıldız, Halil İbrahim Yavuz, Muratahan Aykol, Nagehan Duman, Nihat Ali Işıtman, Şahin Coşkun, Mine Kalkancı, Bahadır Can Kocaoğlu and Murat Güneş for their endless friendship. I am grateful to Cengiz Tan, Necmi Avcı, and Serkan Yılmaz for their significant technical support. I am thankful to METU Metallurgical and Materials Engineering Department for providing facilities for my research.

I am also thankful to my parents for their endless support throughout my lengthy education. Especially, I would also like to thank my love Mehmet Yıldırım for his understanding and support during all the years of my study. And my lovely kid Demir, now and after that, you are everything in my life.

This work was financially supported by DPT-ÖYP research funds and the scientific and technological research council of Turkey (TÜBİTAK), national scholarship programme for Ph.D. students (2211).

TABLE OF CONTENTS

LIST OF TABLES

TABLES

LIST OF FIGURES

FIGURES

LIST OF ABBREVIATIONS

ZnO	**:**	Zinc oxide
GaAs	**:**	Gallium arsenide
CB	**:**	Conduction band
VB	**:**	Valance band
UV-Vis	**:**	Ultraviolet-visible
E_g	**:**	Band gap energy
PL	**:**	Photoluminescence
TM	**:**	Transition metals
RTFM	**:**	Room temperature ferromagnetism
DSSC	**:**	Dye synthesized solar cells
LED	**:**	Light emitting diode
PVP	**:**	Polyvinyl pyrrolidone
AOT	**:**	Sodium bis(2-ethylhexyl) sulfosuccinate
Zn-Gly	**:**	Zinc glycerolate
EG	**:**	Ethylene glycol
XRD	**:**	X-ray diffraction
FESEM	**:**	Field emission scanning electron microscope
TGA	**:**	Thermogravimetric analyses
DSC	**:**	Differential scanning calorimetry
JCPDS	**:**	Joint committe on powder diffraction standards
EDX	**:**	The energy dispersive x-ray
HRTEM	**:**	High resolution transmission electron microscope
FTIR	**:**	Fourier transformed infrared spectroscopy
XPS	**:**	X-ray photoelectron spectroscopy
BE	**:**	Binding energy
H_c	**:**	Coercivity
M_s	**:**	Saturation magnetization

CHAPTER 1

INTRODUCTION

Metal oxide nanoparticles have attracted considerable attention in many scientific and technological applications due to unique properties originating from their particle sizes in nano scale. Zinc oxide (ZnO) is one of the well-known semiconductor metal oxide with wide direct band gap (3.37 eV) and large exciton binding energy (60 meV) at room temperature [1]. Reduction in size to nano scale, novel electrical, mechanical, chemical and optical properties are introduced to ZnO nanomaterials due to surface and quantum confinement effect [2]. These unique properties give ZnO several advantages as active material in the usage of gas sensors, solar cells, field effect transistors, light emitting devices [3-6].

Due to the specific needs in these diverse applications, there has been a strong interest in development of preparation methods enabling of production of ZnO nanostructures with well-controlled size and shape. Chemical vapor deposition, physical vapor deposition, spray pyrolysis, hydrothermal synthesis, sol-gel process, microemulsion method and solution precipitation method are the possible synthesis techniques of ZnO nanoparticles [7-12]. The techniques which are employed to synthesize ZnO should enable not only production of ZnO nanoparticles with different size and morphology, but also rely on experimental conditions, non-sophisticated equipments and low product cost. Microemulsion technique is especially attractive because it does not require sophisticated equipment or rigorous experimental conditions, but still providing possibilities in controlling the size and morphology of the particles in a size scale approaching to nanometers. This technique is based on the thermodynamically stable dispersion of two immiscible liquids which are oil and water. Stability of dispersion is provided by addition of surfactant molecules [11].

However, low product yield is the main disadvantage of microemulsion method. Therefore, aqueous precipitation method has attracted considerable attention due to its simple manipulation, low production cost and large scale production probabilities of ZnO nanostructures. These processing properties give some advantages over the other synthesis methods due to low energy consumption and providing the template free synthesis approaches which may lead to prevent incorporation of impurities and deterioration the optical/electrical properties of the ZnO particles [12]. However, only a few studies have been focused on room temperature synthesis of ZnO nanoparticles with well controllable size and morphology. So, one of the objectives of this study was exploring the potential of low temperature aqueous synthesis routes for obtaining ZnO nanoparticles.

ZnO can be functionalized by incorporation of various metal ions to control and change its functional properties. For example, ZnO nanostructures are also potential candidates for photocatalytic applications [13]. However, pure ZnO nanoparticles could not completely meet all of the needs of photocatalytic devices since they require high energy UV light to activate ZnO as catalysts leading to low efficiency in visible and near infrared regions. In order to solve this drawback, considerable efforts have been spent in improving photocatalytic ability by means of doping nanoparticles with noble metals such as silver (Ag) [14], as it has been also explored in this thesis.

Furthermore, when doped with small amounts of transition metals such as copper (Cu), ZnO shows room temperature ferromagnetism (RTFM), making it a dilute ferromagnetic semiconductor with properties that lead to potential applications in spintronic devices [15]. The origins of the RTFM are still under debate, even for doped ZnO nanoparticles. Therefore, there is an intense research interest on exploring RTFM behavior of Cu incorporated ZnO nanostructures and understanding the way in which Cu distribution affects both the semiconducting properties and also the room temperature ferromagnetic properties [16].

There are seven chapters in this thesis. It begins with the general introduction and structure of the thesis.

In the second chapter of the thesis, the history, basic properties, application fields and synthesis methods of ZnO are introduced. This chapter ends up with functionalizing of ZnO with doping various metals.

The third chapter of the study is on the synthesis of ZnO nanoparticles with different size and morphology by using a reverse microemulsion system. In studies, the effects of surfactant concentration, calcination temperature and solvent concentration on the size and morphology of the resultant ZnO nanoparticles were investigated. At the end of this chapter, a ternary phase diagram of microemulsion components according to morphological stable regions of microemulsion components has been presented.

In Chapter 4, aqueous precipitation method was employed for large scale production of phase pure ZnO nanoparticles at economically/technologically relevant conditions. The specific objective of this part is to determine the process parameters and the effects of precipitation temperature, solvent type and chelating agent concentration on the size and morphology of the resultant ZnO nanoparticles.

In the Chapter 5, Ag-doped ZnO nanoparticles were synthesized with room temperature precipitation method. The specific objection of this phase of the work is to synthesize Ag-doped ZnO nanostructures at room temperature by using aqueous system and to characterize and investigate photocatalytic properties of resultant ZnO nanostructures. The effects on the Ag amount on the structural, morphological, optical and so photocatalytic properties of ZnO nanoparticles are presented and discussed in detail.

In Chapter 6, we intend to explore the behavior of Cu-doped ZnO synthesized with simple room temperature precipitation method, and to understand the way in which Cu amount affects both the semiconducting properties and also the room temperature ferromagnetic properties.

Finally, this thesis is concluded in Chapter 7.

1.1 References

1. Markoc H., Ozgur, U., ZnO: Fundamentals, Materials and Device Technology **2009**, Weinheim, Germany, Wiley-VCH. p. 488.

2. Cauda V., Gazia R., Porro S., Stassi S., Canavese G., Roppolo I., and Chiolerio A., Nanostructured ZnO Materials: Synthesis, Properties and Applications, **2014**, Springer, Berlin, Heidelberg. p. 137-177.

3. Roy S. and Basu S., Bulletin of Materials Science, **2002** 25(6) p. 513-515.

4. Hagfeldt A., Boschloo G., Sun L., Kloo L., and Pettersson H., Chemical Reviews, **2010** 110(11) p. 6595-6663.

5. Zolper J.C., Solid-State Electronics, **1998** 42(12) p. 2153-2156.

6. Yungryel R., Tae-Seok L., Lubguban J.A., White H.W., Bong-Jin K., Yoon-Soo P., and Chang-Joo Y., Applied Physics Letters, **2006** 88(24) p. 241108.

7. Kołodziejczak-Radzimska A. and Jesionowski T., Materials (1996-1944), **2014** 7(4) p. 2833-2881.

8. Alexandrov S.E. and Hitchman M.L., Chemical Vapor Deposition, **2005** 11(11-12) p. 457-468.

9. Ayouchi R., Martin F., Leinen D., and Ramos-Barrado J.R., Journal of Crystal Growth, **2003** 247(3-4) p. 497-504.

10. Lee J.-H., Ko K.-H., and Park B.-O., Journal of Crystal Growth, **2003** 247(1–2) p. 119-125.

11. Li X., He G., Xiao G., Liu H., and Wang M., Journal of Colloid and Interface Science, **2009** 333(2) p. 465-473.

12. Chen C., Liu P., and Lu C., Chemical Engineering Journal, **2008** 144(3) p. 509-513.

13. Pearton S.J., Norton D.P., and Ren F., Small, **2007** 3(7) p. 1144-1150.

14. Georgekutty R., Seery M.K., and Pillai S.C., The Journal of Physical Chemistry C, **2008** 112(35) p. 13563-13570.

15. Pan F., Song C., Liu X.J., Yang Y.C., and Zeng F., Materials Science and Engineering: R: Reports, **2008** 62(1) p. 1-35.

16. Elilarassi R. and Chandrasekaran G., Journal of Materials Science: Materials in Electronics, **2010** 21(11) p. 1168-1173.

CHAPTER 2

LITERATURE REVIEW

2.1 General introduction

Zinc oxide with the chemical formula of ZnO is one of the well-known semiconductor material. For only 2014, with the key word ZnO, the data collections in Web of Science give more than 6000 scientific studies within the various research areas including physics, chemistry, nanotechnology and material science. However, this does not mean that ZnO is newly discovered material. The history of ZnO goes back to ancient age. The ancients discovered the production of the first brass-metal and the medical equipment's made with purified ZnO. In the last few decades, the interest in this fascinating chemical compounds remerges with the usage ZnO powder as an industrial processing chemical and a white paint pigment. In addition, for over one hundred years, polycrystalline form of ZnO has been used in a variety of applications such as electronic materials, gas sensors, cosmetic and pigment industry [1, 2]. The focused interest in this material started in the 1920s with the first utilization of ZnO for its semiconductor properties. With the discovery of attractive semiconductor properties of ZnO during 1950s, researchers focused on the bulk ZnO growth and applications [3]. During 1960s, synthesis of ZnO thin film has been extensively studied due to potential applications of ZnO thin film in the sensor and catalyst applications [4]. Since 1990s, a major research interest has been on the synthesis of ZnO nanostructures by different growth methods [5, 6]. Nowadays, the world wide afford in the fabrication of the high quality single crystal ZnO for the ZnO-based electronic and optoelectronic devices encouraged the researchers and provided to document hundreds of papers and patents every year since 2000.

ZnO is a wide bandgap semiconductor with bandgap energy of 3.37 eV which provides to operate in the blue and ultra-violet optical devices [7]. In addition, it has large exciton binding energy of 60 meV which gives ZnO several advantages over gallium nitride (GaN, 25 meV) such as better radiation resistance for devices used in space and nuclear applications and simpler and cost effective crystal growth methods [8]. Large exciton binding energy of ZnO provides to increase the exciton stability and enhance luminescence efficiency by increasing the possibility of radiative recombination. Gallium arsenide (GaAs) with a direct bandgap is another important semiconductor for high speed integrated circuits and optoelectronic applications like light emitting diodes and laser diodes [9]. However, GaAs is an unsuitable material for high temperature electronics and blue/ultra-violet light emitters [10]. Therefore, ZnO is a very interesting semiconductor and has been extensively used electronic and optoelectronic devices [11].

2.2 Basic properties of ZnO

ZnO is an inorganic compound which usually appears as a odorless white powder in the bulk form. In nature, mineral form of ZnO is zincite which contains impurity phases such as iron and manganese and appears as yellow or red according to impurity content [12]. The basic physical and chemical properties of ZnO are listed in Table 2.1.

Table 2.1. Basic physical and chemical properties of ZnO [13].

Property	**Value**
Molecular weight	81.37 g/mol
Melting point	1975 °C
Boiling point	sublimes
Solubility	0.16 mg/100 mL water (30 °C)
Stable phase at 300 K	wurtzite
Lattice parameters at 300 K	a: 0.32495 nm c: 0.50269 nm c/a: 1.602
Band gap energy	3.4 eV
Exciton binding energy	60 eV

2.2.1 Crystal structures of ZnO

ZnO is a II-VI type of binary semiconductor compounds which comprise the binary compounds of Zn, Cd and Hg with O, S, Se and Te. The most common crystal structure of the II-VI type binary semiconductor compounds are either the cubic zinc blende or hexagonal wurtzite structures. In these structures, each anion is surrounded by four cations at the corners of a tetrahedron, and vice versa. The tetrahedral coordination provides sp^3 hybridised covalent bonding character but all II-VI type binary semiconductor compounds have a partial ionicity, as well. ZnO has also ionicity between covalent and ionic semiconductors [14].

With the electronic configurations of Zn ($(1s)^2$, $(2s)^2$, $(2p)^6$, $(3s)^2$, $(3p)^6$, $(3d)^{10}$, $(4s)^2$) and O ($(1s)^2$, $(1s)^2$, $(2p)^4$), sp^3 hybridization of the electron states leading to tetrahedrally coordinated bonding character determines the crystal structure of ZnO. Indeed the tetrahedral geometry of ZnO results in a rather low space filling so it should be stabilized by the angular rigidity of the binding. In a crystal matrix, the arrangement of tetrahedrons consisting of zinc and oxygen layers may determine its crystal structure depending on the stacking sequence of zinc and oxygen layers.

The crystal structure of ZnO is shared by the wurtzite (B4 type), zinc blende (B3 type) and rock salt structure (B1 type) presented in Figure 2.1 (a), (b) and (c), respectively [11]. Although thermodynamically most stable phase is the hexagonal wurtzite structure at ambient pressure and temperature, ZnO crystallizes in zinc blende which forms only by growth on the cubic substrates and in rock salt which forms at high pressures. Zinc-blende structure may be considered as an arrangement of two interpenetrating face centered cubic sub-lattice structures. Hexagonal wurtzite lattice is uniaxial and its distinct axis, c, is directed through one of the tetrahedral binding orbitals. This means that hexagonal c axis behaves as a body diagonal axis of the cubic structure. Contrary to other II–VI type semiconductors like ZnS which can be stable in both zinc blende and the hexagonal wurtzite-type structures, ZnO mainly prefer to crystallize in the form of the hexagonal wurtzite-type crystal structure at ambient pressure and temperature [16].

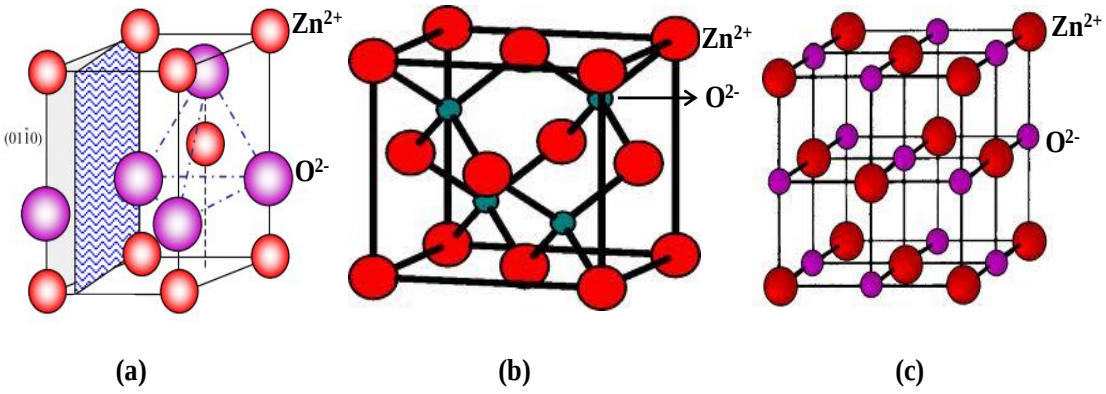

Figure 2.1. Line and ball representation of ZnO structures: (a) hexagonal wurtzite, (b) zinc blende and (c) rock salt [11, 15].

Ideally, ZnO with wurtzite structure has two interpenetrating hexagonal-close-packed sublattice which consists of one kind of atom (group II atom) is surrounded by the other kind of atom (group VI atom) along the threefold c-axis. In this structure, the primitive translation axis, a and b, locate at x-y plane with the angle of 120° and c lies in the z-axis. At room temperature, the values of primitive translation vector are 3.249 Å for a and b and 5.206 Å for c. The ratio c/a of the elementary translation vector is 1.602 and it deviates slightly from ideal value of 1.633 which belongs to the point group in the various notations 6 mm or C_{6v} and the space group $P6_3mc$ or C^4_{6v} [17]. Furthermore, in a real crystal, the u parameter (which is a measure of the amount by which each atom is displaced with respect to next atom through to the c axis) also deviates from ideal value ($u=(1/3)*(a^2/c^2)+(1/4)=0.379$) by changing c/a ratio. Therefore, ZnO crystals deviate from ideal structure by changing c/a value and u parameter. In addition, there is a strong relationship between the c/a value and u parameter, as the c/a value decreases the u parameter increases, so, four tetrahedral distances are kept roughly constant in the lattice by means of the change of the tetrahedral angles because of the long-range polar interactions [11].

The deviation from the ideal wurtzite structure depends on the change of the lattice parameters which are affected by

- the concentration of the free electron which changes conduction band (CB) levels occupied by the these electrons,
- the concentration of the impurity or doped atoms due to differences of the ionic radii with host matrix,
- external strains due to growth substrate and
- temperature.

The tetrahedral structure of the hexagonal wurtzite structure of ZnO, which forms with two interconnecting sublattices of Zn^{2+} and O^{2-}, causes the polar symmetry. The structure contains four common face terminations;

Basal crystal faces

1. catalytically active Zn-terminated polar top surface (0001), with the surface energy of 4.0 J/m^2 and
2. catalytically inert O-terminated polar bottom surface $(000\bar{1})$, with the surface energy of 4.0 J/m^2,

Prismatic crystal faces

3. nonpolar surface of $\{11\bar{2}0\}$ with the surface energy of 2.0 J/m^2 and
4. nonpolar surface of $\{01\bar{1}0\}$ with the surface energy of 2.32 J/m^2 [18, 19].

The polarity of ZnO structure due to different chemical activity, stability and surface energy of the surfaces is responsible for the various properties such as piezoelectricity and spontaneous polarization. In addition, these differences in the surface polarity also affect the crystal growth and defect generation and they are the key factors in nano-micro crystal growth process [20]. The oppositely charges Zn-terminated top surface and O-terminated bottom surface form a dipole moment in the each unit cell perpendicular the basal plane and so give rise to spontaneous polarization along the c-

axis of the crystal. This polarization causes to instability of the polar surfaces of the ZnO crystal and can be eliminated by

- adsorption of the impurity or doping atoms,
- surface reconstruction,
- surface relaxation,
- get rid of surface atoms,
- reorganization of the electronic structure and
- deformation of the crystal along the polar axis.

2.2.2 Electronic band structures of ZnO

Due to their principal technological applications like optoelectronic field and heterogeneous catalysis, the electronic band structure of the ZnO is important to be understood for its utility in devices and for further improving the performance of these devices [21]. Several experimental techniques such as angle resolved photoelectron spectroscopy, x-ray induced photo absorption and photoemission spectroscopy have been commonly used to understand the electronic band structure of ZnO [22-25].

The band structure of ZnO has been also explored by the theoretically studies by a number of groups using the local density approximation (LDA) with standard self-interaction-corrected [24] or atomic self-interaction-corrected pseudo potentials (SIC-PP's) [26]. In the LDA band structure determining techniques, Zn 3d electron positions are very crucial since if the d electrons are treated as core electrons, calculated lattice constants are 18% far from the experimental values for ZnO. However, if the d electrons are truly taken into account, the band gap can be miscalculated or d electron positions can be different than the determined from the experimental studies.

Vogel et al. reported ab initio calculations of electronic properties of ZnO by using the SIC-PP's band structure determining technique [26]. They reported that band structure was along the high symmetry lines in the hexagonal Brillouin zone presented as in

Figure 2.2. They also showed that the valance band (VB) maxima and conduction band (CB) minima fit into one another at Γ point which indicates that ZnO is direct band gap semiconductor.

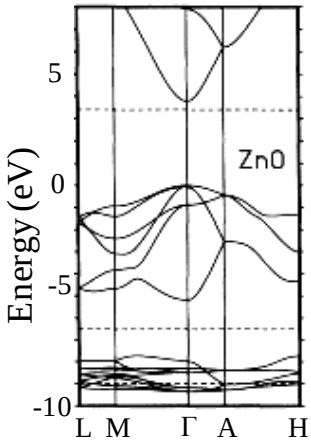

Figure 2.2. Band structure determination of ZnO with LDA using SIC-PP [26].

In Figure 2.2, Zn 3d bonding state appears at around -9 eV (the bottom 10 bands), O 2p energy level emerges from -5 eV to 0 eV (middle 6 bands) and the first two CB correspond to empty Zn 3s bonding state. Therefore, the band gap of ZnO was determined as 3.37 eV by theoretical calculations with LDA using SIC-PPs and this was close to experimental value (3.3 eV) [27]. The difference is probably due to failure in modeling Zn 3d electron levels.

2.2.3 Optical properties of ZnO

The optical properties of a given semiconductor is critical in determining its potential utility. Therefore, a detailed knowledge of the band structure is important if the semiconductor is considered as in a family members of the materials for device applications. The optical properties of ZnO are influenced by the energy band structure and altered with both intrinsic and extrinsic transitions [28, 29]. Although intrinsic transitions take place between CB electrons and VB holes, extrinsic transitions are connected with the discrete electronic states which found between VB and CB and created as a result of the electronic state of dopants or defects. The electronic states of

excitons which can be bound with neutral or charged acceptor or donor states of dopants or defects depend on the band structure of the host semiconductor material. These discrete electronic states influence absorption and emission process and thus, influence final optical properties of ZnO. Figure 2.3 shows electron energy level diagram of copper doped ZnO nanowires and effect of the defect and dopant energy states on the band gap of the ZnO. Various groups have studied the optical properties of ZnO by means of a variety of the experimental techniques like ultraviolet-visible (UV-Vis) spectroscopy [30], photoluminescence (PL) spectroscopy [31] and calorimetric spectroscopy [32].

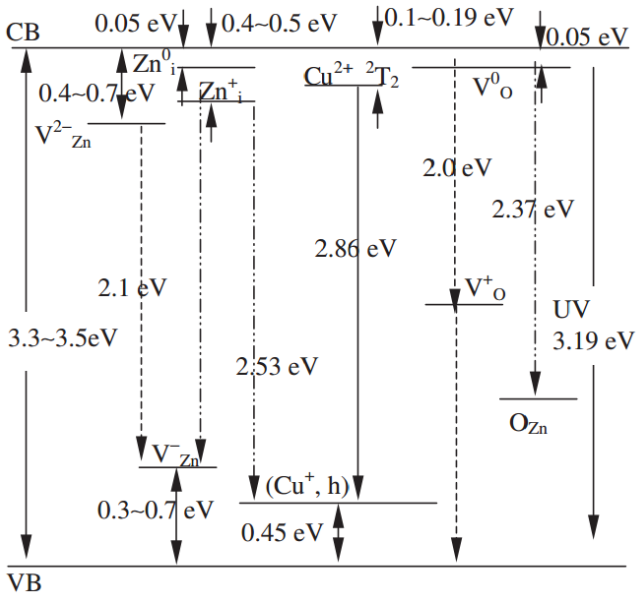

Figure 2.3. Schematic diagram of electron energy level band diagram of the defects in the Cu doped ZnO nanowires [33].

UV-Vis spectroscopy of ZnO is the measurement of the near and ultraviolet light absorbed by ZnO and presents an absorption band located at the wavelength of 360 nm [34]. Band gap energy (E_g) value of ZnO depends on the location of the adsorption band edge. It is obtained by plotting the absorption coefficient (α) – photon energy (hυ) graph and extrapolating the straight-line portion of this plot to the hυ axis. E_g value of ZnO is determined as 3.37 eV which makes ZnO a suitable material short wavelength photonic applications required UV or blue spectral range.

It can be tunable by decreasing particle size or doping with various cations. A reduction of E_g value of ZnO is observed in the case of decreasing particle size [35] or doping with various cations. Aravind et al. reported that E_g value of Cu doped ZnO changes from 3.30 eV to 3.19 eV with increase in Cu amount [36]. This red shift in the E_g value can be explained with the sp-d spin-exchange interactions between the localized d electrons of incorporated transition metal ions and band electrons of host semiconductors. Figure 2.4 shows the change of the E_g values of ZnO nanostructures with particle size and incorporated Cu amount.

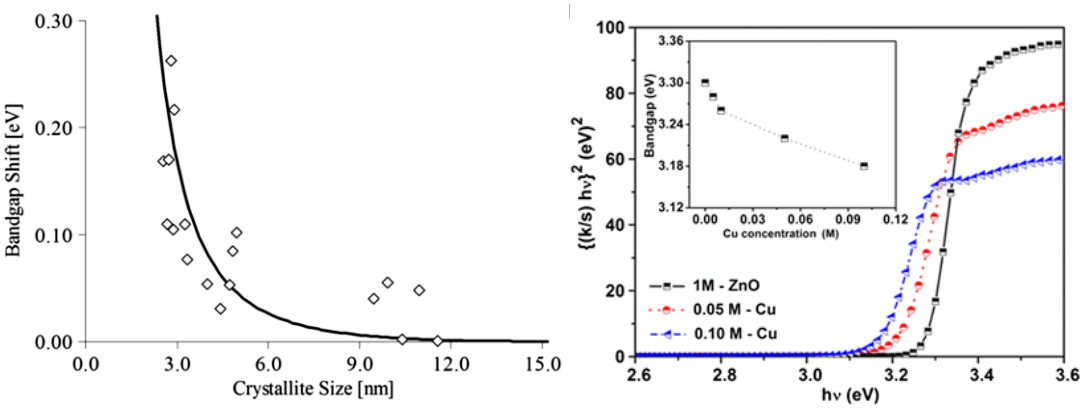

Figure 2.4. The change of the E_g values of ZnO nanostructures with particle size [37] and incorporated Cu amount [36].

PL spectroscopy measurements give information about not only optical properties but also defect structure of ZnO. Earlier works presented that ZnO exhibits three PL bands centered at 390, 510 and 640 nm labeled at UV, green and orange emission, respectively. UV emission is related with the direct recombination of excitons [38], green emission is attributed to oxygen vacancies [39] and yellow emission is associated with oxygen interstitials [40].

Wei et al. reported that the optical properties of ZnO can be improved with controlling the size and morphology of ZnO nanorods through a wet chemical method [41]. They found that crystal quality also affect the final optical properties of ZnO. In a related study, reducing density of defects of ZnO prisms results in a decrease in the

recombination center of defect and so, high intensity of the UV emission band and low intensity of the visible emission band in photoluminescence spectra [42] are obtained.

2.2.4 Magnetic properties of ZnO

The control of the spin in magnetic materials along with electron charges of semiconductors appears promising for a new class of devices; spintronics devices. A key requirement in this devices is that host material should be ferromagnetic at room temperature. Furthermore, they should have efficient spin-polarized carrier injection and transport. Therefore, to achieve spin injection into these materials is developing new class of materials; diluted magnetic oxides (DMS). As magnetic atoms, transition metals (TM) (Ti, Cr, Mn, Co, Fe, Ni and Cu) have been used due to their partially filled d states.

Most of the earlier work on DMSs has been on III-V type semiconductors, which have low solubility for TM [43, 44]. More recently, II-VI type TM-incorporated semiconductors have been explored, as they allow high dopant concentrations and exhibit potential in achieving magnetic ordering at around ambient temperatures [45, 46]. Among various II-VI type semiconductor metal oxides, ZnO has provoked great interest as a DMS due to its wide band gap (3.37 eV) and large exciton binding energy (60 meV) [47]. In addition, both the theoretical predictions and experimental studies indicated that TM-incorporated ZnO has RTFM property with a curie temperature above room temperature (300 K) [48, 49].

2.3 Application fields of ZnO

Due to its unique properties, ZnO is widely used in a wide range of applications ranging from cosmetics to optoelectronic devices. General application fields and a worldwide consumption, nearly 10^5 ton per year, of ZnO are shown in Figure 2.5. General application fields can be classified as;

- electronics and electrotechnology industries (gas sensors, solar cells, field effect transistors, light emitting diodes, varistors and spintronic devices),
- photocatalyst industry,
- textile industry,
- rubber industry,
- pharmaceutical and cosmetic industries

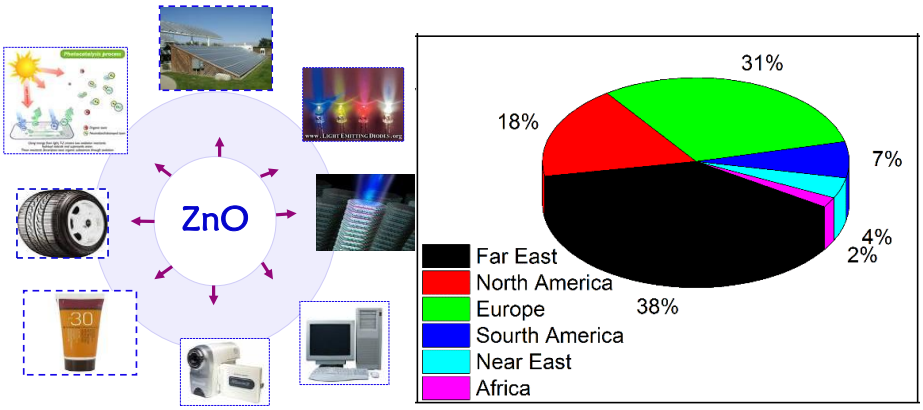

Figure 2.5. General application fields of ZnO and worldwide consumption diagram of ZnO [50].

2.3.1 Electronic and optoelectronic applications of ZnO

ZnO is widely used material in many different electronic and optoelectronic industries including gas sensors, solar cells, field effect transistors, light emitting diodes, varistors and spintronic devices.

2.3.1.1 Gas sensors

Since the atmospheric air contains various type of the chemical species, some of which are vital but many others are harmful to living organisms. After the first time demonstration of gas sensing property of germanium in 1953 [51], researchers have been focused on the semiconductor-based gas sensing materials. After the famous lecture of Feymann's in 1959 "There's plenty room at the bottom", researchers studied on the gas sensors have focused on the new opportunities in nano-scale materials. With the high surface-to-volume ratio, nanosensors made with non-porous and uniform sized nanoparticles or thin films potentially perform better gas-sensor signals due to better interaction of gas molecules with the surface of the semiconductor metal oxides. Later on 1962, ZnO was reported as new alternative for gas detector.

ZnO is attracting significant attention in chemical and environmental sensor applications because their nature and concentration of adsorbed species on their surfaces effects their electrical conductivity. Oxygen vacancies formed in ZnO structure are responsible for the observed high sensitivity of the electrical properties to the presence of adsorbed molecules and allow the tuning of the conductance of the oxide. The unique ability to form a variety of nanostructures such as nanowires, nanocombs, nanorings, nanobelts makes ZnO attractive material for gas sensing applications such as hydrogen, ethanol, ammonia and acetone [52-55]. It is also used for detection of CO and CO_2 gases in mines and alarm equipments [56]. Figure 2.6 shows NH_3 gas sensing mechanism of an individual ZnO nanowire in air and in an NH_3 environment [57].

The sensitivity of gas sensors can be improved by controlling the grain size and porosity of the ZnO; smaller sized ZnO nanoparticles with controlled porosity is preferred for the gas sensor applications [58, 59]. Therefore, to control particle size and porosity, synthesis method of ZnO nanostructures is important for the determining final sensitivity of the gas sensor.

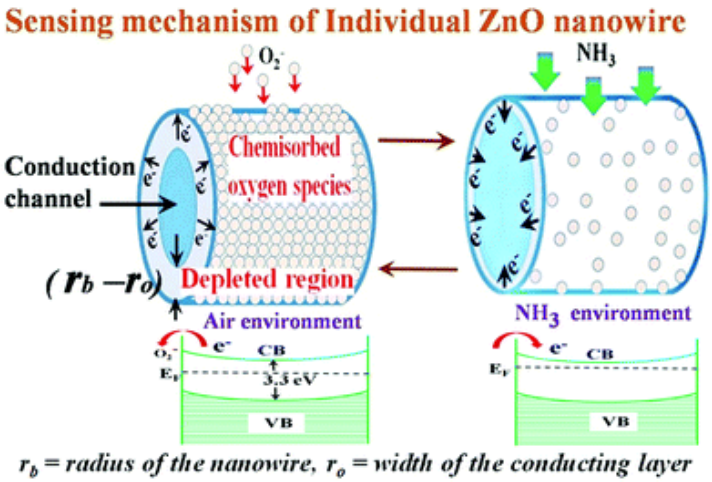

Figure 2.6. NH_3 gas sensing mechanism of an individual ZnO nanowire in air and in an NH_3 environment [57].

2.3.1.2 Solar cells

Solar cell is an electronic device which directly converts sunlight into electricity. The working principle of solar cell device is based on the photovoltaic effect. A well-known photovoltaic device is the single-crystalline silicon solar cell which operate on the principle of the p-n junctions. However due to high material cost of the single-crystalline silicon solar cell, thin film solar cells have been studied worldwide. With the development of the dye synthesized solar cells (DSSCs), the usage of the ZnO based DSSCs has extensively increased since although lower conversion efficient (0.4-5.8 %) than that of 11% for TiO_2, easily crystallization and anisotropic growth makes ZnO a distinguished alternative to TiO_2 [60]. Figure 2.7 indicates the schematic illustration of typical ZnO based solar cell.

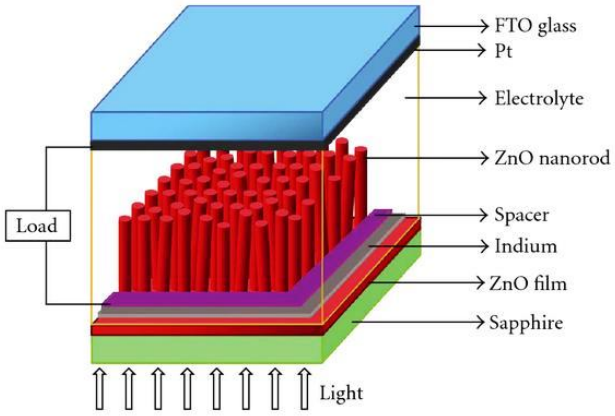

Figure 2.7. A schematic illustration of typical ZnO based solar cell [61].

ZnO film based solar cells show an improvement solar cell efficiency from 2% to 5% by means of a controlled dye-sensitization procedure with avoiding dye-aggregation [62]. Morphology of ZnO nanostructures used in DSSC is also important for the overall device efficiency. Ko et al. reported that special nanoforest morphological ZnO nanostructures with high density, long branched treelike nanowires show a significantly improved DSSC power conversion efficiency and five times higher light conversion efficiency than that of ZnO nanowires [63].

2.3.1.3 Light emitting devices

A light emitting diode (LED) is a device which emits visible light during the passing electric current through it. The light in most LEDs is monochromatic (single wavelength). However, the output of LED can have a wavelength in the range from red to blue-violet. A led consists of p- and n- type semiconductors which are placed in direct contact to each other and form p-n junction. Therefore, the LED can allow visible or IR energy to pass through. Low power requirement, high efficiency, fast switching time, long life, remote control and LCD panel backlighting are the advantages of LEDs over the classical fluorescent illumination.

ZnO based heterestructure LED was fabricated in 1969 by Drapak [64]. After that, ZnO-based heterestructures have great interest due to its large excition binding energy.

As a wide bandgap semiconductor, ZnO has substantial advantages in ultraviolet LEDs, laser and electronic devices working at high temperature operations due to its high exciton binding energy, tunable bandgap, chemical stability and opportunity to produce large and high quality single crystal wafers [65]. Figure 2.8 shows a schematic illustration of the structure of the ZnO-based UV LED devices employing in the presence of a BeZnO/ZnO active layer.

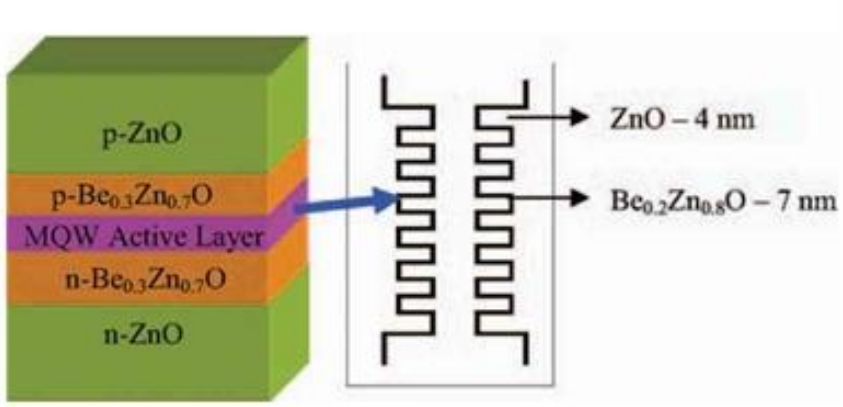

Figure 2.8. A schematic illustration of the ZnO-based UV LED devices [66].

An important issue to fabricate high quality LEDs is the structural similarity between the semiconductors forming the heterojunctions since lattice mismatch can cause the defect formation which deforms p-n junction interface by forming non-radiative centers. Therefore, ZnO-GaN heterostructure is attractive because lattice parameter of GaN has very close lattice parameters to ZnO (the lattice mismatch ~1.8%). In addition their E_g values are similar (E_g: 3.3 (ZnO) and 3.4 (GaN)) [67].

2.3.1.4 Varistors

A varistor is an electronic ceramic device with an electrical resistivity which changes with the applied voltage. Its primary function is to sense and limit transient voltage surges without being destroyed. It can be used both in ac or dc fields and over a wide range of voltages, from a few volts to tens of kilovolts, and a wide range of currents, from microamperes to kiloamperes.

Varistor technology is one of the most important application of ZnO in electronics. The primary function of ZnO varistors is to sense and limit transient voltage surges and to do so repeatedly without being destroyed. Chemical composition as well as the processing techniques used to synthesize the varistor have effect on the electrical characteristics of a varistor. Porosity and inhomogeneous distribution of particles in a varistor cause the formation of hot spots so failure of the varistor occurs at a lower current density than the expected value. ZnO varistors are known as voltage limiters, nonlinear resistors, variable resistors, surge suppressors and surge protectors. In varistors, after spherical ZnO powders are mixed with the powders of other oxides such as those of Bi_2O_3, Sb_2O_3, MnO, CoO and Cr_2O_3, conventional pressing and sintering techniques are applied to the powder compacts [68]. Nonlinear characteristic as well as the range of voltage and current over which the device can be used is far superior to those of SiC based devices makes ZnO the most popular nonlinear resistor prior to the advent of the ZnO varistor.

Synthesis method of ZnO is important to fabricate a good quality varistor. Spherical ZnO particles prepared with aqueous precipitation method have been shown to be suitable for varistor applications due to uniform size distribution [69]. Singhal et al. reported that size of precursor ZnO particles affects the critical voltage of varistor [68]. They found that smaller sized particles decreases critical voltage since reducing grain size allows increasing grain boundary per unit volume and so improves breakdown voltage. Microemulsion technique has some advantages for varistor application since it provides to possibility of *i*) prevention of contamination, *ii*) precise control over stoichiometry, *iii*) surfactant act as source of metal ions and *iv*) precise control size of nanoparticles.

Another important factor to improve varistor performance is homogeneously distributed dopants throughout the grain boundary [70]. This can be achieved by the usage of the particles in the nano scale. However, dopant concentration should be below the certain limit because the dopants concentrations were increased, the electrical properties including coefficient of nonlinearity and breakdown voltage slowly deteriorated.

2.3.1.5 Spintronic devices

New generation information processing devices is an advanced form of the electronic devices based on the both electronic charge and spin movement of electrons. This type of devices is called “spintronic device”, which is a combination of standard microelectronics and magnetic properties of the material. The advantages of spintronic device are nonvolatility, high speed of data processing, low electric power consumption. Requirements of the spintronic device are the ferromagnetic property of the host material above the room temperature, efficient spin-polarized carrier injection and transport. Among the wide band gap semiconductors, ZnO has advantage due to providing charge, photonic and spin-based functionality. In addition, room temperature carrier-mediated ferromagnetism is another advantage of ZnO obtained by means of doping with several transition metal such as Mn, Cr, Ni and Cu. Figure 2.9 shows a schematic illustration of the spin solar cell.

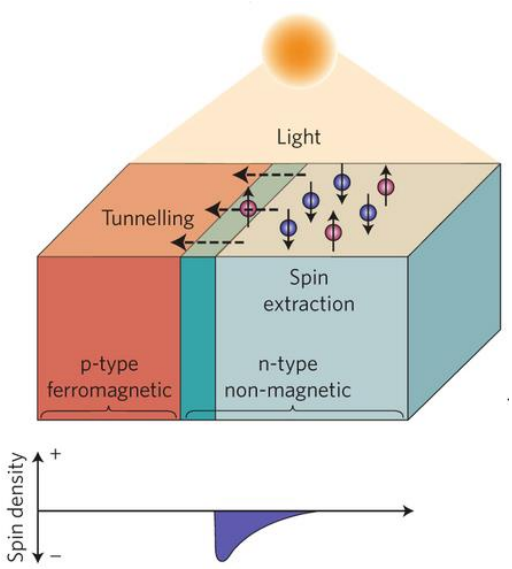

Figure 2.9. A schematic illustration of the spin solar cell [71].

2.3.2 Photocatatytic applications of ZnO

In the past of few decades, many researchers have studied the production of semiconductor oxide nanoparticles for the application of photocatalytic devices. The mechanism of photocatalytic devices based on the acceleration of a photoreaction of

catalyst, which is usually semiconductors with wide band gap, in the presence of solar energy. The photocatalytic ability of semiconductors is determined by the ability to create electron-hole pairs under photo illumination. For photocatalytic irradiation, sunlight is abundantly available as natural energy source and its energy can be conveniently exploited for the irradiation of semiconducting materials. UV irradiation is another energy source for degradation of organics.

Neppolian et. al. reported that while solar energy is a cost effective light source due to its abundance and non-hazardous nature, the UV irradiation can bring better efficiency in the degradation of textile dyes [72]. When semiconductor nanocrystals are illuminated with UV energy not less than the band gap energy of semiconductor, they produce holes in the VB and electrons in the CB [73]. Photocatalytic reactions take place on the surface of semiconductor nanocrystals when these charge carries reach the crystal surface and react with adsorbed molecules. A schematic representation of the photocatalytic reaction is shown in Figure 2.10.

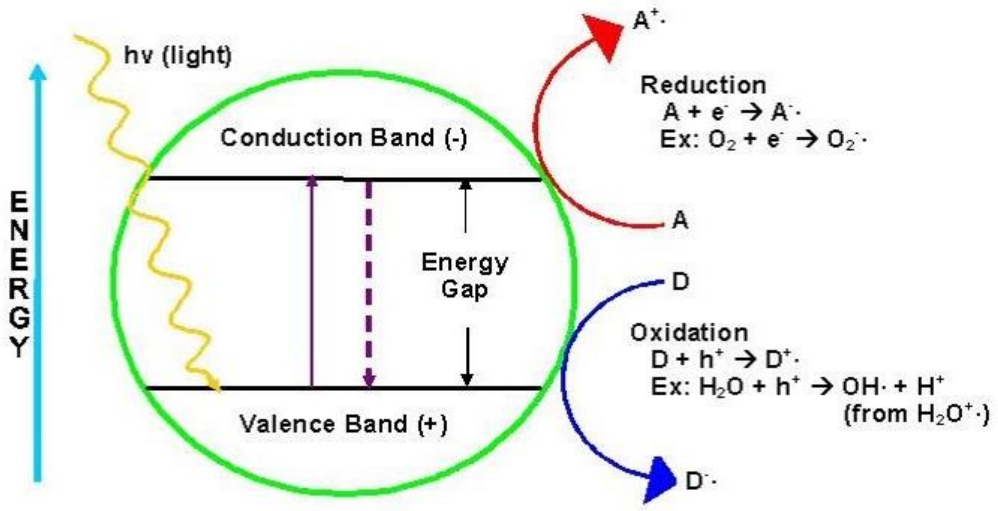

Figure 2.10. A schematic representation of the photocatalytic reaction of semiconductors [Retrieved from:http://www.smita-iitd.com/research-highlights/self-cleaning-finish/Last accessed on 12.12.2014].

With the irritation of the semiconductor surface by light which has equal or higher energy than the band gap of semiconductor, a photo excited VB electron is promoted to the CB so that it leaves a hole behind the VB. For the photocatalytic degradation of a various environmental contaminants, TiO_2, ZnO, ZrO_2, Fe_2O_3, CdS and ZnS have been used. Among various semiconductor materials TiO_2 and ZnO have been recognized as the two most active catalysts due to their wide band gap and widely used in the removal of toxic, harmful or hazardous organic pollutants [74]. As a comparison, ZnO has more attention due to similar band gap energy (3.37 eV) and lower cost than TiO_2.

However, simple ZnO nanoparticles could not completely meet all of the needs of devices since photocatalytic devices require high energy UV light to activate ZnO as catalysts leading to low efficiency in visible and near infrared regions. In order to solve this drawback, considerable efforts have been spent in improving photocatalytic ability of ZnO nanoparticles which is determined by the ability to create electron-hole ($e^-/h^\bullet$) pairs under photo illumination. When a ZnO crystal absorbs a photon which has energy greater than or equal to the band gap energy of ZnO, an electron may be promoted from the valence band to the CB and hole forms in the valence band.

2.3.3 Applications of ZnO in textile industry

The growing of health and hygiene concerns in textile based consumer products brings in an increasing demand in development new materials for textile finishing with UV-blocking, antimicrobial and self-cleaning surface properties. Antimicrobial properties for example can be achieved by applying nano sized silver and self-cleaning and UV blocking properties are imparted by the use of TiO_2 nanostructures [75]. ZnO nanoparticles have superior UV-blocking property in addition its antimicrobial and in some cases self-cleaning properties making a good candidate in technological textile industry comparable to above mentioned novel surface finishes [76]. In particular, nano-sized ZnO is more efficient at absorbing and scattering UV radiation than the conventional size due to increased surface area and intense absorption in the UV region [77].

An important issue on the textile coating is stability of the coating after the laundering of textile. Ates and Unalan reported that ZnO nanowires grown by a microwave–assisted hydrothermal method and functionalized with steric acid to achieve super-hydrophobic property are found to be stable for up to four time washing at 50 °C under continuous stirring for 15 min [78].

2.2.4 Applications of ZnO in rubber industry

A major portion of global production of ZnO is consumed in the rubber industry to fabricate various cross-linked rubber product. ZnO powder is added to increase thermal conductivity of pure silicone rubber while keeping its high electrical resistance and so promising candidates as high performance engineering materials. With the addition of ZnO at nano-scale, high thermal conductivity can be achieved even at relatively low amount of ZnO addition [79]. However, in polymer matrix, aggregation of ZnO nanostructures to form larger size particles is observed due to the weak interaction between the surface of the nanoparticles and polymer. In order to solve this aggregation problem. Yuen et al. reported that surface modified ZnO nanoparticles with the vinyl silane group are added into the silicone rubber through hydrosilylation reaction [80]. These composites exhibited higher thermal conductivity and better mechanical properties because of the formation of a cross-linked structure with the silicone rubber matrix and better dispersion in the matrix.

Przybyszewska and Zaborski investigated the effect of surface area, particle size and morphology of ZnO on the activity of cross linking process [81]. They found that nano-scale particle size results in the better mechanical properties and higher cross link density compared with the micro-size particles. Furthermore, tensile strength is four times greater in nano scale size than that of micro scale size of particles. They also reported that the highest activity of cross linking is obtained when three dimensional snowflake morphological ZnO particles are used.

2.2.5 Pharmaceutical and cosmetic applications of ZnO

Antibacterial, disinfecting and drying properties of ZnO give an opportunity to use in the various kinds of medicines. It has been used as orally administered medicines for epilepsy and diarrhea. By means of accelerating wound healing property, ZnO has been also used as dermatological substances against inflammation. In addition, it has been also used in the dentistry as a dental paste components and temporary filling agents. Another important application field in medicine is as relief agent for diaper rash of babies. This type creams containing up to 40% ZnO.

ZnO is also an important material to preserve from skin cancer which is the most common type of cancer in the United States. Traditional sun-blocks containing various kind of chemicals may cause some skin irritation. New generation sun creams should prevent sun's UV radiation from reaching the skin. They should be absorb both UVB (290-320 nm) and UVA (320-400 nm) light and provide high sun protection factor products. A mixture of ZnO and TiO_2 has been used to provide an effective broad spectrum physical sun-blockers [82]. Particle size of these components are important since large ZnO particles results in a white barrier that is not cosmetically appealing. When ZnO structures with the nano scale particle size are used, suncreams efficiently absorb UV radiation, do not irritate the skin and easily absorbed by the skin

2.4 Synthesis methods of ZnO

Due to the specific needs in diverse applications, there has been a strong interest in development of preparation methods enabling of production of ZnO nanostructures with well-controlled size and shape. In addition, low production cost, high product yield, simple equipment requirements are the other of key factor for the choosing the synthesis technique. Many methods ranging from gas-phase processes to solution routes have been intensively investigated for synthesis ZnO nanostructures. According to temperature, synthesis methods can be classified into two main groups; *i) vapor based synthesis techniques* and *ii) solution based synthesis techniques.*

2.4.1 Vapor based synthesis techniques

These methods are high temperature (~1000 °C) required synthesis methods and can be divided into two main groups:

1. Chemical vapor deposition (CVD),
2. Physical vapor deposition (PVD).

2.4.1.1 Chemical vapor deposition

The chemical vapor deposition (CVD) is a technique based on a chemical reaction between gaseous forms of the precursors at the surface of the substrate material. A schematic representation of the general process steps is shown in Figure 2.11 and include three main stages: i) the generation of the volatile carrier compound, ii) the transportation of the volatile compound by the means of special gases introduced into the system and iii) the chemical reaction on the substrate to form a solid product. The most commonly used form of CVD method is thermal-CVD [83]. Melting point of selected precursor material should be lower than that of the substrate material. This method is usually used in semiconductor industry to produce high-purity and high-performance thin films and 1D structures [84, 85]. In addition, less chemical contamination can be achieved when the noncatalyst growth process is employed [86].

Metal-organic-CVD (MOCVD) [87] and plasma-enhanced CVD (PECVD) [88] are the other generic types of CVD method. MOCVD provides to opportunity for the growth of highly oriented arrays of ZnO nanowires on the substrate surface but it is not cost effective process due to high temperature requirements [89]. PECVD enables the growth of 1D ZnO nanostructures on thermally labile substrates at the relatively lower growth temperatures without any need to the catalyst materials which are used to reduce melting temperature of the precursor material.

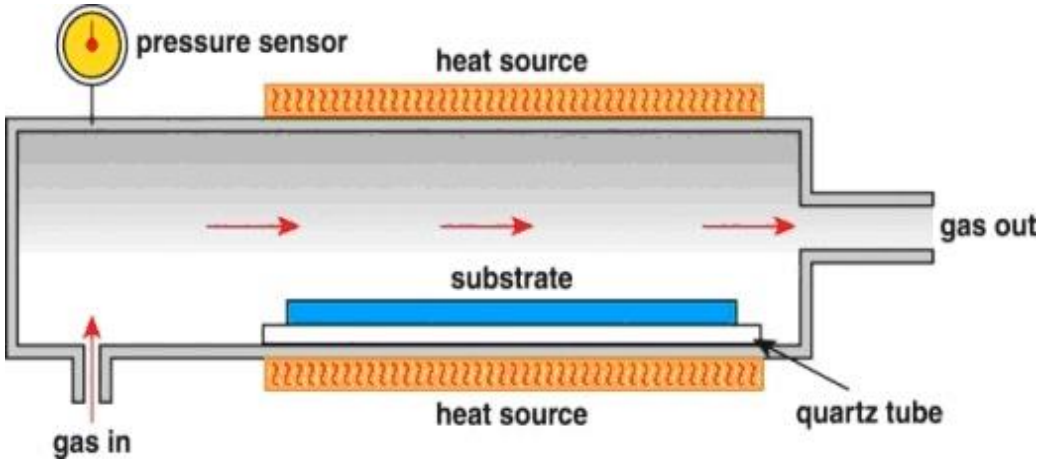

Figure 2.11. A schematic illustration of CVD process [retrieved from: http://www.azonano.com/ Last accessed on 17.11.2014].

2.4.1.2 Physical vapor deposition

The physical vapor deposition (PVD) is a technique based on the firstly vaporization of the precursor material in the form of atoms or molecules from a solid or liquid source and then transportation of these gas through a vacuum or low pressure gaseous environment onto a substrate. Generally, PVD technique is used to deposit film structure with the thickness range from a few to thousands nanometers. The most commonly used PVD techniques are; vacuum deposition and sputter deposition methods.

Vacuum deposition usually takes place in the gas pressure range of 10^{5-} to 10^{9-} Torr and provides to inhibit the possibility of the gaseous contamination. Generally, thermal evaporation of the source material is done using thermal heated source. Sputter deposition technique is based on the vaporization of particles from a target surface by the physical sputtering process. In this process, surface atoms are physically ejected from a solid surface by means of atomic sized energetic particles accelerated from plasma. Sputter deposition can be done by ionic bombardment of solid surface in vacuum using low pressure plasma (<5 m Torr) or high pressure plasma (5-30 m Torr).

2.4.2 Solution based synthesis methods

Each synthesis method can directly affect the final properties of ZnO nanostructures. Dispersion of the different phases (ions and particles) is the basic phenomena of the solution based synthesis methods. These methods usually require low temperature synthesis media (~100 °C). Solution based synthesis methods can be classified as:

1. Hydrothermal method,
2. Spray pyrolysis,
3. Sol-gel method,
4. Microemulsion method,
5. Precipitation method.

2.4.2.1 Hydrothermal method

Hydrothermal synthesis method is based on the chemical reactions of substances above ambient temperature and pressure in a sealed heated solution. This method has advantageous to obtain high-purity, highly crystalline reaction products and also advantageous to control particle size and morphology by adjusting the source species, reaction temperature and time [90]. ZnO nanoforms with various morphologies are produced by hydrothermal method which does not require the use of organic solvents for shape control. The synthesis of ZnO nanostructures are carried out in an autoclave, where the substrate materials are heated gradually to a temperature 100-300 °C [91]. A number of studies have shown that processing parameters including reaction time, temperature, the usage of surfactant and the type of surfactant material can affect the final size and morphology of ZnO nanostructures [92-94]. For example, mono-dispersed ZnO nanorods with the average diameter smaller than 50 nm and the aspect ratio to 30-40 can be synthesized with hydrothermal method by mixing a proper zinc salt and NaOH solution at 180 °C for 20 h in an electric oven [91]. During the synthesis, as a result of heating to reaction temperature then cooling to room temperature, firstly, ZnO crystal nuclei forms and then these nucleus grow, thus the diverse sizes and morphologies of resulted ZnO nanostructures are obtained. A mixture of needle- and

plate-like ZnO particles were synthesized by hydrothermal treatment of a washed precipitate of Zn(OH) formed by mixing $ZnCl_2$ and NaOH [95].

2.4.2.2 Spray pyrolysis

A conventional spray pyrolysis method is based on the atomizing precursor solutions, drying the droplets and reacting the precursor particles at high temperatures in the gas phase [96]. High purity ZnO nanostructures can be synthesized by using spray pyrolysis method [97]. Formation of non-agglomerated particles without milling, control over particle size and particle size distribution, control over crystallinity (grain size), and formation of homogeneous materials are advantages of the preparation of ZnO phosphor samples by using spray pyrolysis.

ZnO nanoparticles were made by flame spray pyrolysis of zinc acrylate– ethanol–acetic acid solution and by changing the solution feed rate, the average primary particle diameter can be controlled from 10 to 20 nm [98]. In addition, the chosen of the precursor materials is important since the chemical nature of the precursor material can directly affect morphology and structure of the reaction products.

2.4.2.3 Sol-gel method

Sol-gel technique is generally defined as the transition of a liquid solution into a solid gel matrix. It is based on the both physical chemical reactions involving hydrolysis condensation drying and densification [99]. Applying sol-gel method to fabricate ZnO nanostructures is the subject of much interest due to its reliability, repeatability, simplicity, and comparatively mild conditions of synthesis. It is usually used for template assisted nanowire fabrication and thin film and enables the surface modification of ZnO with selected organic compounds. Vertically oriented ZnO nanowires have been fabricated using a template by a cathodically induced sol–gel electrodeposition method at room temperature [100]. Fabrication of a large area thin film is easily carried with the sol-gel method which provides to control over the film composition and uniformity of thickness. The annealing temperature is an important

parameter to determine structure of thin films [101]. The crystallite sizes increase with increasing annealing temperature and so thin film crystallinity has been improved with annealing. Figure 2.12 exhibits a general overview for the fabricating films from a colloidal sol and powder from gel.

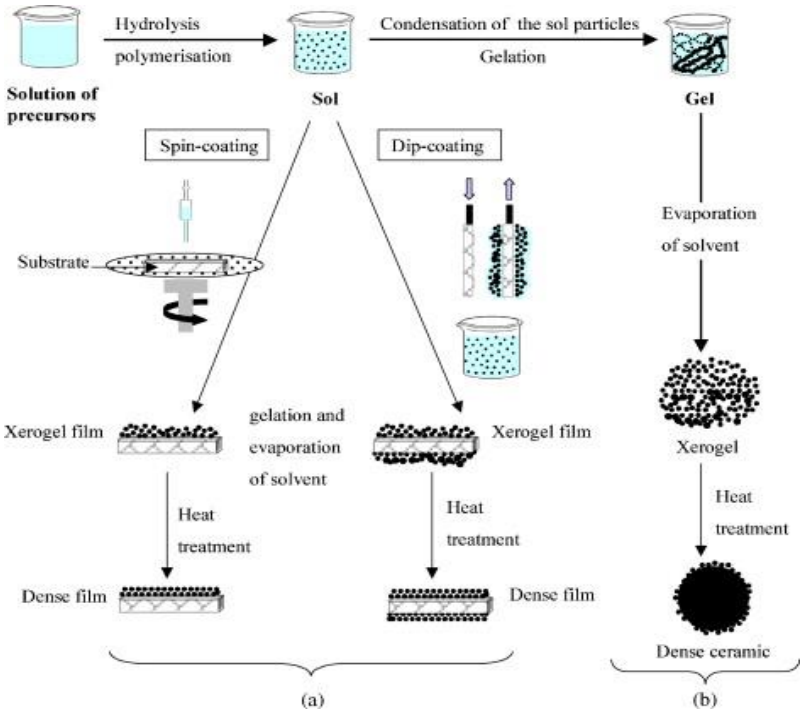

Figure 2.12. Schematic representations of two synthesis examples by the sol–gel method; (a) films from a colloidal sol and (b) powder from a colloidal sol transformed into a gel [102].

Various morphological ZnO nanostructures can be synthesized with sol-gel method. Ba-Abbad et al. investigated both experimental synthesizing of spherical shaped ZnO powders by sol-gel from zinc acetate dehydrate, oxalic acid and ethanol and theoretical investigation of the influence of process parameters involving molar ratio of the starting materials, pH and the calcination temperature on the particle size of ZnO [103]. They theoretically determined the optimum conditions for obtaining a minimum particle size of ZnO (size: 22.9 nm); a molar ratio of 1.76 of precursors, pH of 1.50 and calcination at 402.2 °C. The obtainable particle size upon applying the theoretically determined conditions is 18 ± 2 nm.

2.4.2.4 Microemulsion method

Another versatile technique for synthesis of ZnO nanoparticles is microemulsion method, which does not require any complex preparation procedure, sophisticated equipment and rigorous experimental conditions, but still providing possibilities in controlling the size and morphology of the ZnO powders in a size scale approaching to nanometers. In 1940s, the concept of microemulsion was introduced by Hoor and Schulman [104]. They realized a milky emulsion containing hexanol converted into a clear single phase solution by titrating. The first description of microemulsion was made in 1981 by Danielson and Lindman. They defined microemulsion as "a system of water, oil and amphiphile which is single optically isotropic and thermodynamically stable liquid solution" [105].

According to thermodynamical stability, dispersion of two immiscible liquids can be classified as macro, mini or microemulsion. Droplet size is 2-20 μm for macro-, 0.1-0.3 μm for mini-, < 0.1 μm for micro, ~0.01 μm for miceller- and ~0.001 μm for molecular-emulsion. The key differences between macro and microemulsion are thermodynamic stability, appearance and commercial production types. Opposite to macroemulsions, microemulsions show thermodynamically stability so phase separation does not take place for a long time. In addition, macroemulsions require a mechanical mixing/stirring to achieve temporary stability [106]. Furthermore, microemulsions are clear or translucent appearance, while macroemulsions are cloudy. Generally, microemulsions can be classified into two main groups. First one is *water in oil* (w/o) called as reverse or inverted micelles wherein water droplet are dispersed in continuous oil phase. The other microemulsion type is *oil in water* (o/w) named as normal micelles wherein oil droplets are dispersed in the continuous aqueous phase. the terms of water and oil are very general; the "water" term is usually used for highly polar and hydrophilic liquid while the "oil" term defines hydrophobic and nonpolar liquids [107].

Figure 2.13 shows a schematic representation of normal and reverse micelle structures. In reverse micelle system, there is free water in core called as "nanoreactors" in nanoparticle synthesis. Both microemulsion system is stabilized by addition of surfactants addition (surface active agent). The presence of surfactant molecules in the oil-water system provides to change the nature of interaction between oil and water from repulsive to attractive forces.

Surfactants are comprised of polar hydrophilic head group and non-polar hydrophobic tail group which contains hydrocarbon chain containing about 8-18 carbon atoms. They are classified as anionic, cationic and non-ionic surfactants according to their head group. Surfactants are employed in microemulsion formation by lowering the interfacial tension of oil-water surface by adsorption so they minimize the positive free energy change of dispersion related with surface formation [106]. Aerosol OT (AOT, sodium bis(2-ethylhexyl) sulfosuccinate) which has been used for a long time [108] is an anionic surfactant with two hydrocarbon chains and does not require usage of co-surfactant in order to form microemulsion [109].

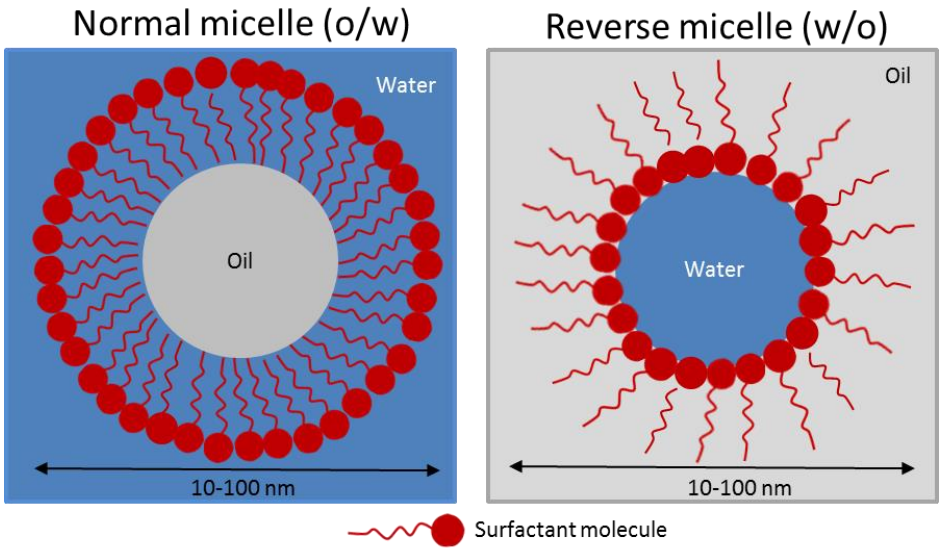

Figure 2.13. Schematic representation of normal and reverse micelle structures.

Generally, microemulsions are prepared by using two different routes. In first one, nanoparticles are synthesized by preparing a single microemulsion. One of the reactants is added inside the reverse micelle and another reactant is added directly to the system. In second route, two separate microemulsion solutions, one containing a salt and the other containing a reducing agent are prepared [110]. After mixing these solutions, nucleation occurs in the micelle edge and then growth takes place around the nuclei in nanoreactor droplet [111]. Droplets are very small in size so; they are subjected to Brownion motion. They continuously collide into aggregates and disintegrate into droplets. Due to these continuous coalescence and decoalescence process, the content of water pool will be distributed over the all microemulsion system. As a result, nanoparticles are synthesized homogeneously in all microemulsion solution.

Spherical ZnO nanoparticles with very small size (<5 nm) and uniform size distribution can be synthesized by forming reverse micelle with several nanometer sized water droplets when NP series (polyoxyethylene nonylphenyl ether) are used as surfactant. These water droplets act as reactor to take place hydrolysis reaction of zinc source and prevent growth of nanoparticles and give spherical shape to ZnO nanoparticles. Therefore, narrow and very small size particles are synthesized. With regard to the synthesis of nanoparticles by the microemulsion techniques, nanoparticles size can be controlled by changing the length of chain of surfactants. When surfactant with longer hydrophilic chain are used, considerably small size reverse micelle so small size ZnO nanoparticles are fabricated such as nanoparticles size 3.9 nm for short hydrophilic chain and 2.4 nm for long hydrophilic chain [112].

ZnO hexagonal nano prisms are synthesized by using PVP as surfactant. PVP layers at the interface between water and oil can act as template for the growth of ZnO because the hydrophilic and negatively charged head of PVP is directly attach to Zn^{2+} cation of zinc source. By reaction at high temperature, ZnO growth from the positively charged Zn^{2+}. PVP molecules are also employed as passivants to quench the visible emission of ZnO so, in the presence of PVP, ZnO hexagonal nanoprisms with high crystal quality exhibit the intensive near-band-edge UV photoluminescence [113].

ZnO nanorods with approximately 16 nm average diameter are fabricated using dodecyl benzene sulfonic acid sodium (DBS) assistant by a simple microemulsion method at a low temperature (61.2 °C). ZnO nanorod samples shows strong ultraviolet emission peak in the time dependent photoluminescence spectra. This indicates that the surface quality of the ZnO nanorods is very high when DBS is used as surfactant [114]. Surfactant addition, DBS, is a key condition to produce 1D nanostructures, nanorods. Without surfactant, larger sized aggregated nanoparticles are obtained. When surfactant concentration increases to a certain level, the micelle size and thus the diameters of the ZnO nanocrystals formed in these rodlike micelles decrease [115]. Reaction time is also a critical issue to synthesize ZnO with different size and morphologies. At the initial stage, the microemulsion droplets determines the nucleation process and the shape of ZnO nanostructures so spherical ZnO nanostructures are fabricated. With the extension of the reaction time, the growth process will dominate to control the shape of ZnO nanostructures so 1D nanoparticles and nanorods are synthesized. The evidenced evolution process from nanoparticles to high aspect ratio and single crystalline 1D nanostructures suggested that the formation process might involve a directed aggregation growth process mediated by microemulsion droplets, in which microemulsion droplets play an important role in modulating crystal size and shape through controlling nucleation rate and nuclei size at the initial stage [116]. After the nucleation process finished at longer heating duration, the directed aggregation growth of microemulsion droplets might occur due to simultaneously collision, conglutination, and amalgamation of different microemulsion droplets. A linear aggregation occurred between the droplets and provided a favorable environment for the recrystallization into a single-crystalline 1D structure along a preferred orientation [117].

Synthesis time, temperature and precursor salt type also affect the morphology of ZnO nanorods. With increasing annealing period (2.5-4h) for a fixed calcination temperature (780°C), the diameter of ZnO nanorods increases. Moreover, at constant annealing time (2.5h), the length and diameter of ZnO nanorods increased with annealing temperature (780-820°C). Therefore, the mean diameter and length of ZnO nanorods increased with increasing annealing temperature and time [118].

Different morphologies of ZnO nanostructures are also synthesized by changing the concentration of microemulsion component. Needle-like, columnar, and spherical morphologies can be obtained when Triton X-100, $Zn(NO_3)_2$ and PEG400 are used as surfactant, zinc source and directing agent, respectively. Passivant, PEG400, addition provides to control the crystal growth by adsorption and encapsulation the nuclei surface and so provides to control final morphology of ZnO nanostructures. In the absence of PEG400, needle-like ZnO with 150–200 nm in length were prepared due to the preferential growth of ZnO crystal growth along the (0001) direction. This shows that restricting effect of the microemulsion, and the surfactant molecules present at the interface controls the excess growth of structures. In the addition of PEG400 with appropriate amounts, during growth process, the directing agent adsorbs on some surfaces of ZnO nuclei, including the face in the (0001) direction.

2.4.2.5 Precipitation method

Since the synthesis route determines the later properties of the material, the preparation method chosen is a very important issue to synthesize ZnO with different size and morphology. High temperature synthesis process of ZnO nanoparticles is unfavorable due to high energy consumption. Template synthesis approaches also lead to some problems such as incorporation of impurities deteriorating the optical/electrical properties of the ZnO particles. On the other hand, aqueous precipitation method can be employed for large scale production of phase pure ZnO nanoparticles at economically/technologically relevant conditions.

Furthermore, synthesizing ZnO with a repeatable process is possible with precipitation method. In this method, fast and spontaneous reduction of a precursor zinc salt occurs by means of using a reducing agent. Precipitation process is generally controlled by the precipitation pH, temperature, time, concentration of reagents, addition and concentration of chelating agent [119-121].

Hong et al. reported that a controlled precipitation method which was carried out using zinc acetate and ammonium carbonate as zinc precursor and reducing agent [122]. To

obtain ZnO nanoparticles with the diameter of 40 nm, a calcination treatment at 450 °C for 3 h was required. However, in this process, agglomeration of particles is a problem. To solve this challenge, calcination can be applied after the heterogeneous azeotropic distillation of the precursor material. Thus, the agglomeration of particles is reduced and particle size decreases to 30 nm.

Lanje et al. used a single step precipitation process with large scale/cost effective preparation of ZnO nanostructures without unwanted impurities [123]. With the usage of low cost precursors such as zinc nitrate as zinc precursor and sodium hydroxide as reducing agent, ZnO nanoparticles were synthesized. To reduce the occurrence of agglomerates among the smaller particles, chelating agent containing many O-H groups which could bind the surface of the nanoparticles at the initial nucleation stage was used.

In presence of water-soluble surfactants/polymers or other similar kind of additives to tune the shape of ZnO nanostructures, aqueous based methods can be performed at relatively low temperature than the high-temperature non-aqueous methods [124]. Due to adsorption of surfactants or additives on specific growing direction, the relative growth rate in different crystallographic planes can change so anisotropic structures can be formed. Therefore, not only nucleation and particle growth, but also coagulation and flocculation of the particles can be affected by the presence of these types of compounds. Single-crystal ZnO nanorods are synthesized at relatively low temperature (100 °C) by using zinc acetate and polyvinyl pyrrolidone (PVP) as precursors [125]. Although synthesis are carried at relatively low temperature, burning of the solid products are carried at 300 °C. To prepare ZnO nanorods, PVP addition plays an important role because as a template, PVP can be removed from the surface of particles by burning the solid products. Moreover, PVP provides to prevent the assembly of ZnO nanoparticles and the growth of ZnO nanorods along [0001] direction by possibly inhibiting the growth of other crystal faces.

A shape controlled precipitation method was also used by Li et al. [126]. Various shapes including forms resembling rice grains, nuts and rods were synthesized from

zinc nitrate hexahydrate and sodium hydroxide in the presence of sodium dodecyl sulfate and triethanolamine as cationic surfactants. It was found that the presence of surfactants affect both the size and morphology of the resultant ZnO particles.

When the water-soluble polymers, poly(vinyl methyl ether) (PVME) is used as shape-directing as well as a stabilizing agent, ZnO nanostructures with various shape can be synthesized at low precipitation temperature. Although in the absence of PVME addition, non-uniform morphological ZnO nanostructures are synthesized, the presence of PVME promotes the formation of dumbbell-shaped nanostructures as a result of the adsorption of PVME on some specific plane of ZnO nanostructures during its growth. pH has also effect on the morphology of ZnO nanostructures. Lance-shaped nanostructures are performed at lower NaOH concentrations, whereas, at higher NaOH concentrations, triangular ZnO nanostructures are synthesized. Consequently, ZnO nanostructures formed in presence of PVME are uniform and regular with three types of morphologies e.g., dumbbell, lance and triangle. But, the ZnO nanostructures prepared in absence of PVME are non-uniform and irregular shape with smaller size. Therefore, polymer addition at different NaOH concentration plays a crucial role in the formation of ZnO nanostructures with different morphologies and sizes [127].

Different adsorption ability of the different additive on various facets of ZnO leads to the different growth rate for different crystal faces. Solvent type has also effect on morphology of ZnO nanostructures. Ethylene glycol (EG) and water can be used in precipitation method during precipitation reaction. When EG is used as solvent, it restricts ZnO structures to grow along [0001] direction and so hinders the formation of 1-D structures. Moreover, the sizes of the obtained ZnO structures decrease. EG molecules can react with Zn^{2+} ions and fasten on surface of ZnO nuclei. EG molecules are firstly linked to the (0001) plane of ZnO, which is Zn rich plane. At higher EG content, the number of connection between EG molecules and (0001) plane of ZnO nuclei will increase. Therefore, surface energy of growth direction will decrease. As a result, growth rate along the [0001] direction will decrease. So in the presence of EG as solvent, spherical ZnO nanostructures are synthesized. Another effect of EG on ZnO

structures is reducing the size of obtained structures due to a higher viscidity compared with water [128].

2.5 Functionalizing of ZnO with doping

Doping is a process in order to improve chemical, physical and optical properties of semiconductors by adding impurity atoms into semiconductor structure. Rare earth elements, noble metals and transition metals are used as doping materials for ZnO.

2.5.1 Rare earth doping

For optoelectronic devices, trivalent rare earth (RE) elements such as RE-GaN, RE-Si have received great research interest due to efficient energy transfer from host semiconductor to RE^{3+} ions. In the rare earth doped ZnO structures, although most of the studies have been focused on the europium (Eu), scandium (Sc) and yttrium (Y) have been also studied to obtain highly transparent and conductive ZnO thin films [129].

2.5.2 Noble metals

Gold (Au), platinium (Pt), iridium (Ir), palladium (Pd), ruthenium (Ru), rhodium (Rh) and silver (Ag) are the examples of the noble metal class of the periodic table. In literature, Ag doped ZnO has been used for the photocatalytic applications, while Ru, Rh and Pt are used to increase the gas sensitivity properties of ZnO gas sensors [130]. Noble metals are resistant to corrosion and oxidation. Noble metals have lower Fermi level than that of ZnO. Thus, noble metal doping is used for the photocatalytic applications. Lover Fermi level provides to excite photo-generated electrons from CB of ZnO and remain a hole in the VB of ZnO. This electron transfer leads to higher photocatalytic activity according to pure condition by decreasing the possibility of the electron-hole recombination. The photocatalytic ability of the noble metal doped ZnO depends on the dopant amount since there is a critical dopant concentration to form electron-hole recombination centers.

If $e^-/h^\bullet$ charge separation is maintained, they can migrate to the catalyst surface where they participate in redox reactions with adsorbed species. These $e^-/h^\bullet$ pairs can be used for the oxidation of a wide range of organic molecules/contaminants [131]. During the reactions, organic molecules are oxidized with hole and adsorbed oxygen molecule is taken up by the electron. Therefore, highly active superoxide radical ($O_2^{-\bullet}$) forms and these superoxide radical transforms into reactive species like $HO^\bullet$, $HO_2^\bullet$, and H_2O_2, which act as oxidizing agents in the presence of moisture. Creation of self-cleaning surfaces, oxidation of organic contaminants and conversion of carbon dioxide into gaseous hydrocarbons are typical photocatalytic reactions.

The rapid recombination of the photogenerated $e^-/h^\bullet$ pairs is the major limiting factor which hinders enhancement of photocatalytic activity of ZnO nanoparticles. To overcome this problem, semiconductor combination [132], transition metal doping [133] and noble metal deposition [134] have been applied. Among these techniques, noble metal deposition seems to be most promising. Loading with various noble metals such as Au, Pd and Ag could significantly improve photocatalytic activity of ZnO nanoparticles. Wu and Tseng reported significant enhancement of the photocatalytic activity of ZnO nanorods upon loading Au nanoparticles with sizes smaller than 15 nm [135]. By depositing an appropriate amount of Pd on the surface of the ZnO, the photocatalytic activity of ZnO nanoparticles could be greatly enhanced [136]. Doping ZnO nanoparticles with silver (Ag) has been also employed to enhance photocatalytic ability of ZnO nanoparticles [134]. Gouvea et al. prepared Ag doped ZnO photocatalyst exhibits better photocatalytic property than pure ZnO [137].

The exact role of Ag in increasing the visible light response of ZnO nanoparticles is intensively investigated for developing electronic and optoelectronic devices. In the photochemical reactions, Ag can trap the photogenerated electrons from the ZnO and form the holes to create hydroxyl radicals which provide the degradation reaction of organic species present. In addition, Ag can improve the photocatalytic activity of ZnO nanoparticles by creating a local electric field and enhance electrical properties by the optical vibration of surface plasmon [138]. Wang et. al. reported that surface properties

like oxygen vacancies and crystal defects also effect photocatalytic activity of Ag doped ZnO nanostructures [19].

2.5.3 Transition metals

There is currently intense interest in the origin of room temperature ferromagnetism (RTFM) in metal oxide nanoparticles. ZnO is one of the well-known semiconductor metal oxides, which has a wide direct band gap and large exciton binding energy at room temperature. Reduction in size to the nano scale, introduces novel electrical, mechanical, chemical and optical properties to ZnO nanomaterials due to surface and quantum confinement effects. For example, these unique properties give ZnO several advantages in spintronic devices due to room temperature ferromagnetism behavior when they are doped with small amounts of transition metals (TM). The definition of transition metals is made by IUPAC as "an element whose atom has a partially filled d sub-shell, or which can give rise to cations with an incomplete d sub-shell" made by the IUPAC [139].

The electronic band structure of the substituted TM ions with 3d electron states is generally exposed to two competing factors: i) strong 3d-host hybridization and ii) strong 3d-3d Coulomb interactions. Hybridization between 3d of TM and the host VB state causes to the magnetic interaction. At high Curie temperature (>100 K), the observation of the ferromagnetic property in III-V and II-VI type semiconductors has attracted great interest due to their long spin-coherence time and rapid development of the information storage technologies.

The role of the TM incorporation in ZnO based DMSs is of considerable significance because the origin of the RTFM was claimed to be based on two controversies; ferromagnetism (i) is an external property and comes from impurities like TM clusters [140, 141] or (ii) is an intrinsic property and originates from the spin-polarized carries [142, 143]. Therefore, many studies have been performed to elucidate the underlying mechanism for RTFM. Up to now, various TMs such as manganese [144], cobalt [145], and iron [146] have been incorporated into ZnO structure to achieve RTFM

property. The major drawback of these TM is that the dopant atoms can form clusters or precipitates directly affecting the ferromagnetic properties and such impurities impede the use of DMSs for spintronics applications [47]. Recently, researchers have focused on copper incorporated ZnO (ZnO:Cu) nanostructures [147-149] instead of traditional DMSs incorporated with other TMs since metallic copper is not magnetic, and neither Cu_2O nor CuO is ferromagnetic. However, the origin of the RTFM behavior of the ZnO:Cu is not well understood due to confliction between experimental and theoretical studies. Thus, it is important to clarify the nature of the RTFM with detailed experimental study.

2.6 References

1. Bevan D.J.M. and Anderson J.S., Discussions of the Faraday Society, **1950**(8) p. 238-246.

2. Cooley A.J., **1866**, London: R. Hardwicke. p. 812.

3. Harrison S.E., Physical Review, **1954** 93(1) p. 52-62.

4. Dudkowsk S., Kepka A.G., and Grosswei L., Journal of Physics and Chemistry of Solids, **1967** 28(3) p. 485-493.

5. Henglein A., Berichte Der Bunsen-Gesellschaft-Physical Chemistry Chemical Physics, **1997** 101(11) p. 1562-1572.

6. Dong L.F., Cui Z.L., and Zhang Z.K., Nanostructured Materials, **1997** 8(7) p. 815-823.

7. Huang M.H., Mao S., Feick H., Yan H., Wu Y., Kind H., Weber E., Russo R., and Yang P., Science, **2001** 292(5523) p. 1897-1899.

8. Pearton S.J., Abernathy C.R., Overberg M.E., Thaler G.T., Norton D.P., Theodoropoulou N., Hebard A.F., Park Y.D., Ren F., Kim J., and Boatner L.A., Journal of Applied Physics, **2003** 93(1) p. 1-13.

9. Tomioka K., Motohisa J., Hara S., Hiruma K., and Fukui T., Nano Letters, **2010** 10(5) p. 1639-1644.

10. Zolper J.C., Solid-State Electronics, **1998** 42(12) p. 2153-2156.

11. Ozgur U., Alivov Y.I., Liu C., Teke A., Reshchikov M.A., Dogan S., Avrutin V., Cho S.J., and Morkoc H., Journal of Applied Physics, **2005** 98(4).

12. Klingshirn C., ChemPhysChem, **2007** 8(6) p. 782-803.

13. ZheChuan F., Brief Historical Review of Research and Basic/Interdisciplinary Characterization of ZnO, **2012**, Taylor & Francis. p. 3-36.

14. Phillips J.C., Reviews of Modern Physics, **1970** 42(3) p. 317-356.

15. Akira O. and Masaki T., Electronic Ferroelectricity in II-VI Semiconductor ZnO. **2012**.

16. Markoc H., Ozgur, U., ZnO: Fundamentals, Materials and Device Technology, **2009**, Weinheim, Germany: Wiley-VCH. p. 488.

17. Kisi E.H. and Elcombe M.M., Acta Crystallographica Section C, **1989** 45(12) p. 1867-1870.

18. Wander A., Schedin F., Steadman P., Norris A., McGrath R., Turner T.S., Thornton G., and Harrison N.M., Physical Review Letters, **2001** 86(17) p. 3811-3814.

19. Wang Z.L., Kong X.Y., and Zuo J.M., Physical Review Letters, **2003** 91(18) p. 185502.

20. Wang Z.L. and Song J., Science, **2006** 312(5771) p. 242-246.

21. Özgür Ü., Alivov Y.I., Liu C., Teke A., Reshchikov M.A., Doğan S., Avrutin V., Cho S.-J., and Morkoç H., Journal of Applied Physics, **2005** 98(4) p. 041301-103.

22. Muller S., von Wenckstern H., Breitenstein O., Lenzner J., and Grundmann M., Electron Devices, IEEE Transactions on, **2012** 59(3) p. 536-541.

23. Girard R.T., Tjernberg O., Chiaia G., Söderholm S., Karlsson U.O., Wigren C., Nylén H., and Lindau I., Surface Science, **1997** 373(2–3) p. 409-417.

24. Dong C.L., Persson C., Vayssieres L., Augustsson A., Schmitt T., Mattesini M., Ahuja R., Chang C.L., and Guo J.H., Physical Review B, **2004** 70(19) p. 195325.

25. King P.D.C., Veal T.D., Schleife A., Zúñiga-Pérez J., Martel B., Jefferson P.H., Fuchs F., Muñoz-Sanjosé V., Bechstedt F., and McConville C.F., Physical Review B, **2009** 79(20) p. 205205.

26. Vogel D., Kruger P., and Pollmann J., Physical Review B, **1995** 52(20) p. R14316-R14319.

27. Srikant V. and Clarke D.R., Journal of Applied Physics, **1998** 83(10) p. 5447-5451.

28. Erhart P., Albe K., and Klein A., Physical Review B, **2006** 73(20) p. 205203.

29. Teke A., Özgür Ü., Doğan S., Gu X., Morkoç H., Nemeth B., Nause J., and Everitt H.O., Physical Review B, **2004** 70(19) p. 195207.

30. Li Y.-Q., Fu S.-Y., and Mai Y.-W., Polymer, **2006** 47(6) p. 2127-2132.

31. Lin B., Fu Z., and Jia Y., Applied Physics Letters, **2001** 79(7) p. 943-945.

32. Vanheusden K., Seager C.H., Warren W.L., Tallant D.R., and Voigt J.A., Applied Physics Letters, **1996** 68(3) p. 403-405.

33. Xu C.X., Sun X.W., Zhang X.H., Ke L., and Chua S.J., Nanotechnology, **2004** 15(7) p. 856-861.

34. Wahab R., Ansari S.G., Kim Y.S., Seo H.K., Kim G.S., Khang G., and Shin H.-S., Materials Research Bulletin, **2007** 42(9) p. 1640-1648.

35. Singla M.L., Shafeeq M M., and Kumar M., Journal of Luminescence, **2009** 129(5) p. 434-438.

36. Aravind A., Jayaraj M.K., Kumar M., and Chandra R., Journal of Materials Science-Materials in Electronics, **2013** 24(1) p. 106-112.

37. King D.M., Johnson S.I., Li J., Du X., Liang X., and Weimer A.W., Nanotechnology, **2009** 20(19) p. 195401.

38. Willander M., Nur O., Sadaf J.R., Qadir M.I., Zaman S., Zainelabdin A., Bano N., and Hussain I., Materials, **2010** 3(4) p. 2643-2667.

39. Kang H.S., Kang J.S., Kim J.W., and Lee S.Y., Journal of Applied Physics, **2004** 95(3) p. 1246-1250.

40. Liu M., Kitai A.H., and Mascher P., Journal of Luminescence, **1992** 54(1) p. 35-42.

41. Wei S.F., Lian J.S., and Jiang Q., Applied Surface Science, **2009** 255(15) p. 6978-6984.

42. Sui X., Liu Y., Shao C., Liu Y., and Xu C., Chemical Physics Letters, **2006** 424(4-6) p. 340-344.

43. Koshihara S., Oiwa A., Hirasawa M., Katsumoto S., Iye Y., Urano C., Takagi H., and Munekata H., Physical Review Letters, **1997** 78(24) p. 4617-4620.

44. Ohno H., Science, **1998** 281(5379) p. 951-956.

45. Dietl T., Ohno H., Matsukura F., Cibert J., and Ferrand D., Science, **2000** 287(5455) p. 1019-1022.

46. Buchholz D.B., Chang R.P.H., Song J.H., and Ketterson J.B., Applied Physics Letters, **2005** 87(8) p. 082504-3.

47. Pearton S.J., Heo W.H., Ivill M., Norton D.P., and Steiner T., Semiconductor Science and Technology, **2004** 19(10) p. R59-R74.

48. Shuai M., Liao L., Lu H.B., Zhang L., Li J.C., and Fu D.J., Journal of Physics D: Applied Physics, **2008** 41(13) p. 135010.

49. Sharma P., Gupta A., Rao K.V., Owens F.J., Sharma R., Ahuja R., Guillen J.M.O., Johansson B., and Gehring G.A., Nature Materials, **2003** 2(10) p. 673-677.

50. Kolodziejczak-Radzimska A. and Jesionowski T., Materials, **2014** 7(4) p. 2833-2881.

51. Brattain W.H. and Bardeen J., Bell System Technical Journal, **1953** 32(1) p. 1-41.

52. Bie L.-J., Yan X.-N., Yin J., Duan Y.-Q., and Yuan Z.-H., Sensors and Actuators B: Chemical, **2007** 126(2) p. 604-608.

53. Renganathan B., Sastikumar D., Gobi G., Rajeswari Yogamalar N., and Chandra Bose A., Optics & Laser Technology, **2011** 43(8) p. 1398-1404.

54. Chen M., Wang Z., Han D., Gu F., and Guo G., The Journal of Physical Chemistry C, **2011** 115(26) p. 12763-12773.

55. Jia Q., Ji H., Zhang Y., Chen Y., Sun X., and Jin Z., Journal of Hazardous Materials, **2014** 276(0) p. 262-270.

56. Chang J.F., Kuo H.H., Leu I.C., and Hon M.H., Sensors and Actuators B: Chemical, **2002** 84(2–3) p. 258-264.

57. Kumar N., Srivastava A.K., Nath R., Gupta B.K., and Varma G.D., Dalton Transactions, **2014** 43(15) p. 5713-5720.

58. Jing Z.H. and Zhan J.H., Advanced Materials, **2008** 20(23) p. 4547-4551.

59. Roy S. and Basu S., Bulletin of Materials Science, **2002** 25(6) p. 513-515.

60. Hagfeldt A., Boschloo G., Sun L., Kloo L., and Pettersson H., Chemical Reviews, **2010** 110(11) p. 6595-6663.

61. Lai M.-H., Tubtimtae A., Lee M.-W., and Wang G.-J., International Journal of Photoenergy, **2010** 2010.

62. Keis K., Magnusson E., Lindström H., Lindquist S.-E., and Hagfeldt A., Solar Energy Materials and Solar Cells, **2002** 73(1) p. 51-58.

63. Ko S.H., Lee D., Kang H.W., Nam K.H., Yeo J.Y., Hong S.J., Grigoropoulos C.P., and Sung H.J., Nano Letters, **2011** 11(2) p. 666-671.

64. Drapak I.T., Soviet Physics Journal, **1969** 12(7) p. 933-934.

65. Bagnall D.M., Chen Y.F., Zhu Z., Yao T., Koyama S., Shen M.Y., and Goto T., Applied Physics Letters, **1997** 70(17) p. 2230-2232.

66. Yungryel R., Tae-Seok L., Lubguban J.A., White H.W., Bong-Jin K., Yoon-Soo P., and Chang-Joo Y., Applied Physics Letters, **2006** 88(24) p. 241108.

67. Dae-Kue H., Kang S.-H., Jae-Hong L., Yang E.-J., Oh J.-Y., Yang J.-H., and Park S.-J., Applied Physics Letters, **2005** 86(22) p. 222101-222101-3.

68. Singhai M., Chhabra V., Kang P., and Shah D.O., Materials Research Bulletin, **1997** 32(2) p. 239-247.

69. Haile S.M., Johnson D.W., Wiseman G.H., and Bowen H.K., Journal of the American Ceramic Society, **1989** 72(10) p. 2004-2008.

70. Hembram K., Sivaprahasam D., and Rao T.N., Journal of the European Ceramic Society, **2011** 31(10) p. 1905-1913.

71. Jansen R., Nat Mater, **2013** 12(9) p. 779-780.

72. Neppolian B., Choi H.C., Sakthivel S., Arabindoo B., and Murugesan V., Journal of Hazardous Materials, **2002** 89(2-3) p. 303-317.

73. O'Neil M., Marohn J., and McLendon G., The Journal of Physical Chemistry, **1990** 94(10) p. 4356-4363.

74. Serpone N. and Pelizzetti, Photocatalysis: fundamentals and applications, E. Wiley. **1989**. p. 650.

75. Yuranova T., Mosteo R., Bandara J., Laub D., and Kiwi J., Journal of Molecular Catalysis A: Chemical, **2006** 244(1–2) p. 160-167.

76. Nadanathangam V., Sampath K., Kathe A.A., Varadarajan P.V., and Virendra P., Nanotechnology, **2006** 17(20) p. 5087.

77. Yadav A., Prasad V., Kathe A.A., Raj S., Yadav D., Sundaramoorthy C., and Vigneshwaran N., Bulletin of Materials Science, **2006** 29(6) p. 641-645.

78. Ates E.S. and Unalan H.E., Thin Solid Films, **2012** 520(14) p. 4658-4661.

79. Mu Q., Feng S., and Diao G., Polymer Composites, **2007** 28(2) p. 125-130.

80. Yuan Z., Zhou W., Hu T., Chen Y., Li F., Xu Z., and Wang X., Surface Review and Letters, **2011** 18(01-02) p. 33-38.

81. Przybyszewska M., The effect of zinc oxide nanoparticle morphology on activity in crosslinking of carboxylated nitrile elastomer, **2009** 3(9) p. 542-552.

82. Breunig H., Weinigel M., and König K., BioNanoScience, **2014** p. 1-6.

83. Cheng A.-J., Tzeng Y., Zhou Y., Park M., Wu T.-h., Shannon C., Wang D., and Lee W., Applied Physics Letters, **2008** 92(9) p. 092113-3.

84. Xiang B., Wang P., Zhang X., Dayeh S.A., Aplin D.P.R., Soci C., Yu D., and Wang D., Nano Letters, **2006** 7(2) p. 323-328.

85. Purica M., Budianu E., Rusu E., Danila M., and Gavrila R., Thin Solid Films, **2002** 403–404(0) p. 485-488.

86. An-Jen C., Yonhua T., Yi Z., Minseo P., Tsung-Hsueh W., Shannon C., Wang D., and Wonwoo L., Applied Physics Letters, **2008** 92(9) p. 092113.

87. Lee W., Jeong M.-C., and Myoung J.-M., Acta Materialia, **2004** 52(13) p. 3949-3957.

88. Liu X., Wu X., Cao H., and Chang R.P.H., Journal of Applied Physics, **2004** 95(6) p. 3141-3147.

89. Jeong M.-C., Oh B.-Y., Lee W., and Myoung J.-M., Journal of Crystal Growth, **2004** 268(1–2) p. 149-154.

90. A. C. Larson and Dreele R.B.V., LANSCE, MS-H805, **1994** Los Alamos National Laboratory p. NM 87545.

91. Liu B. and Zeng H.C., Journal of the American Chemical Society, **2003** 125(15) p. 4430-4431.

92. Ismail A.A., El-Midany A., Abdel-Aal E.A., and El-Shall H., Materials Letters, **2005** 59(14–15) p. 1924-1928.

93. Chen D., Jiao X., and Cheng G., Solid State Communications, **1999** 113(6) p. 363-366.

94. Dem'yanets L.N., Li L.E., and Uvarova T.G., Journal of Materials Science, **2006** 41(5) p. 1439-1444.

95. Van den Rul H., Mondelaers D., Van Bael M., and Mullens J., Journal of Sol-Gel Science and Technology, **2006** 39(1) p. 41-47.

96. Mädler L., Kammler H.K., Mueller R., and Pratsinis S.E., Journal of Aerosol Science, **2002** 33(2) p. 369-389.

97. Vanheusden K., Seager C.H., Warren W.L., Tallant D.R., Caruso J., Hampden-Smith M.J., and Kodas T.T., Journal of Luminescence, **1997** 75(1) p. 11-16.

98. Tani T., Madler L., and Pratsinis S.E., Journal of Nanoparticle Research, **2002** 4(4) p. 337-343.

99. Ohyama M., Kouzuka H., and Yoko T., Thin Solid Films, **1997** 306(1) p. 78-85.

100. Öztürk S., Taşaltın N., Kılınç N., Yüzer H., and Öztürk Z., Applied Physics A, **2010** 99(1) p. 73-78.

101. Ivanova T., Harizanova A., Koutzarova T., and Vertruyen B., Materials Letters, **2010** 64(10) p. 1147-1149.

102. Znaidi L., Materials Science and Engineering: B, **2010** 174(1–3) p. 18-30.

103. Ba-Abbad M.M., Kadhum A.A.H., Mohamad A.B., Takriff M.S., and Sopian K., Journal of Industrial and Engineering Chemistry, **2013** 19(1) p. 99-105.

104. Hoar T. P. S., J. H., Nature **1943** 152(3847) p. 102-103.

105. Danielsson I. and Lindman B., Colloids and Surfaces, **1981** 3(4) p. 391-392.

106. Lawrence M.J. and Rees G.D., Advanced Drug Delivery Reviews, **2000** 45(1) p. 89-121.

107. Li X., He G., Xiao G., Liu H., and Wang M., Journal of Colloid and Interface Science, **2009** 333(2) p. 465-473.

108. Angel L.R., Evans D.F., and Ninham B.W., The Journal of Physical Chemistry, **1983** 87(4) p. 538-540.

109. Kumar P., and Mittal K.L., Handbook of microemulsion science and technology, **1999**, New York: Mercel Dekker.

110. Boutonnet M., Kizling J., Touroude R., Maire G., and Stenius P., Catalysis Letters, **1991** 9(5-6) p. 347-354.

111. Li L., Qing-Sheng W., Ya-Ping D., and Pei-Ming W., Materials Letters, **2005** 59(13) p. 1623-1626.

112. Inoguchi M., Suzuki K., Kageyama K., Takagi H., and Sakabe Y., Journal of the American Ceramic Society, **2008** 91(12) p. 3850-3855.

113. Sui X., Liu Y., Shao C., Liu Y., and Xu C., Chemical Physics Letters, **2006** 424(4–6) p. 340-344.

114. Lv Y.Z., Zhang Y.H., Li C.P., Ren L.R., Guo L., Xu H.B., Ding L., Yang C.L., Ge W.K., and Yang S.H., Journal of Luminescence, **2007** 122–123(0) p. 816-818.

115. Lv Y., Guo L., Xu H., Ding L., Yang C., Wang J., Ge W., Yang S., and Wu Z., Journal of Applied Physics, **2006** 99(11) p. 114302-1-4.

116. Zhang J., Sun L.-D., Jiang X.-C., Liao C.-S., and Yan C.-H., Crystal Growth & Design, **2003** 4(2) p. 309-313.

117. Pacholski C., Kornowski A., and Weller H., Angewandte Chemie International Edition, **2002** 41(7) p. 1188-1191.

118. Liu Y., Liu Z., and Wang G., Journal of Crystal Growth, **2003** 252(1–3) p. 213-218.

119. Yildirim O.A. and Durucan C., Journal of Materials Research, **2012** 27(11) p. 1452-1461.

120. Rodríguez-Paéz J.E., Caballero A.C., Villegas M., Moure C., Durán P., and Fernández J.F., Journal of the European Ceramic Society, **2001** 21(7) p. 925-930.

121. Chen C., Liu P., and Lu C., Chemical Engineering Journal, **2008** 144(3) p. 509-513.

122. Hong R., Pan T., Qian J., and Li H., Chemical Engineering Journal, **2006** 119(2–3) p. 71-81.

123. Lanje A.S., Sharma S.J., Ningthoujam R.S., Ahn J.S., and Pode R.B., Advanced Powder Technology, **2013** 24(1) p. 331-335.

124. Zhang H., Yang D., Ji Y., Ma X., Xu J., and Que D., The Journal of Physical Chemistry B, **2004** 108(13) p. 3955-3958.

125. Tao D., Qian W., Huang Y., and Wei F., Journal of Crystal Growth, **2004** 271(3–4) p. 353-357.

126. Li P., Wei Y., Liu H., and Wang X.-k., Journal of Solid State Chemistry, **2005** 178(3) p. 855-860.

127. Harunar Rashid M., Raula M., Bhattacharjee R.R., and Mandal T.K., Journal of Colloid and Interface Science, **2009** 339(1) p. 249-258.

128. Zhang L. and Zhu Y.-J., Applied Physics A, **2009** 97(4) p. 847-852.

129. Minami T., Yamamoto T., and Miyata T., Thin Solid Films, **2000** 366(1-2) p. 63-68.

130. Xu J., Shun Y.a., Pan Q., and Qin J., Sensors and Actuators B: Chemical, **2000** 66(1–3) p. 161-163.

131. Georgekutty R., Seery M.K., and Pillai S.C., The Journal of Physical Chemistry C, **2008** 112(35) p. 13563-13570.

132. Tada H., Hattori A., Tokihisa Y., Imai K., Tohge N., and Ito S., The Journal of Physical Chemistry B, **2000** 104(19) p. 4585-4587.

133. Ekambaram S., Iikubo Y., and Kudo A., Journal of Alloys and Compounds, **2007** 433(1-2) p. 237-240.

134. Wang R., Xin J.H., Yang Y., Liu H., Xu L., and Hu J., Applied Surface Science, **2004** 227(1-4) p. 312-317.

135. Wu J.-J. and Tseng C.-H., Applied Catalysis B: Environmental, **2006** 66(1-2) p. 51-57.

136. Liqiang J., Baiqi W., Baifu X., Shudan L., Keying S., Weimin C., and Honggang F., Journal of Solid State Chemistry, **2004** 177(11) p. 4221-4227.

137. Gouvea C.A.K., Wypych F., Moraes S.G., DurÃ¡n N., Nagata N., and Peralta-Zamora P., Chemosphere, **2000** 40(4) p. 433-440.

138. Seery M.K., George R., Floris P., and Pillai S.C., Journal of Photochemistry and Photobiology A: Chemistry, **2007** 189(2-3) p. 258-263.

139. McNaught A.D. and Wilkinson A., IUPAC Compendium of Chemical Terminology, **1997**: WileyBlackwell.

140. Shim J.H., Hwang T., Lee S., Park J.H., Han S.-J., and Jeong Y.H., Applied Physics Letters, **2005** 86(8) p. 082503-082503-3.

141. Kane M.H., Shalini K., Summers C.J., Varatharajan R., Vestal C.R., Zhang Z.J., and Ferguson I.T., Journal of Applied Physics, **2005** 97(2) p. 023906-6.

142. Ye L.-H., Freeman A.J., and Delley B., Physical Review B, **2006** 73(3) p. 033203.

143. Ueda K., Tabata H., and Kawai T., Applied Physics Letters, **2001** 79(7) p. 988-990.

144. Muthukumaran S. and Gopalakrishnan R., Journal of Materials Science: Materials in Electronics, **2012** 23(7) p. 1393-1401.

145. Bylsma R.B., Becker W.M., Kossut J., Debska U., and Yoder-Short D., Physical Review B, **1986** 33(12) p. 8207-8215.

146. Yu X., Meng D., Liu C., Xu K., Chen J., Lu C., and Wang Y., Journal of Materials Science: Materials in Electronics, **2014** 25(9) p. 3920-3923.

147. Hou D.L., Ye X.J., Meng H.J., Zhou H.J., Li X.L., Zhen C.M., and Tang G.D., Appl. Phys. Lett., **2007** 90 p. 142502.

148. Owens F.J., Gladczuk L., Szymczak R., and Niedermayer C., Journal of Physics and Chemistry of Solids, **2011** 72(6) p. 648-652.

149. Owens F.J., Journal of Magnetism and Magnetic Materials, **2009** 321(22) p. 3734-3737.

CHAPTER 3

SYNTHESIS OF ZnO NANOSTRUCTURES BY MICROEMULSION METHOD

3.1 Introduction

A microemulsion is a thermodynamically stable dispersion of two immiscible liquids which are usually referred as oil (o) and water (w) [1]. Stability of dispersion is provided by addition of surfactant molecules. Microemulsion method does not require any complex preparation procedure, sophisticated equipment and rigorous experimental conditions, but still providing possibilities in controlling the size and morphology for synthesis of particles in a size scale approaching to nanometers [2]. Even though the product yield is low, narrow size distribution for the resultant nanostructures due to formation of well-dispersed, cage-like small reactors (5–100 nm) in uniform nucleation conditions, is the advantageous aspects of microemulsion routes. ZnO nanoparticles with narrow and uniform size characteristics obtained by microemulsion may offer tunable electrical and optical properties. Such ZnO nanoparticles can be used in some technological applications such as UV-emission optoelectronic and lasing devices, as well as transparent conducting thin films.

There are number of studies reporting preparation of spherical [3-6], rod shaped [7-10] or columnar [2] ZnO nanoparticles by reverse micellar systems or microemulsion-mediated systems. In most of these microemulsion-assisted routes, preparation of nanoparticles is achieved by direct recovery of the ZnO precipitates. Unfortunately, recovery of nanostructured microemulsion products by sedimentation results in aggregation of the ZnO precipitates either during aging and/or subsequent calcination. It is therefore important to develop new methods for the preparation of homogeneous and mono-dispersed ZnO nanoparticles by microemulsion routes. In this study, a

modified microemulsion approach for synthesis of mono-dispersed ZnO nanoparticles has been offered. In this method, different than before mentioned reports, final ZnO nanoparticles are not directly produced in the microemulsion, but formed by thermal decomposition of a zinc-complex microemulsion product by a subsequent calcination process. In the modified microemulsion process, glycerol was used as an internal phase of the reverse microemulsion (Aerosol OT:glycerol:heptane) in a procedure similar to that employed in preparation of ZnO nanoparticles in amorphous silica [5]. The specific objectives of this phase of the study is to determine the effects of surfactant amount, water amount and calcination temperature on the size and morphology of the resultant ZnO nanoparticles.

3.2 Experimental methods

3.2.1 Materials

The chemicals used during synthesis of pure ZnO nanoparticles by microemulsion method are listed in Table 3.1. All reagents were used without further purification.

Table 3.1. Materials used in the experimental part of the synthesis of pure ZnO nanoparticles with microemulsion method, their formulas and sources.

Material	Chemical Formula	Grade	Source
Zinc acetate dihydrate	$C_4H_6O_4Zn{\cdot}2H_2O$	99.5%, powder	Riedel
Sodium bis(2-ethylhexyl) sulfosuccinate, AOT	$C_{20}H_{37}NaO_7S$	96%, bulk	Fluka
Glycerol	$C_3H_8O_3$	87%, solution	Merck
n-heptane	C_7H_{16}	extra pure, solution	Riedel
Methanol	CH_3OH	99.9%, solution	Riedel
Chloroform	$CHCl_3$	99.8%, solution	Sigma Aldrich

3.2.2 Experimental procedures

The synthesis of ZnO nanoparticles was carried out using reverse microemulsion system using sodium bis(2-ethylhexyl) sulfosuccinate (Aerosol OT or AOT) as the surfactant, glycerol as the polar phase (water, w) and n-heptane as the non-polar phase (oil, o). Zinc precursor was zinc acetate dihydrate. The effects of surfactant amount, water amount and calcination temperature on the size and morphology of ZnO nanoparticles were investigated by using different microemulsion formulations. Selected microemulsion formulations are given by the circular points (named as S1.i or S2.i; i= 1-5) in Figure 3.1 and listed in Table 3.2 as in weight percentages**.**

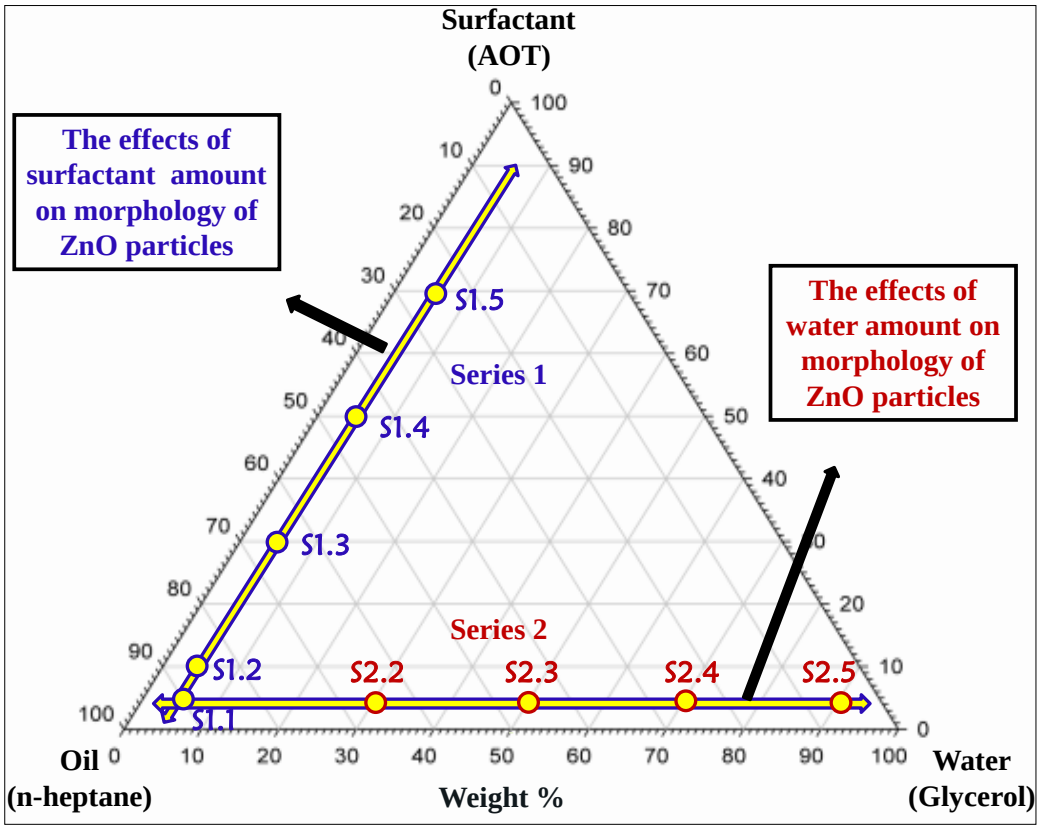

Figure 3.1. A schematic representation of the specific surfactant-oil-water ternary phase diagram with selected microemulsion formulations.

Table 3.2. Selected microemulsion formulations (weight %).

Name	AOT	Glycerol	n-heptane	Name	AOT	Glycerol	n-heptane
S1.1	5	5	90	S1.1	5	5	90
S1.2	10	5	85	S2.2	5	30	65
S1.3	30	5	65	S2.3	5	50	45
S1.4	50	5	45	S2.4	5	70	25
S1.5	70	5	25	S2.5	5	90	5

To prepare ZnO nanoparticles by the microemulsion system S1.1 (AOT:glycerol:n-heptane, 5:5:90), first required amount of AOT was dissolved in n-heptane at room temperature by stirring. After achieving complete dissolution, this solution was divided into glass containers and two separate AOT:n-heptane solutions, solution-A and solution-B, were obtained. Then, half of the glycerol containing 0.5 M zinc acetate dehydrate was slowly added into solution-A under constant stirring. Similarly, rest of the glycerol containing 0.5 M NaOH solution was added into solution-B. NaOH was introduced as a catalyst. Both solutions were stirred at room temperature until they become completely transparent. Then, solution-B was slowly added into solution-A under constant stirring and resulting mixture was further homogenized by refluxing at 60-70 °C for 24 h. At the end, the white solid powders were collected via centrifugation for 20 min at 10000 rpm. The solid extracts were then washed three times with a mixture of 1:1 (vol %) methanol and chloroform solution by centrifugation at 10000 rpm for 10 min. The obtained powders were dried at 100 °C for 1 h in an open atmosphere drying oven and in a vacuum dryer at room temperature for overnight. Finally, they were calcined in air atmosphere for 3 h at 300 °C, or 400 °C, or 500 °C. In addition, to investigate the effects of *surfactant* and *water amount* on the size and morphology of final ZnO nanostructures, this experimental procedure was repeated by changing the relative ratio of AOT (series 1) and glycerol amount (series 2). A schematic representation of the experimental procedure is shown in Figure 3.2.

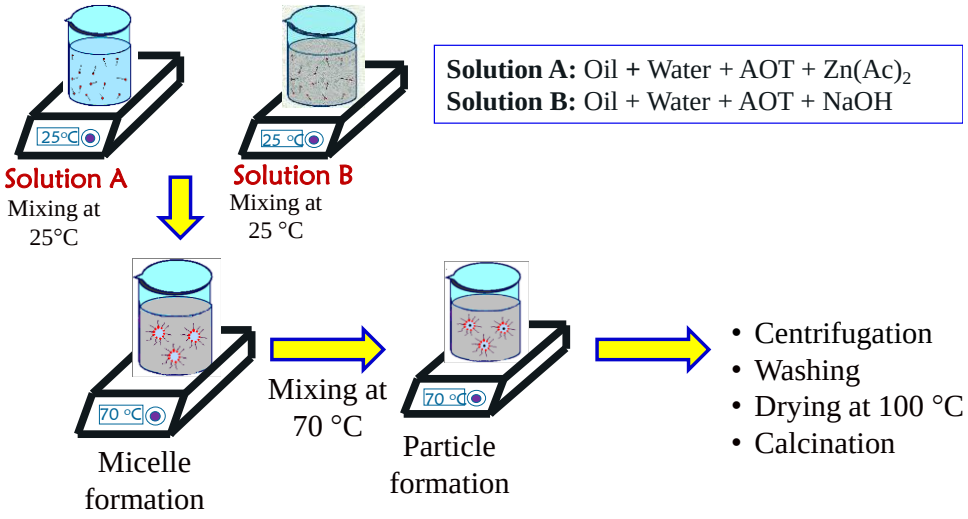

Figure 3.2. A schematic representation of experimental procedure for synthesis of ZnO nanoparticles with microemulsion method.

3.2.3 Materials characterization

X-ray diffraction (XRD) analyses were performed for phase identification of microemulsion products in *as-prepared* (dried at 100 °C for 1 h) and after calcination treatments. A Rigaku D/Max-2000 PC diffractometer was employed in XRD analyses, using Cu-Kα radiation (λ=1.54 Å) and x-ray source operating voltage of 40 kV in the 2θ range of 3-90° at a rate of 2°/min. The average crystallite size for the powders (D, in nm) was estimated by Scherrer's equation using the XRD line broadening method;

$$D = 0.9\lambda/\beta \cos\theta \qquad 3.1$$

where, λ is the x-ray wavelength for CuKα , β is the full width in radians at half-maximum (FWHM) of the diffraction line and θ is the diffraction angle. (110) diffraction peak (at 2θ≈56.61°) was chosen to determine a representative particle size for ZnO nanoparticles by employing the Scherrer's equation.

The morphology and size of the ZnO particles was also examined by using a FEI Quanta 400F model field emission scanning electron microscope (FESEM). The SEM samples were obtained from a suspension of ZnO particles dispersed in distilled water

by ultrasonic treatment. A few drops of dilute dispersion were then deposited onto a carbon film on an aluminum grid and dried in air. FESEM examinations were performed without any conductive coating.

Thermogravimetric analyses (TGA) and differential scanning calorimetry (DSC) experiments were carried out using Setaram SETSYS–16/18 on finely ground powders in air atmosphere between 30-700 °C with a heating rate of 5 °C/min.

Photoluminescence (PL) measurements were conducted at room temperature with the HeCd laser and Hamamatsu CCD camera with a range of 300 to 800 nm.

3.3 Results

The XRD diffractograms of microemulsion products prepared using different surfactant amount (microemulsion formulations S1.1, S1.2, S1.3 and S1.4) are shown in Figure 3.3. Figure 3.3 (a) and (b) exhibit the phases of the reaction products in as-prepared condition and after calcination at 500 °C for 3h. For S1.5 formulation, no-stable phase separation was observed in the emulsion state, so it has been excluded. For the as-prepared samples prepared with increasing surfactant amount, there is no obvious differences in the XRD patterns. All XRD patterns of the particles coincide with that of zinc glycerolate (Zn-Gly, with JCPDS card number 23-1975) and no other crystalline phase besides zinc glycerolate was observed. After calcination the zinc glycerolate intermediate microemulsion precursor decomposes to crystalline ZnO (hexagonal wurtzite structure, with JCPDS card no: 36-1451).

Figure 3.4 shows the SEM micrographs of ZnO particles prepared under different surfactant amount (microemulsion formulations S1.1, S1.2, S1.3 and S1.4) after calcination for 3 h at 500 °C. From microemulsion formulations of S1.1, S1.2 and S1.3, the ZnO nanoparticles exhibit a spherical morphology with a narrow and uniform size distribution. The average particle size decreases with increasing surfactant amount. With further increasing surfactant amount, rod-like ZnO nanoparticles were obtained. The average crystallite size calculated from XRD patterns and average particle size determined from SEM micrographs are listed in Table 3.3.

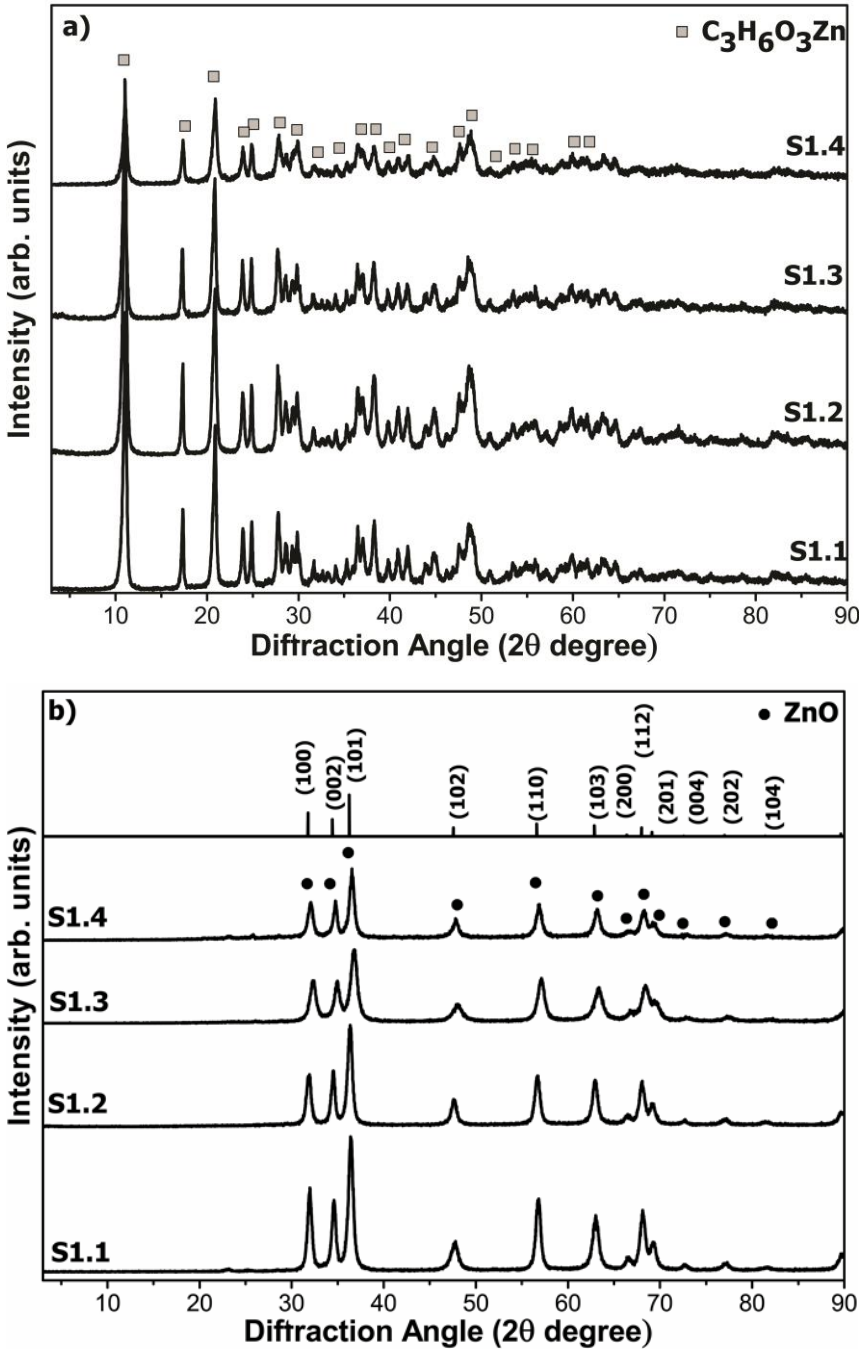

Figure 3.3. XRD diffractograms of microemulsion products for Series-1 microemulsion formulations (S1.1, S1.2, S1.3 and S1.4) in (a) as-prepared condition (for precursor zinc-complex) and (b) after 3 h calcination in air at 500 °C.

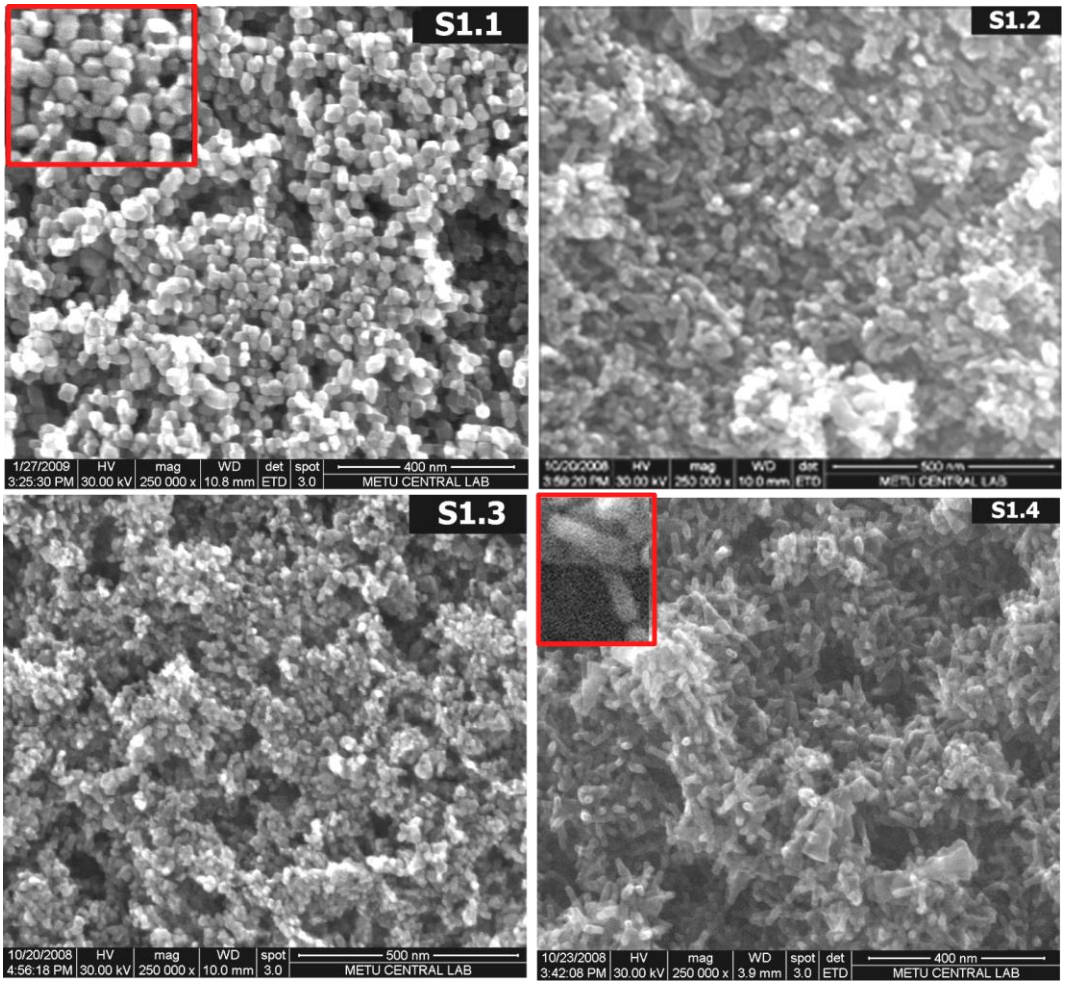

Figure 3.4. SEM micrographs of ZnO nanoparticles obtained using Series-1 microemulsion formulations (S1.1, S1.2, S1.3 and S1.4) (calcined in air at 500 °C, 3h).

Table 3.3. Average crystallite size calculated from XRD patterns and average particle size determined from SEM micrographs.

Sample Name	XRD crystallite size (nm)	SEM particle size (nm)
S1.1	26.8	24 ± 1
S1.2	25.7	21.6±1
S1.3	24.8	20 ± 1
S1.4	37.5	d: 25 ± 1 l: 70 ± 1

d: diameter
l: length

In order to investigate calcination temperature treatment on the size and morphology of the microemulsion products, three different calcination temperature (300, 400 and 500 °C) were applied to as-prepared sample. Figure 3.5 shows the XRD diffractograms of the microemulsion products for both formulations S.1.1 and S1.2, in as-prepared condition and after calcination for 3 h at 300 °C, 400 °C and 500 °C. For both microemulsion systems the XRD patterns of the particles in as-prepared condition coincide with that of zinc glycerolate (Zn-Gly, with JCPDS card number 23-1975) and no other crystalline phase besides zinc glycerolate was observed. After calcination the zinc glycerolate intermediate microemulsion precursor decomposes to crystalline ZnO (hexagonal wurtzite structure, with JCPDS card no: 89-0510). For S1.1, this decomposition completes at 300 °C. ZnO obtained in S1.2 microemulsion still contained some residual zinc glycerolate after calcination at 300 °C. For both systems calcination at 400 °C or 500 °C results in phase pure crystalline ZnO powder. Another distinction between XRD patterns of ZnO particles synthesized in S1.1 or S1.2 system is the difference in relative intensities of the certain diffractions. The JCPDS card of crystalline ZnO is also presented as an inset in Figure 3.5 for comparison purposes and shows the relative intensities for the possible diffractions. For all calcination treatments, the diffraction peak intensities of the ZnO product S1.1 show a better match with the standard card in terms of intensity order for the diffraction events. The XRD patterns of ZnO particles, synthesized in S1.2 systems and calcined at 300 °C or 400 °C, on the other hand show a distinct deviation from the standard pattern in relative intensities of the observed diffractions. For the ZnO powder of S1.2, calcined at 500 °C, the diffraction peak intensities and their order are again in agreement with standard card intensities. The reasons for such differences will be further clarified in the discussion section of this chapter.

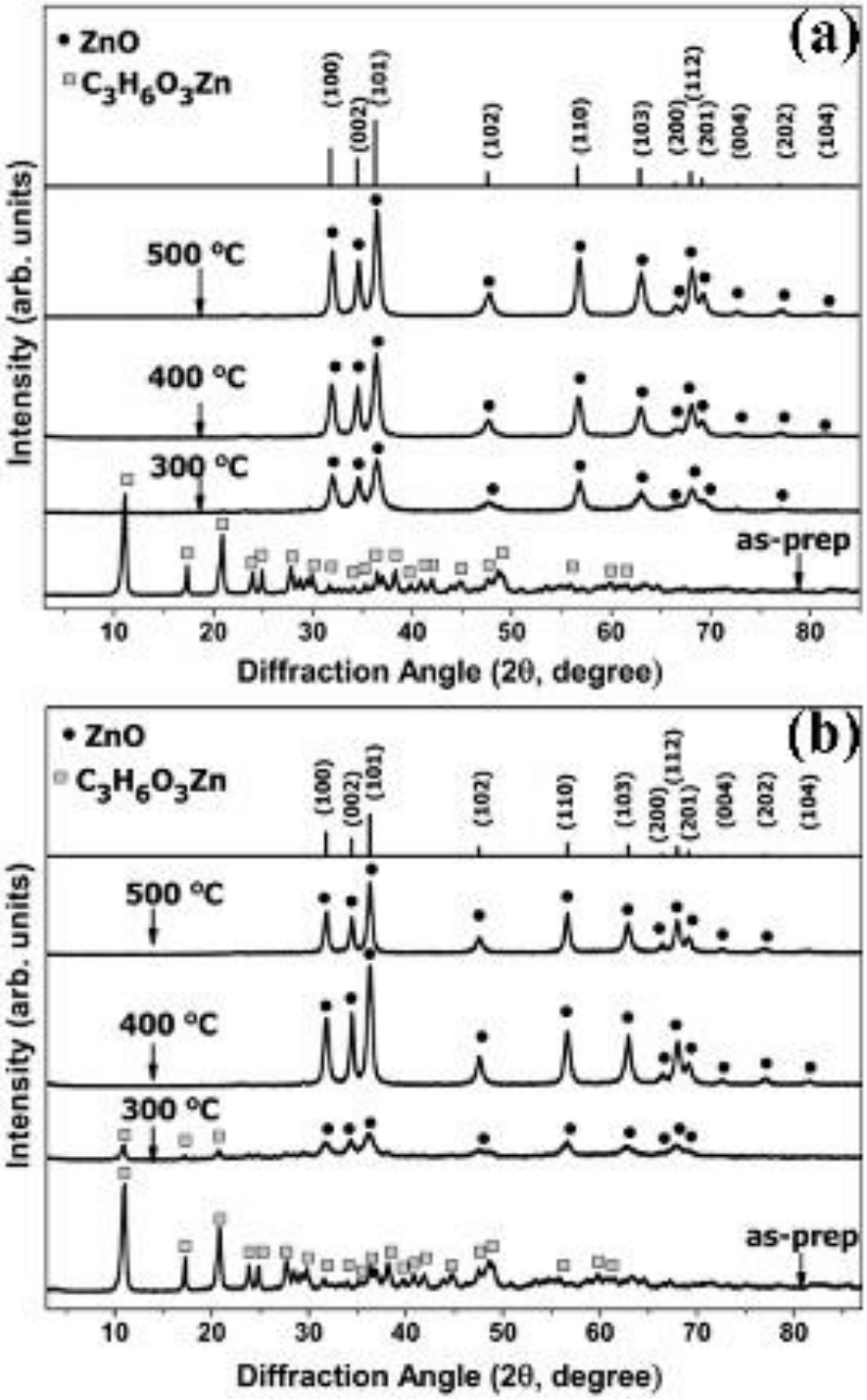

Figure 3.5. XRD diffractograms of microemulsion products in as-prepared condition (for precursor zinc-complex) and after 3 h calcination in air at different temperatures for two microemulsion formulations: (a) S1.1 and (b) S1.2. The inset shows the relative intensities of the standard ZnO (with JCPDS card No. 36-1451) diffraction pattern.

TGA-DSC results of the microemulsion products in as-prepared condition obtained by heating from room temperature to 700 °C in air are shown in Figure 3.6. (a) and (b). According to TGA curves of S1.1 and S1.2, there is a very small amount of weight loss (around 2 wt.%) up to 200 °C. The broad exothermic events (280-450 °C range) in DSC curves are attributed to decomposition of zinc glycerolate complex to ZnO and crystallization of ZnO, respectively. The DSC and TGA data are somewhat in agreement with each other, as the temperatures of the broad exothermic peak coincide with the temperature ranges of the main weight loss. However, the DSC curves show two exothermic peaks. The first sharp peak at around 340 °C corresponding to the main weight loss in TGA curves is attributed to the decomposition of Zn-Gly particles to ZnO. The second exothermic peak indicates that there must be another reaction such as volatilizing, combustion of organics accompanying the decomposition of Zn-Gly [11]. Absence of weight loss or heat flow change above 450 °C indicates that no reaction takes place beyond 450 °C.

Figure 3.7 shows the SEM micrographs of ZnO particles of S1.1 system after calcination for 3 h at 300 °C, 400 °C and 500 °C. The ZnO nanoparticles exhibit a spherical morphology with a narrow and uniform size distribution. The average particle size varies in the range of 15-25 nm and increases with calcination temperature within the temperature range of the study, i.e. 300-500 °C. Calcination at 500 °C also initiates sintering of the particles by neck formation between the particles at higher temperatures as shown in the Figure 3.7.

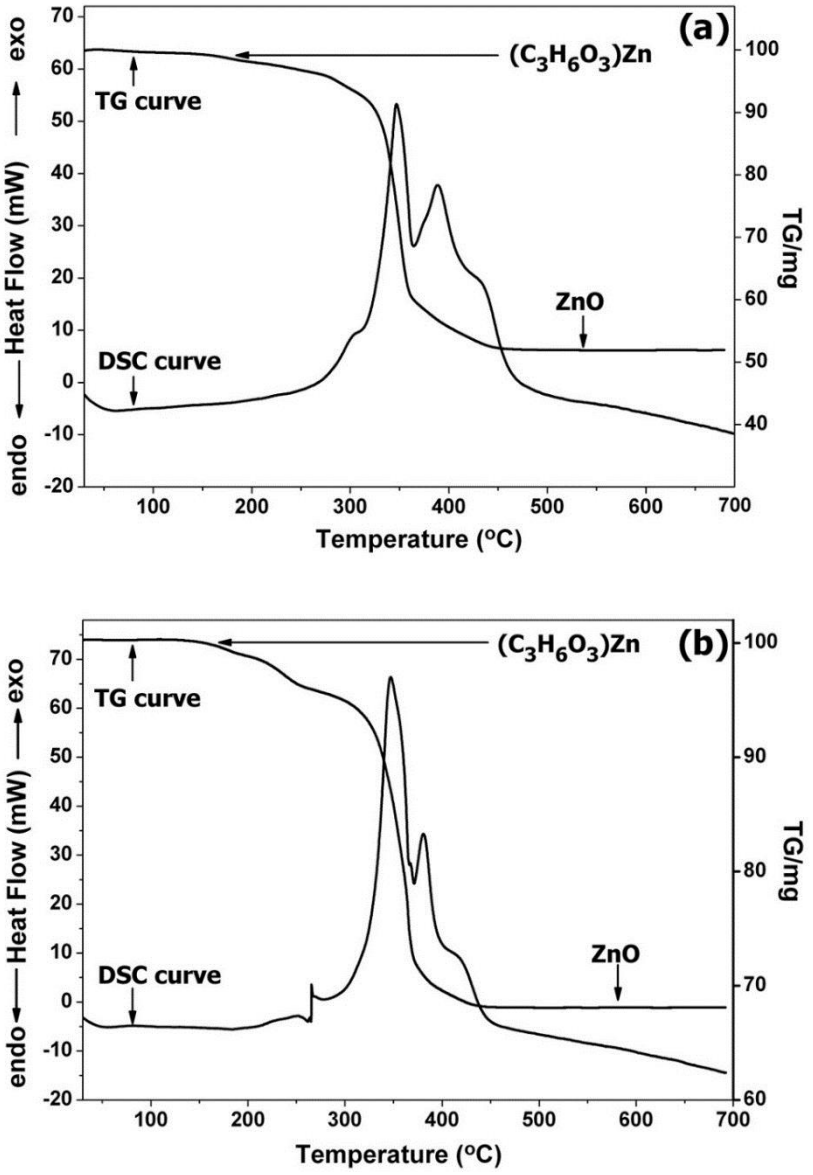

Figure 3.6. TGA and DSC plots for decomposition of the precursor microemulsion products (i.e. zinc glycerolate particles) for two microemulsion formulations: (a) S1.1 and (b) S1.2.

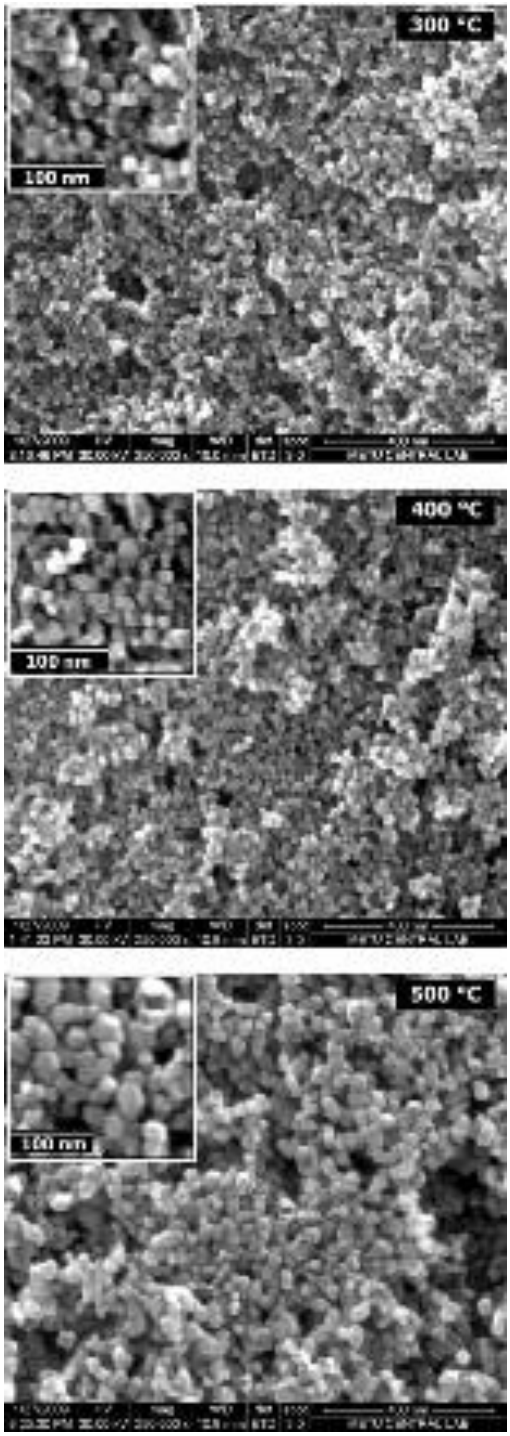

Figure 3.7. SEM micrographs of the ZnO nanoparticles of the microemulsion S1.1 calcined at 300, 400 and 500 °C. The insets are the segments from the underlying SEM images magnified (2X) as a visual aid indicating dimensional details.

For sample S1.1, the energy dispersive x-ray (EDX) and elemental mapping analysis of Zn and O elements are shown in Figure 3.8. EDX data revealed that the particles were composed of Zn and O elements with an atomic Zn:O proportion of 49.45:50.55, close to the stoichiometric ratio of 1:1. The elemental mapping images also confirmed homogeneous distribution of zinc and oxygen suggesting highly pure and stoichiometric ZnO nanoparticles.

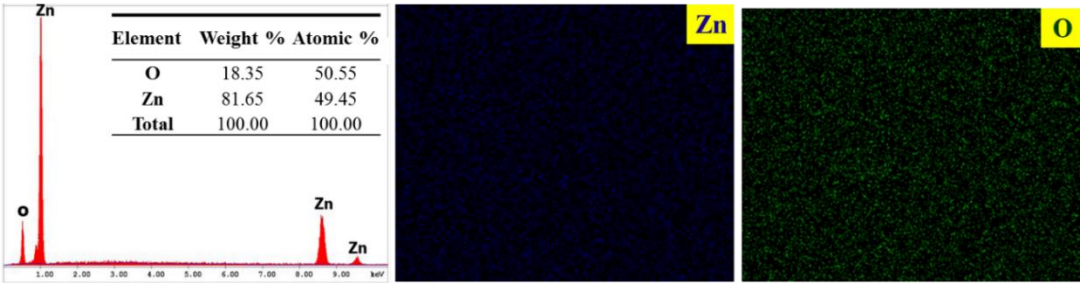

Figure 3.8. EDX spectrum and elemental (Zn and O) mapping images of sample S1.1.

SEM micrographs of microemulsion products after same calcination treatments for the second microemulsion system S1.2 are shown in Figure 3.9. Particles of S1.2 calcined at 300 °C and 400 °C exhibit a distinctly different morphology compared to those for S1.1 and have a rod-like morphology again with a narrow size distribution. The length of the rods is approximately 65-70 nm, with a typical diameter of 22-28 nm. ZnO particles of S1.2 calcined at 500 °C on the other hand have a spherical morphology as shown in Figure 3.9 with an average particle size of 22 nm. The average particle sizes of the ZnO powders determined from SEM examinations are listed in Table 3.4, together with the estimated values by Scherrer's equation.

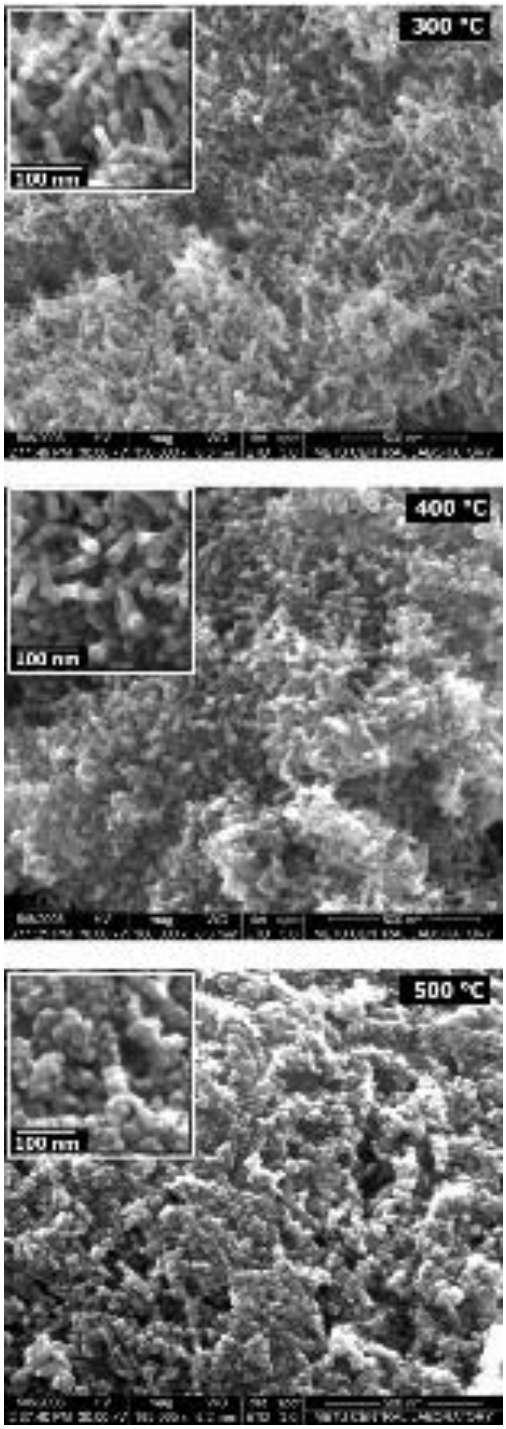

Figure 3.9. SEM micrographs of the ZnO nanoparticles of the microemulsion S1.2 calcined at 300, 400 and 500 ◦C. The insets are the segments from the underlying SEM images magnified (2X) as a visual aid indicating dimensional details.

Table 3.4. Average crystallite size estimated from the XRD results and average particle size as determined from SEM examinations for the ZnO nanoparticles calcined at different temperatures.

Microemulsion formulation	**S1.1**		**S1.2**	
Calcination Temperature	**XRD crystallite size (nm)**	**SEM particle size (nm)**	**XRD crystallite size (nm)**	**SEM particle size (nm)**
300 °C	16.4	15±1	n.a.	d: 22±3 l: 66±3
400 °C	28.8	18±0.5	41	d: 28±1 l: 72±1
500 °C	26.8	24±1	31.7	21.6±1

n.a.: not available
d: diameter
l: length

Figure 3.10 shows the PL spectra of ZnO nanoparticles obtained S1.1 and S1.2 and calcined at different temperatures. As shown in Figure 3.10 (a), the PL spectra of S1.1 products consists of a weak UV emission peak (385 nm) as shown in the inset of the figure and strong deep-level green emission peak (530 nm). The intensity of weak UV emission band decreases with increasing calcination temperature but the intensity of strong green emission increases with calcination temperature. Figure 3.10(b) presents PL spectra of S1.2 products. There is only strong deep-level green emission peak and it becomes stronger with increasing calcination temperature resulting in an enhanced green emission.

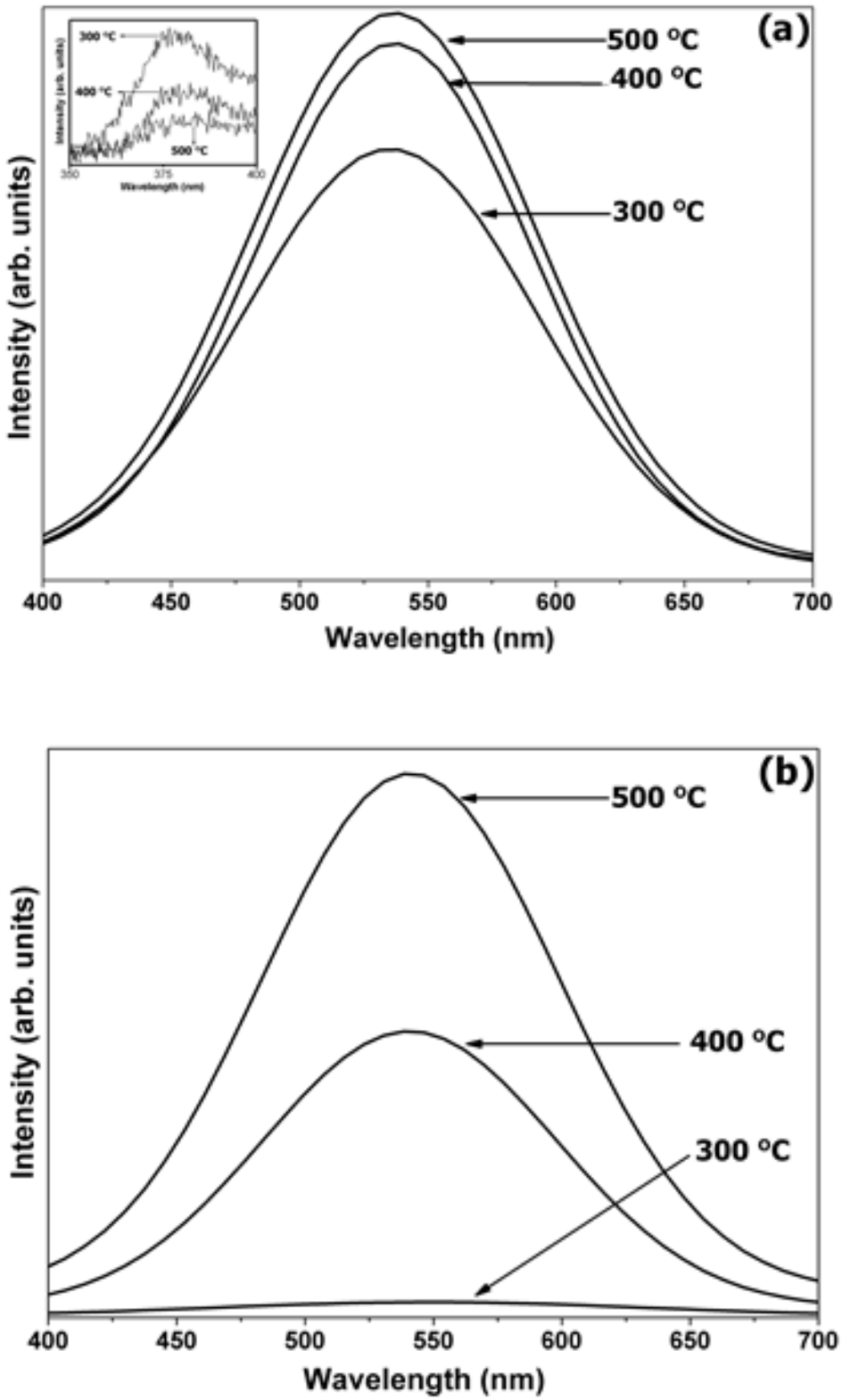

Figure 3.10. Room temperature PL spectra of the ZnO nanoparticles calcined at 300, 400 and 500 °C for two microemulsion formulations: (a) S1.1 and (b) S1.2.

Figure 3.11 (a) and (b) show XRD patterns of microemulsion products for Series-2 microemulsion formulations (S1.1, S2.2, S2.3, S2.4 and S2.5) in as-prepared condition (for precursor zinc-complex) and after 3 h calcination in air at different 500 °C, respectively. In Series-2 formulations, surfactant amount is constant at 5% and water amount increase from 5% to 90% for S1.1 and S2.5, respectively. All diffraction patterns match with Zn-Gly for samples in as-prepared condition and wurtzite type ZnO crystal structure for the samples after calcination.

Figure 3.12 exhibits low and high magnification SEM micrographs of microemulsion products for S2.2 and S2.3 formulations, respectively. For S2.2, the low magnification SEM image shows that reaction product has flower structure consisting of ZnO plate structures. With increasing water amount to 50% (S2.3), morphology of the ZnO structure changes to micro-plate structure. High magnification micrographs of the S2.2 and S2.3 formulations indicate that both flower and plate structure are constituted of spherical nanoparticles with ~20 nm average particle size.

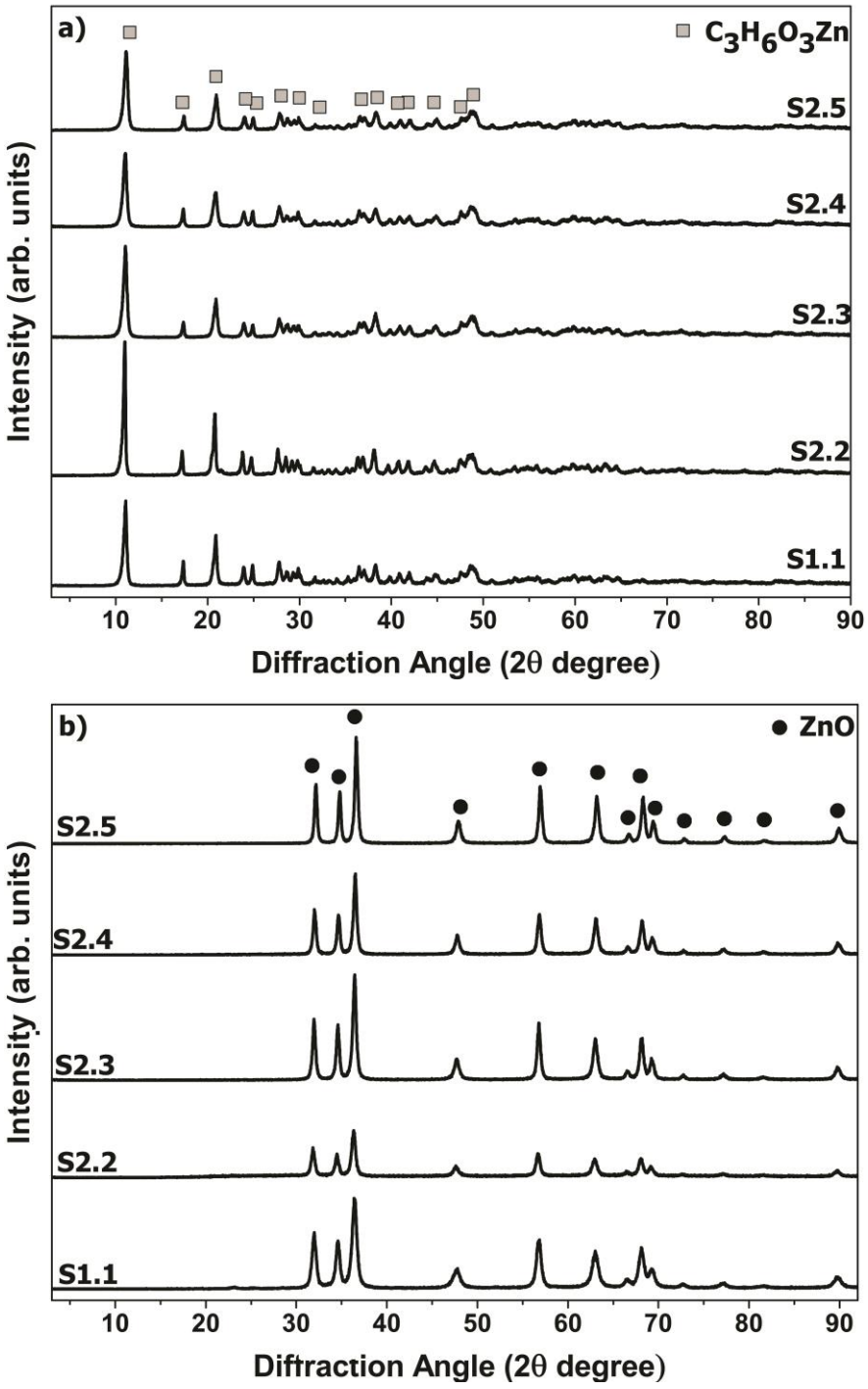

Figure 3.11. XRD patterns of microemulsion products for Series-2 microemulsion formulations (S1.1, S2.2, S2.3, S2.4 and S2.5) in (a) as-prepared condition (for precursor zinc-complex) and (b) after 3 h calcination in air at 500 °C.

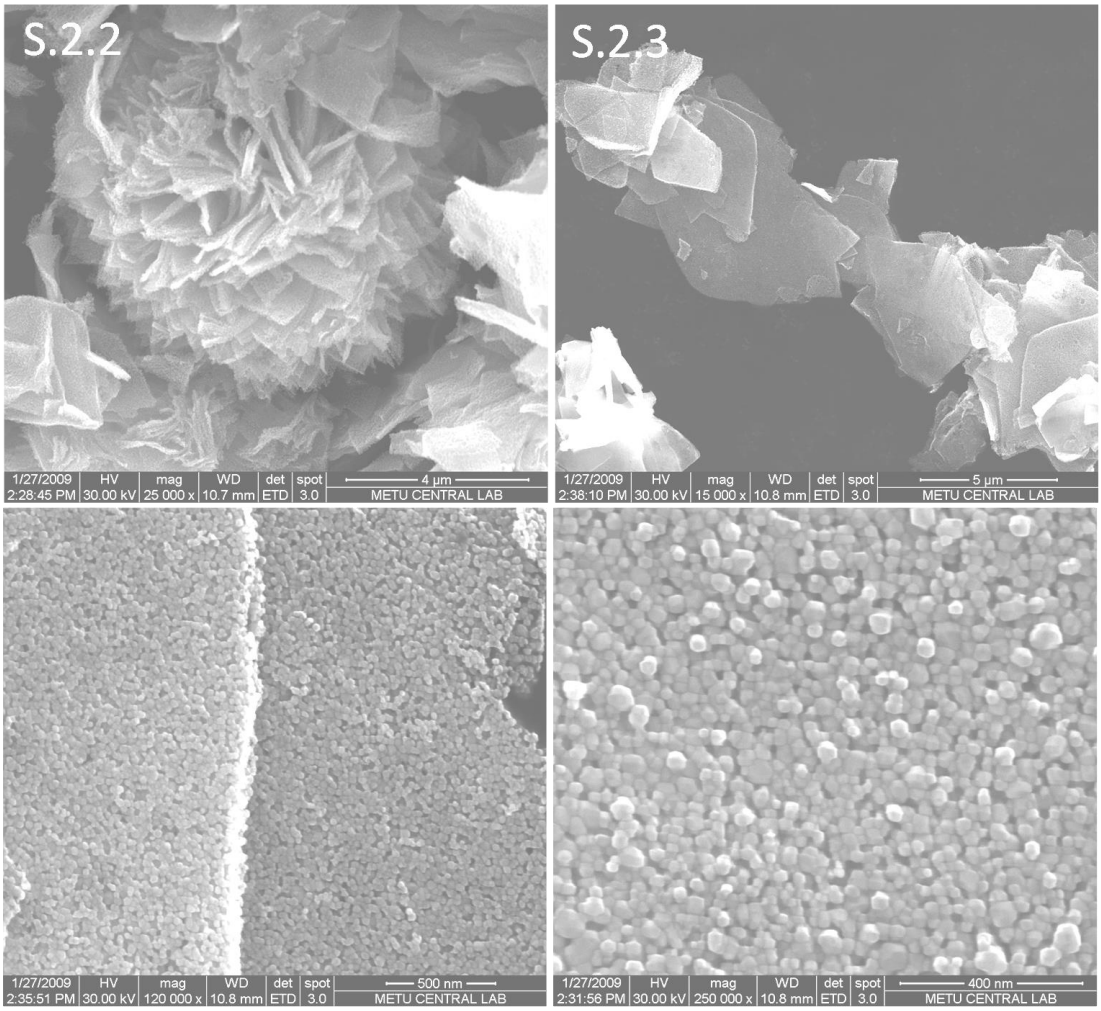

Figure 3.12. SEM micrographs of microemulsion product for microemulsion formulations of S2.2 and S2.3 prepared after 3 h calcination in air at 500 °C.

3.4 Discussion

A reverse microemulsion system has been employed to synthesize ZnO nanoparticles with different size and morphology. A water-in-oil microemulsion acting as nanoreactor for Zn-complex formation was obtained when glycerol droplets are surrounded by AOT surfactant molecules in n-heptane oil phase. In such a water-in-oil microemulsion system; AOT dissolves in the dispersed phase and form stable micelles reach in Na^+ ions. When Zn^{2+} ions are incorporated ion exchange reaction takes place and finally Na^+ replaces with Zn^{2+} in the dispersed micelles [12]. The Zn-Gly complex

acting as a precursor for ZnO formation was synthesized in the presence of NaOH, because the reaction between zinc acetate and glycerol is much faster in basic environment and as Zn-Gly decomposes in acidic solutions [13]. In other words, NaOH was used as electrolyte providing glycerol stabilization in n-heptane and provides rigidity for the droplet interfacial film and so the stability of droplet size [14]. As can be noted from the XRD and thermal analyses, formation of ZnO originates from the decomposition of Zn-Gly complex precursor, whose morphology is most likely controlled by the shape of the nanoreactors in the microemulsion system which does not change their shape during thermal decomposition to ZnO. In this sense, nucleation and growth of ZnO crystals occur in the definite shape of this precursor upon subsequent thermal treatment.

One obvious effect of surfactant amount in the studied microemulsion system is on particle morphology. Higher surfactant concentration results in rod-like nanoreactors and eventually rod-like ZnO products as can be seen for the S1.2 microemulsion products calcined at 300 °C and 400 °C. Formation of rod-like nanoreactors in the presence of higher amount of surfactants is analogous to that reported by others [2, 15]. As shown by the schematics in Figure 3.13 a low surfactant concentration beyond critical micelle concentration favors the formation of spherical water-in-oil droplets, so formation of spherical ZnO particles as in the case of S1.1 Whereas higher surfactant concentration favors development of interconnected cylindrical droplets, and generates rod-like ZnO particles as in the case of S1.2. This compositional modification in the microemulsion formulation in fact gives a chance to control the final particle morphology at nano scale.

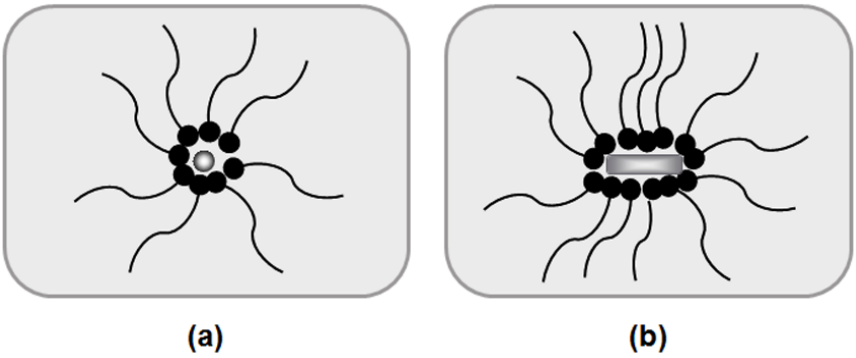

Figure 3.13. Schematic illustration for the formation of different ZnO morphologies: (a) in microemulsion formulation S1.1 that has low surfactant amount and (b) in microemulsion formulation S1.2 with higher surfactant content.

Another finding related with the physical difference for two microemulsion products is the change in the average particle size and morphologies with the calcination temperature. For the all calcination temperatures employed, the ZnO powders of S1.1 microemulsion formulations are typically spherical and exhibited bigger sizes with increasing calcination temperature. Similar observations have also been reported by other researchers [16]. On the other hand, S1.2 microemulsion products after calcination at 300 and 400 °C had a rod-like morphology and exhibited a structural rod-to-sphere shape transformation at higher calcination temperatures (500 °C). While the SEM observations clearly demonstrate such differences, the XRD data also provide indirect evidence. The intensity order of the diffractions of the ZnO products of S1.1 shows a complete match with the intensities listed standard JCPDS card data, which corresponds the most random arrangement of crystal planes for powder crystal sample. The ideal intensity order, corresponding most random is crystal arrangement is actually presentation of the thermodynamically most stable arrangement which can be approximated by spherical morphology. ZnO products of S1.2 calcined at 300 °C and 400 °C however show some deviation from the standard intensity order; and have relatively more intense (002) diffraction peaks compared to standard card data. This indicates presence of preferred crystallographic orientation, here a rod-like, of ZnO crystals for this particular microemulsion formulation with higher amount of surfactant.

The observation regarding the calcination temperature dependent structural rod-to-sphere shape transformation change may results from size and defect controlled thermodynamic factors. It has been reported that gold nanorods can be transformed into sphere-like nanoparticles by photo induced processes leading to a thermal excitation and allowing a shape transformation to the energetically more stable spherical shape [17]. Similar transition for ZnO nanorods may occur during thermal heating at temperatures approaching to sintering temperatures.

Increasing calcination temperature also affect the particle size of the rod-like ZnO powders of S1.2 as shown in Figure 3.9 (a)-(b). Lu et al. studied microemulsion mediated hydrothermal synthesis of TiO_2 particles [18]. They showed that the aspect ratio of rod-like TiO_2 particles decreases with an increase in synthesis temperature. In the present study, same behavior in the size of rod-like ZnO particles has been observe as a result of increasing calcination temperature. While length and diameter of the rod-like ZnO particles increase from 66±3 nm and 22±3 nm to 72±1 nm and 28±1 nm, respectively, the aspect ratio (length/diameter) of the rod-like ZnO nanoparticles decreases from 3.0 to 2.6 with an increase in calcination temperature of 300 °C to 400 °C. This decrease in aspect ratio again implies a morphological approximation to a more equiaxed shape with increasing calcination temperature.

Figure 3.14 shows the stable microemulsion regions in a selected (water/oil/surfactant) ternary emulsion system to synthesize different size and morphology of ZnO nanostructures. Morphology control was achieved by using different surfactant concentrations. Spherical nanoparticles and rod-like nanostructures were synthesized at low and high surfactant concentrations, respectively. At too high surfactant (S1.5) addition to the microemulsion system, phase separation between oil and water components has been observed instead of microemulsion formation.

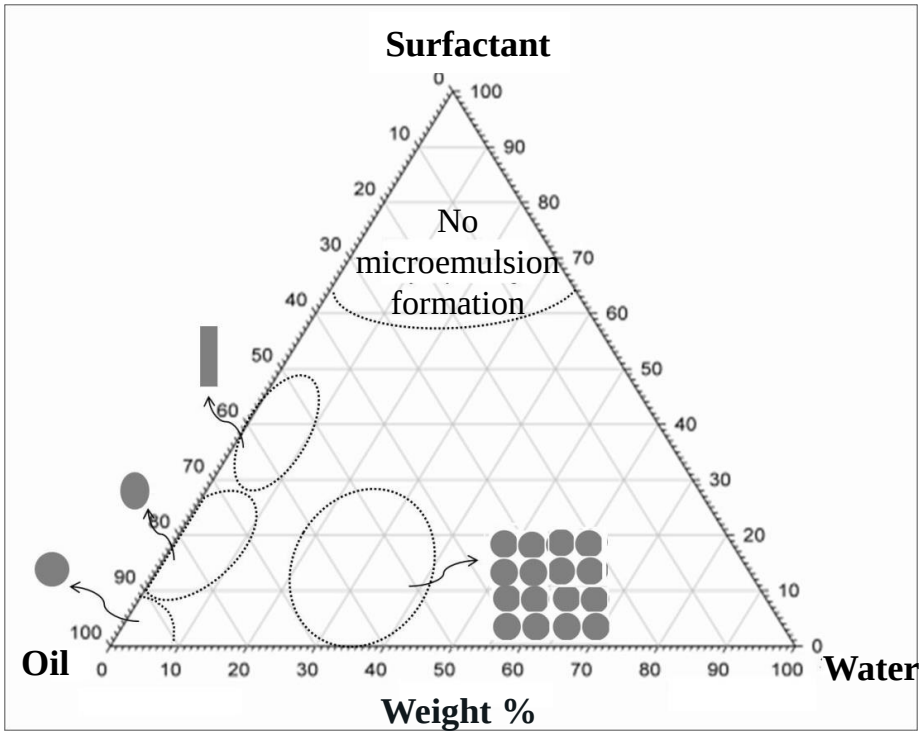

Figure 3.14. Ternary phase diagram of surfactant-oil-water microemulsion system.

In regard to optical properties, the relatively weak UV emission peak at around 385 nm attributed to the exciton combination emission indicates a passivated surface for the ZnO nanoparticles. The quenching of UV-emission may be due to surface defects in the form of OH group [19, 20]. The strong deep-level green emission at around 530 nm resulting from the defects associated with oxygen vacancies or zinc interstitials implies a populated defect concentration for ZnO crystals of the both microemulsion products S1.1 and S1.2. A higher calcination temperature enhances the green emission intensity suggesting a correlation between green emission and isolated oxygen vacancies as proposed by others [21]. With increasing calcination temperature; the kinetic energy of atoms in ZnO lattice will increase and the escape rate of oxygen atoms from ZnO lattice will be faster than rate of getting oxygen atoms to lattice [22] resulting in more vacancy formation and higher green emission.

3.5 Conclusions

Synthesis of ZnO nanoparticles was achieved by a modified reverse microemulsion with Aerosol OT serving as surfactant and glycerol serving as water phase. By employing of glycerol as an internal phase in the microemulsion formulation it was possible to obtain an intermediate zinc-complex rather direct precipitation of zinc oxide crystals as the microemulsion product in preventing formation agglomerated products. The intermediate zinc glycerolate complex was converted to zinc oxide by thermal decomposition during subsequent calcination. In this way monodispersed spherical ZnO nanoparticles with average particle size of 15 nm were successfully obtained. Particle size control of the spherical ZnO nanoparticles was achieved by changing the calcination temperature, i.e. 15±1 nm (300 °C), 18±1 nm (400 °C) and 24±1 nm (500 °C). Hence, the proposed microemulsion system is advantageous for obtaining size controlled ZnO nanoparticles with narrow size distribution. In addition, the proposed system also allows attaining variation in ZnO morphology which can be achieved by controlling surfactant amount in the microemulsion formulation. Higher surfactant concentrations and calcination temperatures not exceeding 400 °C promotes formation rod-like ZnO microemulsion products with typical diameter of ~25 nm and length of 60-70 nm. The findings of the study indicated that the suggested modified microemulsion method provides an alternative approach for synthesis of ZnO nanoparticles by a simple wet chemical route which also enables tailoring the size and morphology of the ZnO nanoparticles. However, low product yield and the requirement of calcination to convert as-prepared microemulsion product to ZnO are the main disadvantages of microemulsion technique.

3.6 References

1. Danielsson I. and Lindman B., Colloids and Surfaces, **1981** 3(4) p. 391-392.

2. Li X., He G., Xiao G., Liu H., and Wang M., Journal of Colloid and Interface Science, **2009** 333(2) p. 465-473.

3. Hingorani S., Pillai V., Kumar P., Multani M.S., and Shah D.O., Materials Research Bulletin, **1993** 28(12) p. 1303-1310.

4. Lu C.-H. and Yeh C.-H., Materials Letters, **1997** 33(3–4) p. 129-132.

5. Moleski R., Leontidis E., and Krumeich F., Journal of Colloid and Interface Science, **2006** 302(1) p. 246-253.

6. Inoguchi M., Suzuki K., Kageyama K., Takagi H., and Sakabe Y., Journal of the American Ceramic Society, **2008** 91(12) p. 3850-3855.

7. Guo L., Ji Y.L., Xu H., Simon P., and Wu Z., Journal of the American Chemical Society, **2002** 124(50) p. 14864-14865.

8. Liu Y., Liu Z., and Wang G., Journal of Crystal Growth, **2003** 252(1–3) p. 213-218.

9. Tokeer A., Sonalika V., Niladri S., Subhasis G., and Ashok K.G., Nanotechnology, **2006** 17(5) p. 1236-1240.

10. Lv Y., Guo L., Xu H., Ding L., Yang C., Wang J., Ge W., Yang S., and Wu Z., Journal of Applied Physics, **2006** 99(11) p. 114302-1-4.

11. Yang Y., Chen H., Zhao B., and Bao X., Journal of Crystal Growth, **2004** 263(1–4) p. 447-453.

12. Singhai M., Chhabra V., Kang P., and Shah D.O., Materials Research Bulletin, **1997** 32(2) p. 239-247.

13. Fairlie D.P., Whitehouse M.W., and Taylor R.M., Agents and Actions, **1992** 36(1-2) p. 152-158.

14. Liu D., Ma J., Cheng H., and Zhao Z., Colloids and Surfaces A: Physicochemical and Engineering Aspects, **1998** 143(1) p. 59-68.

15. Sun G., Cao M., Wang Y., Hu C., Liu Y., Ren L., and Pu Z., Materials Letters, **2006** 60(21–22) p. 2777-2782.

16. Kwon Y.J., Kim K.H., Lim C.S., Shim K.B., J. Ceram. Processing Res., **2002** 3 p. 146-149.

17. Link S., Wang Z.L., and El-Sayed M.A., The Journal of Physical Chemistry B, **2000** 104(33) p. 7867-7870.

18. Lu C.-H., Wu W.-H., and Kale R.B., Journal of Hazardous Materials, **2008** 154(1–3) p. 649-654.

19. Zhou H., Alves H., Hofmann D.M., Kriegseis W., Meyer B.K., Kaczmarczyk G., and Hoffmann A., Applied Physics Letters, **2002** 80(2) p. 210-212.

20. Zhou H., Alves H., Hofmann D.M., Kriegseis W., Meyer B.K., Kaczmarczyk G., and Hoffmann A., Applied Physics Letters, **2002** 80(2) p. 210-212.

21. Yadav H.K., Sreenivas K., Gupta V., Singh S.P., and Katiyar R.S., Journal of Materials Research, **2007** 22(9) p. 2404-2409.

22. Vanheusden K., Seager C.H., Warren W.L., Tallant D.R., Caruso J., Hampden-Smith M.J., and Kodas T.T., Journal of Luminescence, **1997** 75(1) p. 11-16.

CHAPTER 4

SYNTHESIS OF ZnO NANOSTRUCTURES BY PRECIPITATION METHOD: EFFECT OF PRECIPITATION TEMPERATURE AND ORGANIC ADDITIVES ON SIZE AND MORPHOLOGY OF ZnO NANOPARTICLES

4.1 Introduction

Being able to tune the electrical and optical properties of semiconductor nanomaterials during synthesis is quite critical, as control of the size and morphology may allow enhancement in these properties. Zinc oxide (ZnO) is a semiconductor with a wide direct band gap (3.37 eV) and a large exciton binding energy (60 meV), and it has many potential applications in electronic and optoelectronic devices such as varistors [1, 2], gas sensors [3, 4], field emitters [5, 6] and solar cells [7, 8]. Due to different functional requirements in these applications, a variety of techniques ranging from gas phase processes to solution routes including hydrothermal method [9, 10], spray pyrolysis [11, 12], sol-gel process [13, 14] and microemulsion method [15, 16] have been employed to synthesize ZnO nanostructures with different physical properties. However, high synthesis temperature, long synthesis periods, high vacuum requirements or sophisticated equipment necessities make these methods unfavourable for large scale production. Therefore, synthesis of highly crystalline ZnO nanostructures with proper size and morphology control under mild synthetic conditions still remains as a challenge.

As an alternative route, aqueous precipitation method attracts particular interest since it allows convenient control of particle size and morphology for facile scale-up. A survey of literature shows that special morphologies of ZnO nanostructures such as rod [17], wire [18], star-like [19] or ellipsoidal [20] can be obtained via solution based

methods and subsequent heat treatments. Meanwhile, little attention has been paid room temperature synthesis of size and morphology controlled highly crystalline ZnO nanoparticles at short synthesis periods.

The objective of the study was to establish a simple approach for the synthesis of size and morphology controlled ZnO nanoparticles at around room temperature. A zinc salt (zinc acetate dihydrate) was used as zinc source and ethylene glycol (EG) or DI-water were employed as solvents and polyvinyl pyrrolidon (PVP) as chelating agent. Size control of ZnO nanoparticles at nearly 10 nm with narrow size distribution was achieved by modifying the processing parameters, including precipitation temperature and amount of chelating agent. Morphology of the nanostructures was controlled by using different solvents. The effects of these parameters on resultant ZnO nanoparticles were investigated and described in detail. The correlation between precipitation temperature, chelating agent concentration, solvent type and the size/morphology of resultant ZnO nanoparticles has been established in connection with a proposed precipitation mechanism.

4.2 Experimental methods

4.2.1 Materials

The chemicals used during synthesis of pure ZnO nanoparticles with precipitation method are listed in Table 4.1. All reagents were used without further purification. Ultrapure deionized (DI) water used during reactions was obtained by using Human Corporation Zeneer Power I water purification system.

Table 4.1. Materials used in the experimental part of the synthesis of pure ZnO nanoparticles with precipitation method, their formulas and sources.

Material	Chemical Formula	Grade	Source
Zinc acetate dihydrate	$C_4H_6O_4Zn{\cdot}2H_2O$	99.5%, powder	Fluka
Polyvinyl pyrrolidon, PVP	$(C_6H_9NO)_n$	MW ~55000	Aldrich
Sodium hydroxide	NaOH	97%, pellets	Merck
Ethylene glycol, EG	$C_2H_6O_2$	99%, solution	Merck

4.2.2 Experimental procedures

Zinc acetate dihydrate in a quantity of 0.4 g was dissolved in 15 mL EG at 25 °C. Meanwhile, 0.2 g PVP containing 10 mL EG solution was prepared at 25 °C. Both solutions were stirred for 1 h to achieve complete homogenization. Then, zinc acetate dihydrate solution was added dropwise into PVP-containing solution in 5-s intervals and final solution was further stirred for 15 min at 25 °C. Finally, 2 M NaOH (20 mL) solution was added dropwise into the parent solution in 1 h and the pH of the final solution was measured as 12.7. After addition of NaOH, the solution took a milky appearance and it was aged by refluxing for 30 min at 25 °C. Then the solid extracts were collected by centrifugation at 10,000 rpm (using Eppendorf 5804 model, with a rotor radius of 115 mm, Eppendorf AG, Hamburg, Germany) for 10 min and washed five times with DI-water. The powder products were dried at 70 °C for 3 h in a vacuum dryer and no further thermal treatment was performed. This synthesis procedure described above can be considered as standard protocol. The same experimental protocol was also repeated by changing the reflux temperature to 60, 70 and 80 °C. In addition, to investigate the effect of changing the PVP quantity, standard protocol was repeated by replacing 0.2 g PVP-containing EG solution with 0.3 or 0.4 g PVP-containing EG solution. Likewise, to examine solvent effect on size and morphology of ZnO particles, the standard protocol was modified where DI-water was used instead of EG as a solvent. All experimental studies were carried in ambient air. Figure 4.1 shows a schematic representation of experimental procedure for synthesis of ZnO nanoparticles with precipitation method. Table 4.2 summarizes the precipitation conditions and reactants used in all experiments.

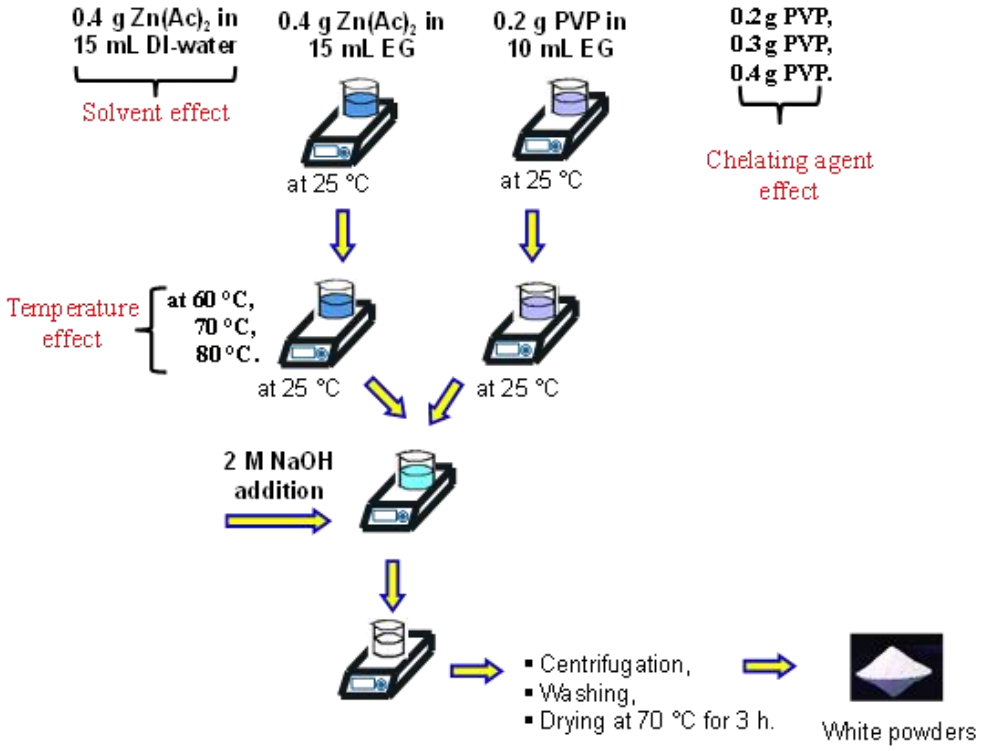

Figure 4.1. Schematic representation of experimental procedures applied during precipitation reactions.

Table 4.2. Synthesis parameters of ZnO nanoparticles (EG: Ethylene glycol, PVP: Polyvinyl pyrrolidon).

Temperature (°C)	Solvent type	PVP (grams)
25	EG	0.2
60	EG	0.2
70	EG	0.2
80	EG	0.2
25	EG	0.3
25	EG	0.4
25	DI-water	0.2

4.2.3 Materials characterization

X-ray diffraction (XRD) analyses were performed for phase identification of products. A Rigaku D/Max-2000 PC diffractometer was employed, using Cu-Kα radiation (λ=1.54 Å) and x-ray source operating voltage of 40 kV in the 2θ range of 5-92° at a rate of 2°/min. The XRD data were also employed in estimating the average crystallite size of ZnO based on Scherrer's approximation. (102) diffraction peak (47.46 °, 2θ) parameters were used in predicting the representative crystallite size of ZnO nanoparticles.

The morphology and size of the ZnO particles were examined using a FEI Quanta 400F model field emission scanning electron microscope (SEM). The energy dispersive x-ray (EDX) and elemental mapping analysis were also performed. Representative SEM samples were obtained using a suspension of ZnO particles dispersed in DI-water by ultrasonic treatment. A few drops of dilute dispersion were deposited onto a carbon film taped on aluminum grid and then dried in air. Samples were examined without any conductive coating. The average particle size measurements from SEM images were performed by the cross sectional examination of at least 25 particles and errors were estimated by root mean square (RMS) method.

The morphology of ZnO particles was further examined with JEOL 2100 F model transmission electron microscope (TEM) TEM samples were prepared by dropping of ultrasonically dispersed ZnO particle suspension in DI-water on hallow carbon grid. Grids were dried in open air at 25 °C.

The optical properties of the particles were investigated by UV-vis absorption double beam spectrophotometer (Varian-Cary100 Bio) in the wavelength range of 300-800 nm at room temperature. Samples were dispersed in water by 10 min ultrasonic treatment for complete dispersion of the powders.

Room temperature photo luminescence (PL) measurements were conducted with the He-Cd laser (325 nm) and Hamamatsu CCD camera with a range of 300 to 800 nm to investigate the optical properties of particles.

Fourier Transformed Infrared spectroscopy (FTIR) analyses were performed by using IFS 66/S model infrared spectroscopy with Hyperion 1000 microscope. FTIR spectra of powders was obtained in the transmission mode.

4.3 Results

The effects of different reaction temperatures (e.g. 25, 60, 70 and 80 °C) on size and morphology of ZnO nanoparticles were investigated. Optimum reaction temperature was determined to obtain ZnO nanoparticles with distinct shape in nano meter scale. After determination of temperature, the other parameters were developed accordingly these results.

Figure 4.2 illustrates the XRD diffractograms of the reaction products obtained at different precipitation temperatures - 25, 60, 70 and 80 °C - in the aqueous formulations containing identical amount of PVP (0.2 g) as chelating agent. The solvent was EG in all cases and the solid products were collected after 30 min precipitation (reflux) period. The XRD diffractograms revealed that all of the reaction products were phase pure crystalline ZnO (hexagonal wurtzite structure, with JCPDS card no: 36-1451) and no other crystalline phase was detected. The yield of standard protocol (at 25°C - 0.2 g PVP- EG solvent), i.e. ZnO product formation per of zinc acetate dihydrate precursor, was determined at around 95% on molar bases. This shows that proposed precipitation mechanism is very effective to synthesize phase pure ZnO nanoparticles at 25 °C.

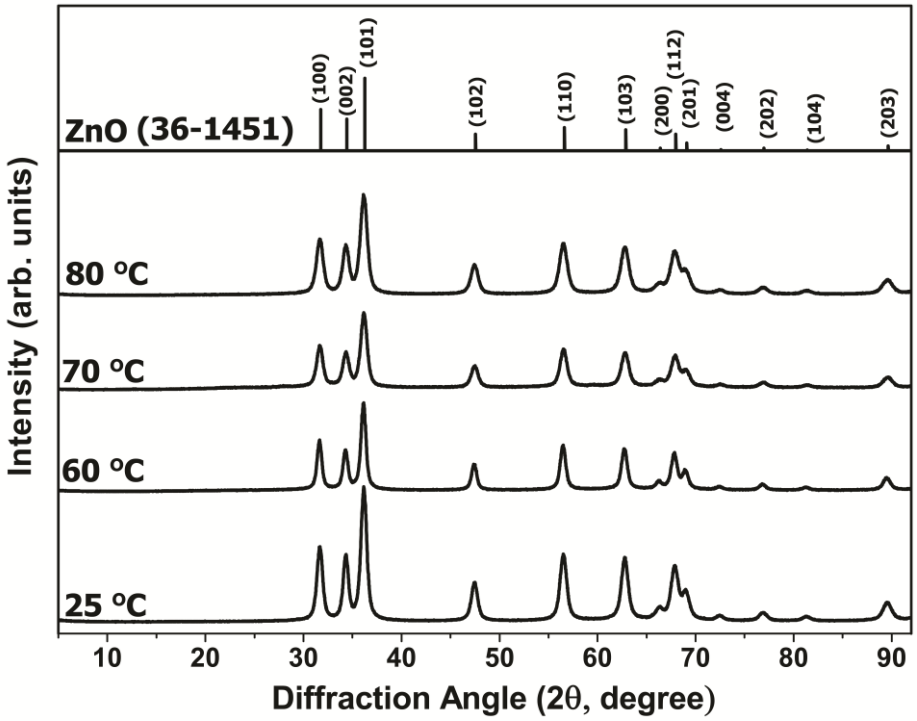

Figure 4.2. XRD patterns of precipitation products synthesized in 0.2 g PVP containing EG-based solutions at 25, 60, 70 and 80 °C.

Figure 4.3 shows low (x200K) and high (x1000K) magnification SEM micrographs of the same ZnO particles synthesized in EG-based solutions at different precipitation temperatures. SEM images indicate that the ZnO nanoparticles had spherical morphology, independent of the reaction temperature.

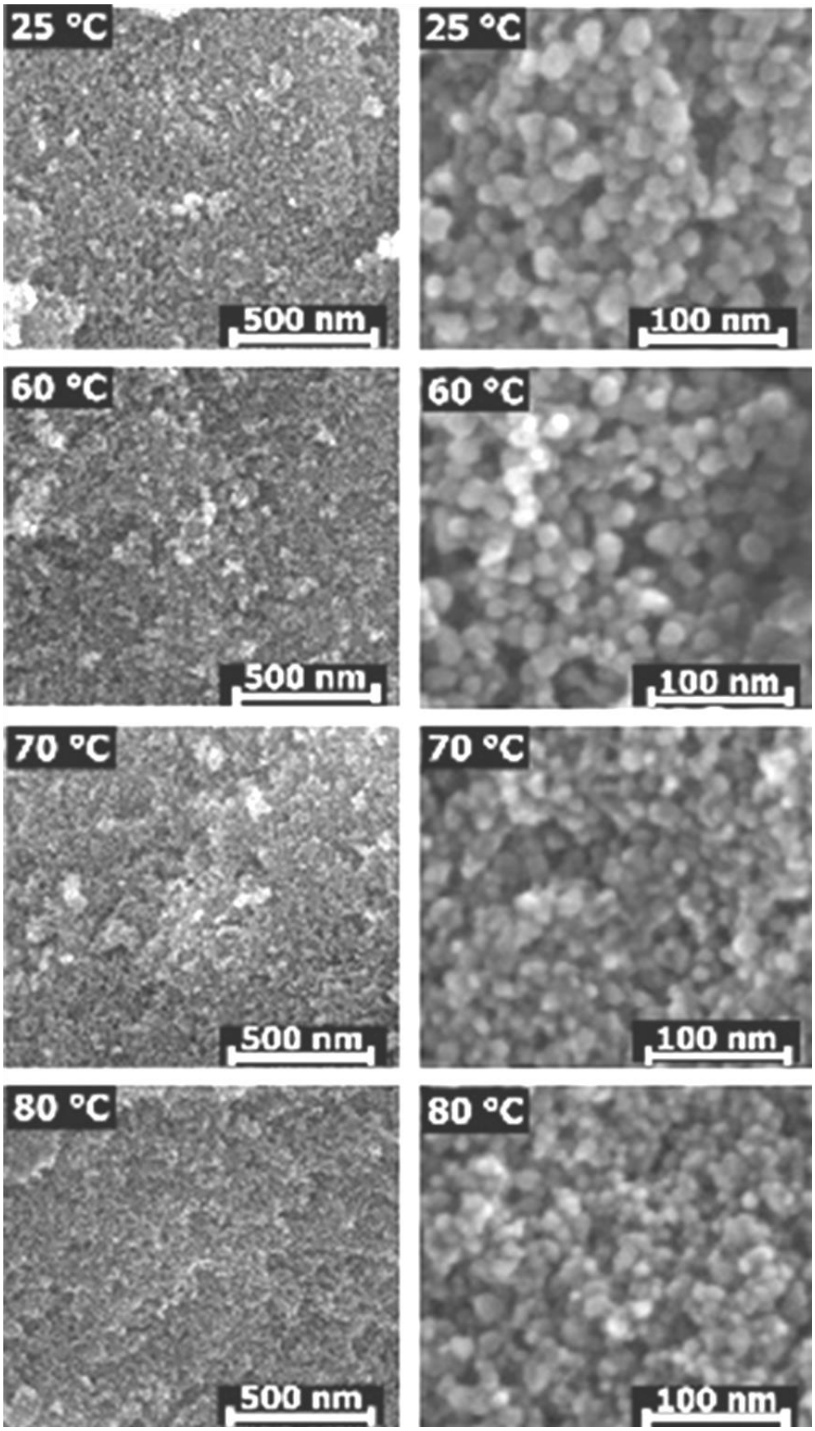

Figure 4.3. Low (left side) and high (right side) magnification SEM micrographs of ZnO nanoparticles prepared in 0.2 g PVP containing EG-based solutions at 25, 60, 70 and 80 °C.

The rough chemical composition of ZnO powders synthesized at 25 ºC was determined with the EDX analysis accompanied with elemental mapping. The EDX spectrum and mapping images of particles are presented in Figure 4.4. The EDX spectrum and mapping images of particles synthesized at 60, 70 and 80 °C give also similar results with particles prepared at 25 °C. Therefore, these results are not given in here. EDX data revealed that the particles are mainly composed of Zn and O elements with an atomic Zn:O proportion of 49.8:50.2, close to stoichiometric ratio of 1:1. Meanwhile, the elemental mapping images also confirmed a homogenous distribution of Zn and O elements suggesting highly pure, stoichiometric ZnO precipitation products.

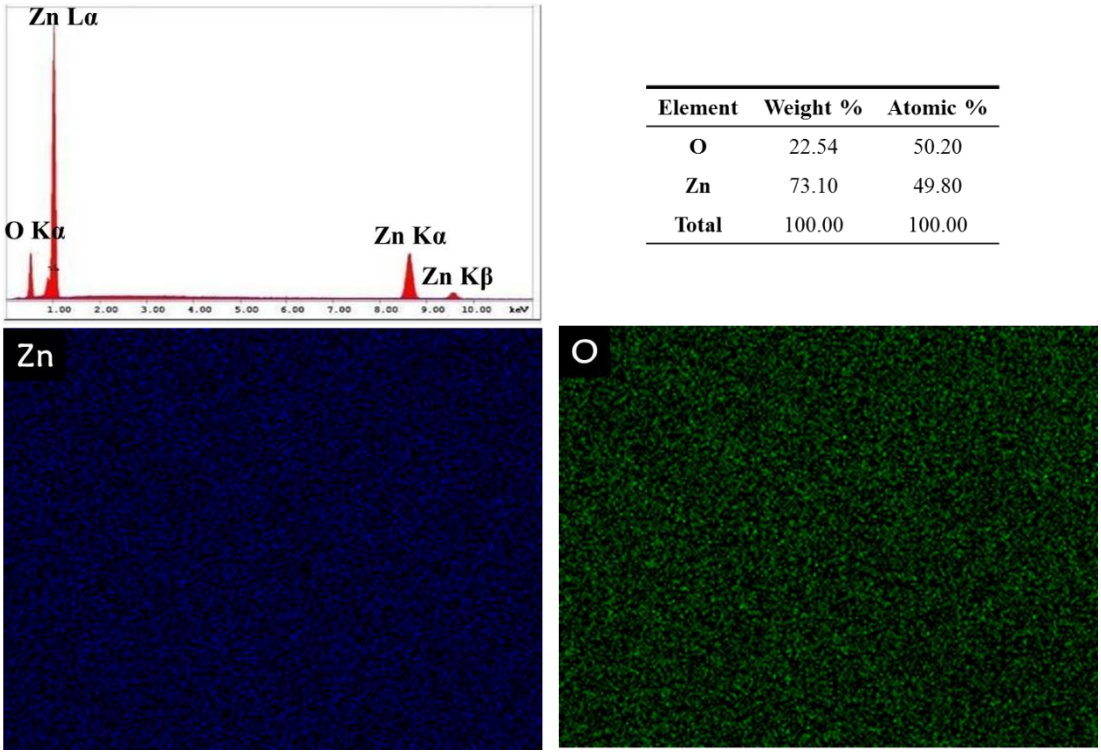

Element	Weight %	Atomic %
O	22.54	50.20
Zn	73.10	49.80
Total	100.00	100.00

Figure 4.4. The EDX spectrum and elemental (Zn and O) mapping images of the ZnO nanoparticles of the precipitation products synthesized at a precipitation temperature of 25 °C.

The morphology and size of the same ZnO nanoparticles were further investigated by TEM. The low and high magnification TEM images of ZnO products synthesized in EG based solutions at 25, 60, 70 and 80 ºC are shown in Figure 4.5. TEM data also

point out that, keeping all other reaction/process parameters identical, spherical ZnO nanoparticles with smaller size were obtained when precipitation temperature was increased. The average particle sizes from TEM results were estimated as 13.0 ± 1.9 nm, 12.2 ± 1.5 nm, 11.8 ± 1.8 nm and 9.0 ± 1.3 nm for the ZnO particles obtained by reactions at 25, 60, 70 and 80 °C, respectively. In parallel to the SEM findings, the TEM images again confirmed an equiaxed/spherical morphology with uniform size distribution for all precipitation products. The high magnification TEM micrographs of selected ZnO nanoparticle(s) exhibiting the fringes of individual planes suggest that ZnO nanoparticles are single crystal, as also clearly indicated by the bottom image in Figure 4.5. This figure shows the HRTEM image of ZnO nanoparticles prepared at 25 °C in the presence EG as solvent and 0.2 g PVP, i.e. according to the standard protocol. The upper and lower insets indicate FFT pattern and IFFT pattern showing the lattice spacings, respectively. The diffused FFT pattern suggest that ZnO particles are single crystal. The lattice spacing between two adjacent planes was determined as ~1.9 Å confirming the wurtzite hexagonal structure of ZnO.

Synthesis of size and shape controlled ZnO nanoparticles can be achieved at relatively low temperature and low refluxing time in the presence of different additives by changing precipitation temperature, PVP amount and solvent. One obvious effect of precipitation temperature is on the average particle size. ZnO powders have spherical morphology at all precipitation temperatures and particle size decreases with increasing precipitation temperature. Table 4.3 summarizes that the average crystallite size of particles calculated from XRD results and the average particle size determined from SEM and TEM micrographs of powders synthesized with different temperatures. All results are very good agreement with each other and the average size of the particles differs from 11.7 ± 0.3 nm to 6.3 ± 0.3 nm and decreases with increasing precipitation temperature from 25 to 80 °C.

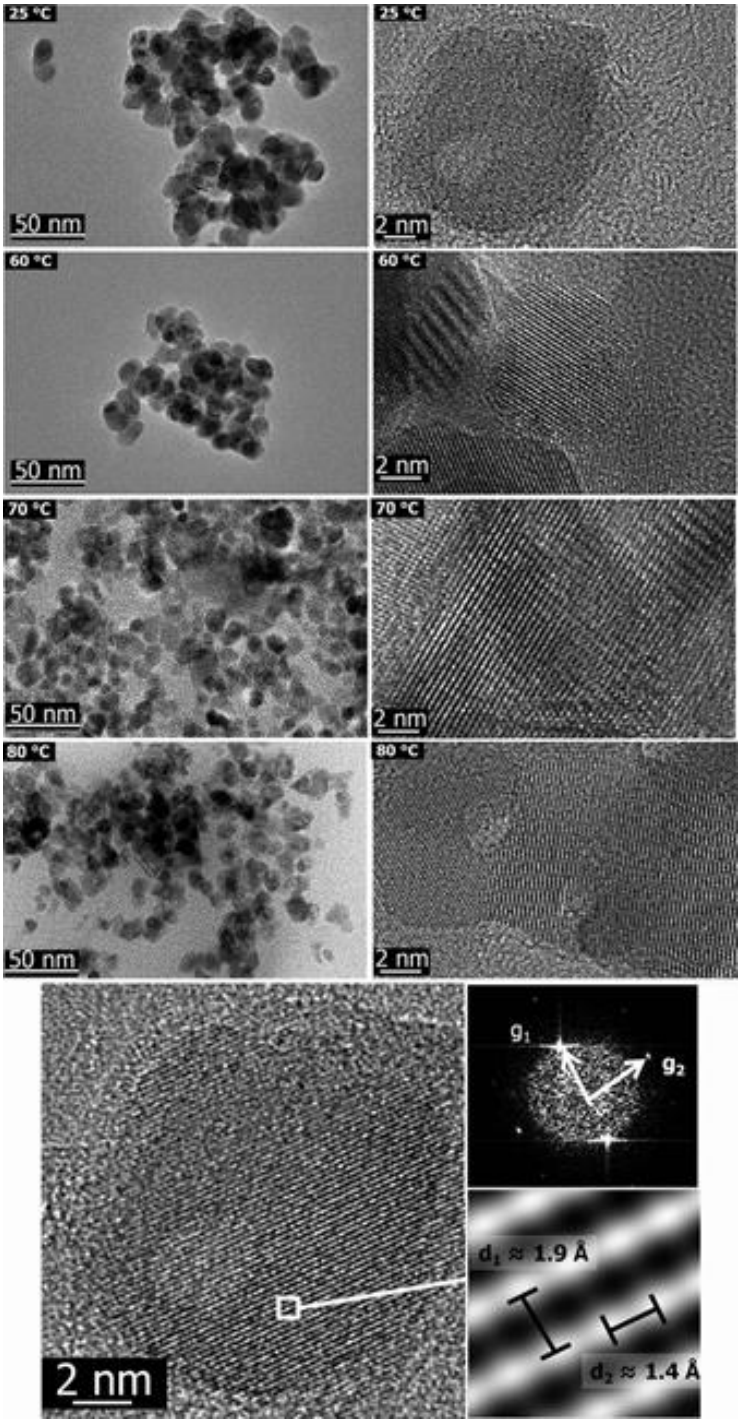

Figure 4.5. TEM (left side) and high resolution TEM (right side) micrographs of ZnO nanoparticles obtained in 0.2 g PVP containing EG-based solutions at 25, 60, 70 and 80 °C. The bottom centered image is for ZnO prepared in 0.2 g PVP containing EG-based solutions at 25 °C. The upper and lower insets indicate FFT pattern and IFFT pattern showing the lattice spacings, respectively.

Table 4.3. Average crystallite sizes estimated from the XRD results and an average particle sizes as determined from SEM and TEM examinations of precipitation products.

Temperature (°C)	Solvent	PVP (g)	XRD crystallite size, nm	SEM particle size, nm	TEM particle size, nm
25	EG	0.2	12.7	d: 11.7±0.3	d: 13.0±1.9
60	EG	0.2	10.8	d: 10.6±0.1	d: 12.2±1.5
70	EG	0.2	10.1	d: 7.7±0.3	d: 11.8±1.8
80	EG	0.2	9.2	d: 6.3±0.3	d: 9.0±1.3

d, diameter

The effects of polymer concentration on morphology and size of ZnO nanostructures were examined in the presence of different amount of PVP (0.2, 0.3 and 0.4 g PVP) at 25 °C precipitation temperature. EG was used as solvent. The XRD diffractograms of precipitation products synthesized in EG-based solutions at 25 °C after 30 min in the presence of different amounts of PVP (0.2, 0.3 and 0.4 g) are shown in Figure 4.6. In all cases, the diffraction pattern again matches with that of crystalline ZnO (hexagonal wurtzite structure, with JCPDS card no: 36-1451) and no additional peaks associated with any other phase/impurity were observed. Meanwhile, the TEM micrographs of ZnO nanoparticles of the same set (with varying PVP amount) are shown in Figure 4.7. The characteristic spherical morphology did not change with increasing PVP amount, but particle size decreased. The average particle size of the highest amount of PVP-containing (0.4 g) precipitation formulation was 5.3 ± 0.3 nm; almost half of the average size of the ZnO particles obtained with minimum PVP-containing formulation (0.2 g), which was determined as 13.0 ± 1.9 nm.

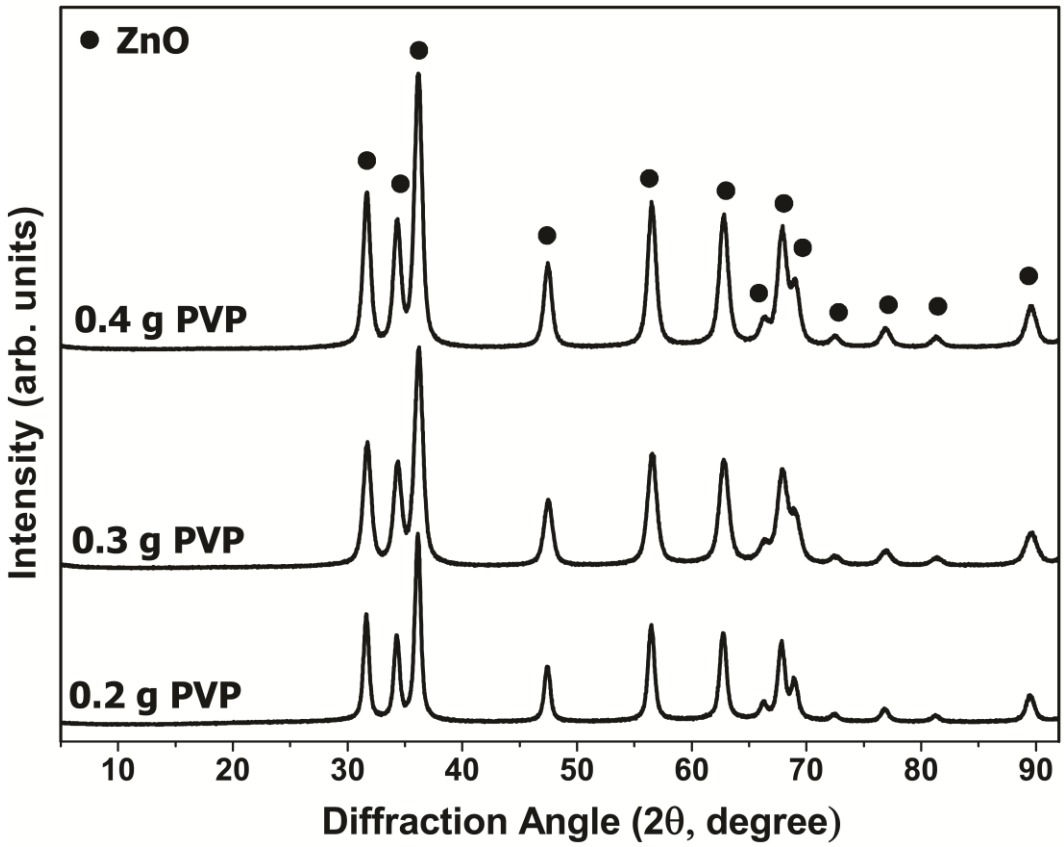

Figure 4.6. XRD patterns of precipitation products prepared by using 0.2, 0.3 and 0.4 g PVP containing EG-based solutions at 25 °C.

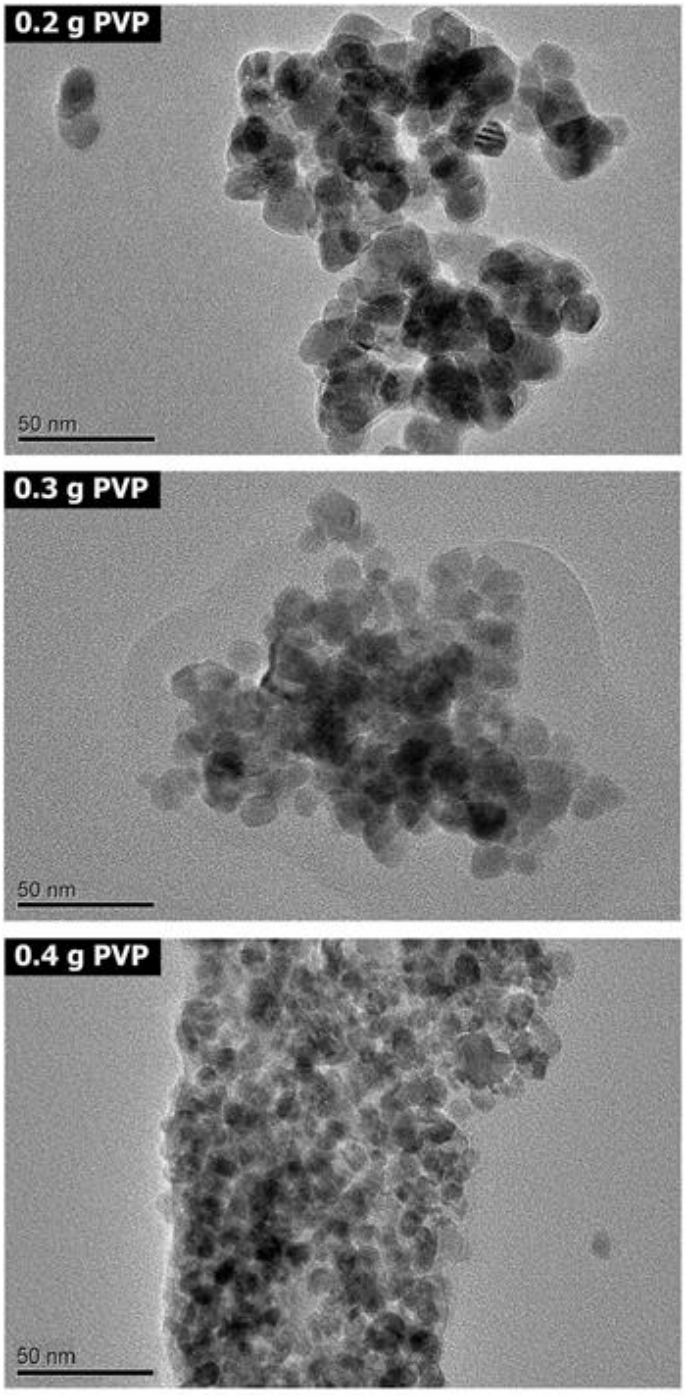

Figure 4.7. TEM images of ZnO nanoparticles synthesized by using 0.2, 0.3 and 0.4 g PVP containing EG-based solutions at 25 °C.

Table 4.4 summarizes that the average crystallite size of particles calculated from XRD results and the average particle size determined from TEM micrographs of powders synthesized in the presence of different amount of PVP.

Table 4.4. Average crystallite size estimated from the XRD results and average particle size as determined from SEM and TEM examinations of precipitation products.

Temperature (°C)	Solvent	PVP (g)	XRD crystallite size, (nm)	TEM particle size, (nm)
25	EG	0.2	12.7	d: 13.0 ± 1.9
25	EG	0.3	10.3	d: 8.0 ± 0.3
25	EG	0.4	9.6	d: 5.3± 0.3

d, diameter.

The effects of solvent type on morphology and size of ZnO nanostructures were examined by using EG, DI-water as solvent in the presence of 0.2 g PVP at 25 °C precipitation temperature. Figure 4.8 shows the XRD diffractograms of ZnO precipitation products prepared at 25 °C in the presence of 0.2 g PVP in two different solvents; EG and DI-water. For direct comparison purposes, the JCPDS card of crystalline ZnO is also presented as an inset in Figure 6 to guide the presentation of the relative intensities of the diffractions. When DI-water was utilized instead of EG, again phase pure ZnO precipitates were obtained as the only crystalline product. The distinction between XRD patterns of ZnO particles synthesized using EG or DI-water as solvent was the differences in relative intensities of the certain diffractions. When water was used as solvent, there is an increase in the relative intensity of (0002) and (1011) diffractions. The reason for this difference will be explained in the discussion part. A comparison of the normalized intensities for all diffraction peaks in Figure 4.8 is also shown in Table 4.5. This data show that, when water was used instead of EG, the intensity ratio of (0002) and $(10\bar{1}1)$ diffractions changes.

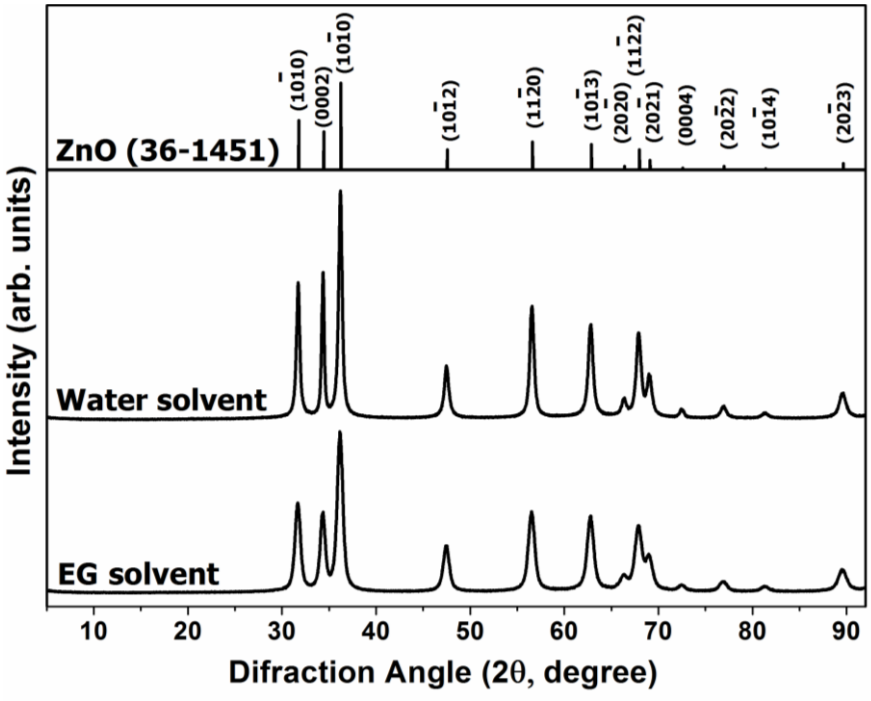

Figure 4.8. XRD patterns of standard ZnO (with JCPDS Card No. 36-1451) and precipitation products prepared by using 0.2 g PVP containing EG-based and DI-water-based solutions at 25 °C.

The differences in chemical composition of ZnO precipitates synthesized using different solvents were also investigated with FTIR spectroscopy and the spectra of the ZnO particles obtained in EG-based and DI-water-based precipitation formulations are shown in Figure 4.9. The FTIR spectrum of PVP is also shown in Figure 4.9. For PVP, the bands located at 3440, 2950, 1650, 1420 and 1288 cm^{-1} were assigned to the O-H stretching vibration, CH_2 unsymmetrical stretching vibration, C═O stretching vibration, CH_2 bending vibration and C-N stretching vibration bands, respectively [21]. ZnO spectra reveal four adsorption bands located at 1573, 1420, 880 and 400 cm^{-1} assigned for C═N stretching vibration, CH_2 bending vibration, NO and ZnO stretching mode, respectively [22-25]. FTIR spectrum of the ZnO precipitates prepared in DI-water showed two additional bands located at 1660 and 1288 cm^{-1}. The reason for presence of these peaks will be also clarified in discussion. In summary, FTIR spectra shows that the precipitation products are ZnO contained small amount of organic residues attributed to the starting precursor materials.

Table 4.5. Relative normalized intensities of the diffractions for standard ZnO (JCPDS card no: 36-1451) and ZnO powders synthesized at 25 °C in EG and DI-water based solvent.

Diffraction plane	Standard ZnO (JCPDS Card No, 36-1451)	ZnO synthesized at 25 °C in EG	ZnO synthesized at 25 °C in DI-water
$(10\bar{1}0)$	57	56	60
(0002)	44	50	64
$(10\bar{1}1)$	100	100	100
$(10\bar{1}2)$	23	29	24
$(11\bar{2}0)$	32	50	50
$(10\bar{1}3)$	29	48	42
$(20\bar{2}0)$	4	11	10
$(11\bar{2}2)$	23	42	38
$(20\bar{2}1)$	11	24	20
(0004)	2	5	5
$(20\bar{2}2)$	4	7	6
$(10\bar{1}4)$	1	4	3
$(20\bar{2}3)$	7	15	12

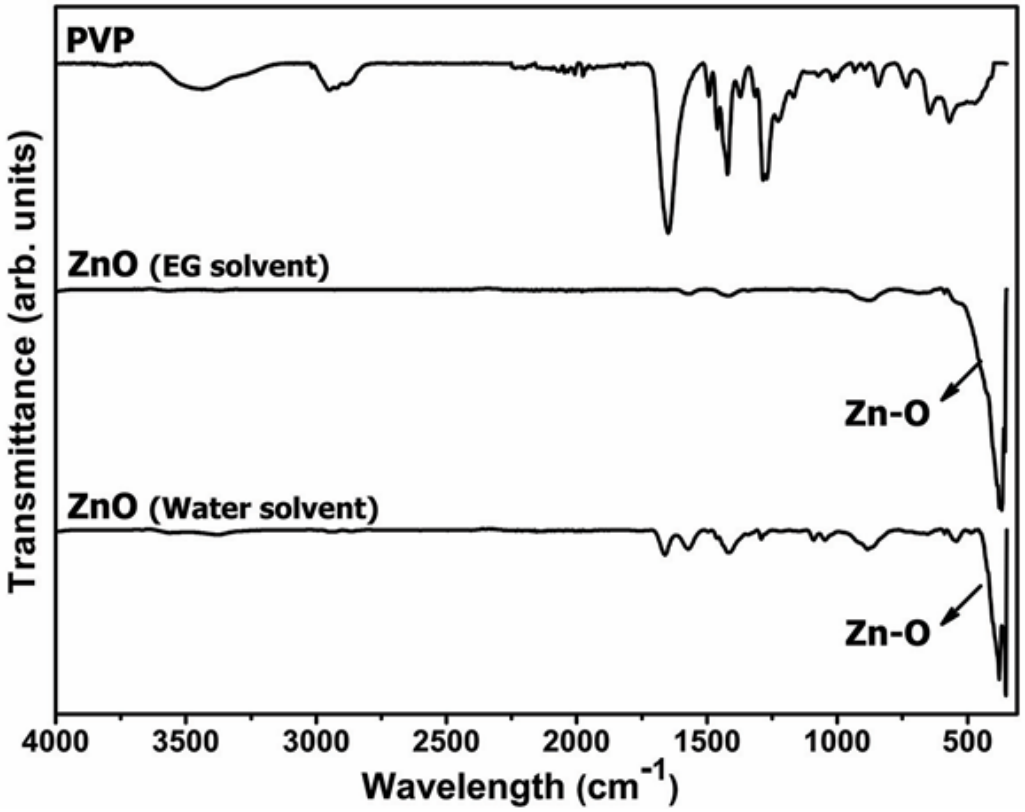

Figure 4.9. FTIR spectra of pure PVP and ZnO nanoparticles synthesized in 0.2 PVP-containing EG-based and DI-water-based solutions at 25 °C.

SEM and TEM micrographs of ZnO nanoparticles prepared by using DI-water as solvent at 25 °C precipitation temperature are shown in Figure 4.10. Changing the solvent from EG to DI-water resulted in morphology change from spherical to isosceles triangle. The average side lengths of triangles were determined as 175 ± 20 nm from the micrograph.

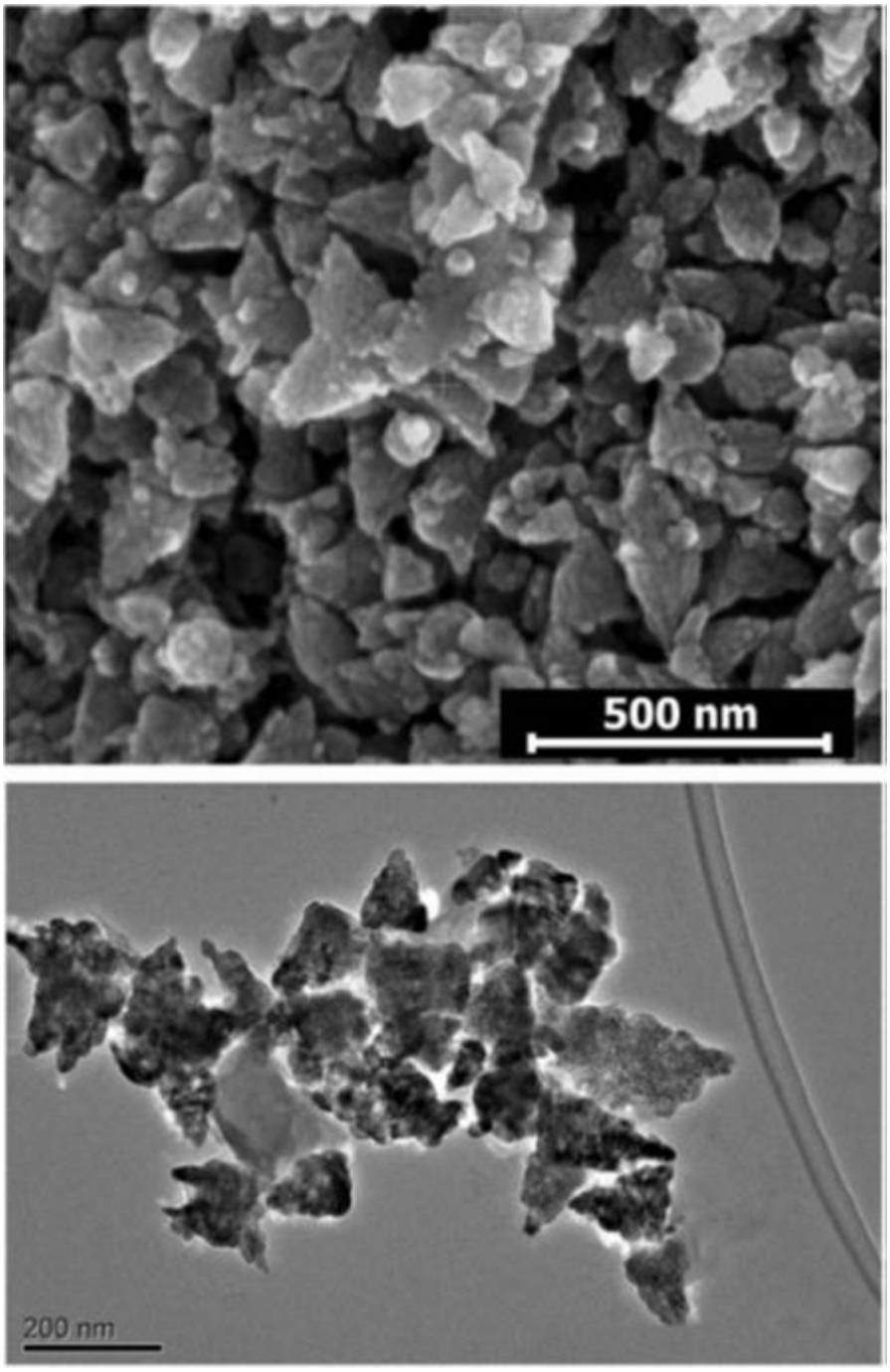

Figure 4.10. SEM (top) and TEM (bottom) micrographs of agglomerated ZnO nanoparticles prepared by using 0.2 g PVP-containing DI-water based solution at 25 °C.

The optical properties of ZnO precipitates obtained from EG and DI-water solvent formulations (at 25 °C) are presented with the absorption and room temperature PL spectra shown in Figure 4.11 (a) and Figure 4.11 (b), respectively. The absorption spectra had distinct absorption bands at ~353 nm and ~358 nm for EG and DI-water formulations, respectively. The direct band gap energy (Eg) of ZnO were determined by fitting the absorption data and given as insets in UV absorption graphs. Figure 4.11(b) shows that both powders prepared in different solvents exhibit weak UV emission (~380 nm) and strong orange emission (~640 nm) bands [25-26]. The intensities of both characteristic emissions for ZnO powders synthesized in EG were lower than that of ZnO powders prepared in DI-water.

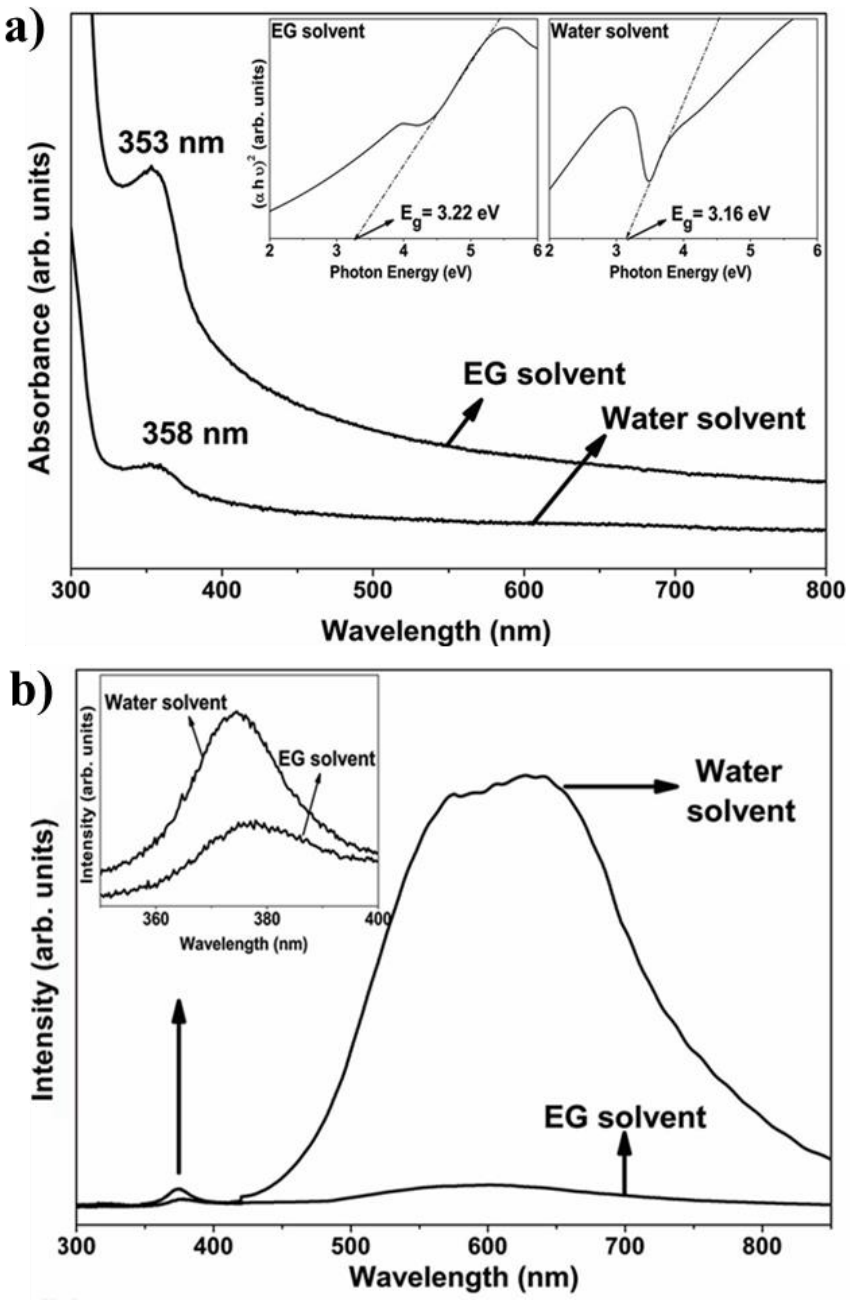

Figure 4.11. (a) UV-Vis adsorption spectra and **(b)** room temperature PL spectra of ZnO nanoparticles prepared by using 0.2 g PVP containing EG-based and DI-water-based solutions at 25 °C (precipitation temperature). The insets in (a) show plots of $(\alpha hv)^2$ as a function of photon energy (E_g) for both precipitation products. The inset in (b) discloses the indicated segment from the underlying PL spectra, magnified to show the band gap emission.

4.4 Discussion

Highly crystalline ZnO nanoparticles can be synthesized with proposed precipitation system at around room temperature and short precipitation periods. The results show that the size and morphology modification of ZnO particles can be accomplished by controlling various processing parameters, including precipitation temperature, amount of chelating agent and solvent type.

4.4.1 The effect of reaction temperature on size and morphology of ZnO particles

Synthesis of spherical ZnO nanoparticles was achieved when EG was used as solvent in the presence of PVP as chelating agent. The particle size was greatly affected by the precipitation temperature (Figure 4.3 and Figure 4.5). During precipitation of solid particles in ionic parent solutions, relative surface activity of various growth facets is one of the most important size and morphology determining factors for the resultant crystalline product. ZnO crystal has a polar structure and consists of catalytically active Zn-terminated polar top surface (0001), catalytically inert O-terminated polar bottom surface $(000\bar{1})$ and non-polar surfaces $\{01\bar{1}0\}$ and $\{2\bar{1}\bar{1}0\}$ [27- 28]. Organic additives in the parent solution, EG and/or PVP, can selectively interact with these sites of energetically different states and restrain growth of the certain crystallographic planes of such crystal system mainly by chemical and/or physical adsorption. The former can preferentially occur between organic molecules and positive polar planes of ZnO crystals; however the latter takes place between organic additives and non-polar planes of ZnO crystals. As a result of adsorption events and selective passivation of certain planes by the organic molecules, relative growth rate of the precipitating particles changes in these crystallographic directions [29, 30].

EG is an organic solvent consisting of polar OH molecules and affects the growth of ZnO crystal due to its excellent chemical adsorption ability by means of complexes developing between anionic groups of EG and positive polar top surface of ZnO crystals [31]. Similarly, growth orientation of ZnO is also affected by PVP which can hamper growth of certain planes of ZnO both by chemical and physical adsorption. In

the polar media, possible coordination between PVP and ZnO crystal is chemical adsorption which occurs between negative charged oxygen atom of PVP and positive polar top surface of ZnO ZnO crystals [21]. However, such chemical association between EG and ZnO crystals already exist in the current precipitation system. Therefore, PVP molecules physically adsorb on non-polar surfaces of ZnO crystal. Both chemical adsorption of EG and physical adsorption of PVP inhibit growth of ZnO at preferential growth direction and lead to formation of spherical ZnO nanostructures in equiaxed form. The reaction temperature in relation with these selective adsorption events affects the size of the ZnO particles. Figure 4.12 schematically represents the relationship between particle size and reaction temperature according the suggested precipitation model. Upper side of the figure shows representation of the initial size of ZnO for all precipitation temperatures. Meanwhile, lower side indicates representations of final size of ZnO after synthesis at different precipitation temperature. At higher reaction temperature, both the number of nucleation sites for ZnO crystals and the number of adsorbed molecules of EG and PVP on the growth plane of ZnO crystals increase impeding growth of the spherical ZnO nanoparticles. This leads to formation of relatively smaller yet still uniform particle size of ZnO precipitates at the high reaction temperature (80 °C). Table 4.3 summarizes the average crystallite size of particles determined from XRD results (by peak broadening analyses) and the average particle size obtained from SEM and TEM examinations of ZnO particles synthesized as different reaction temperatures. All analytical results on particle sizes are in good agreement and the average size of the ZnO particles can be effectively controlled in the range of 9-13 nm by the choice of precipitation temperature in the range of 25-80 °C. Decreasing particle size with increasing precipitation temperature is due to an increase in adsorption events between organic molecules and ZnO crystal which inhibit growth of ZnO crystal.

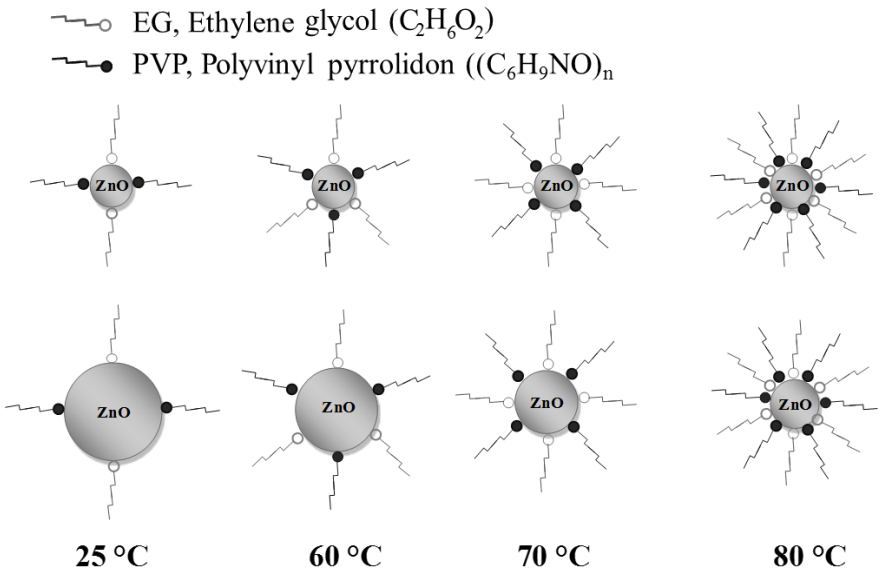

Figure 4.12. A schematic representation of temperature effect on size of spherical ZnO nanoparticles by means of the attaching of EG and PVP on some specific growth plane of crystals.

4.4.2 The effect of chelating agent (PVP) amount on size and morphology of ZnO particles

It has been found that the average particle size of ZnO nanoparticles also decreases with increasing amount of PVP at precipitation temperature of 25 °C (Figure 4.7 and Table 4.5). This is due to two factors. i. PVP promotes nucleation of ZnO by accelerating the dehydration reaction of ZnO precursor and forming coordinating complex [32], ii. Both physical and chemical adsorption of PVP molecules on ZnO crystal are promoted in precipitation solutions containing higher PVP amount [32]. It has been reported that a critical amount of PVP is required to produce a significant change in ZnO precipitation mechanism [33]. At very low concentration, PVP is not effective to promote ZnO nucleation, while increasing the PVP amount provides nucleation and crystallization of ZnO by means of chemical adsorption. However, further increase the PVP amount promotes not only chemical but also physical adsorption and provides formation of smaller ZnO particles. In the precipitation system containing high amount of PVP and EG as solvent, both chemical adsorption of EG

and PVP, and physical adsorption with PVP occur simultaneously. As a result, particle growth is also distinctly inhibited and smaller sized spherical ZnO nanoparticles develop. Figure 4.13 indicates a schematic representation of the PVP concentration on size of spherical ZnO nanoparticles. As summarized in Table 4.4, with an increase in the amount of PVP from 0.2 to 0.4 g in the parent solution, the average size of the particles decreased from 13.0 ± 1.9 nm to 5.3 ± 0.3 nm according to TEM examinations. Reduction in particle size with increasing PVP amount is also due to an increase in the size of adsorption events between organic molecules and ZnO surface.

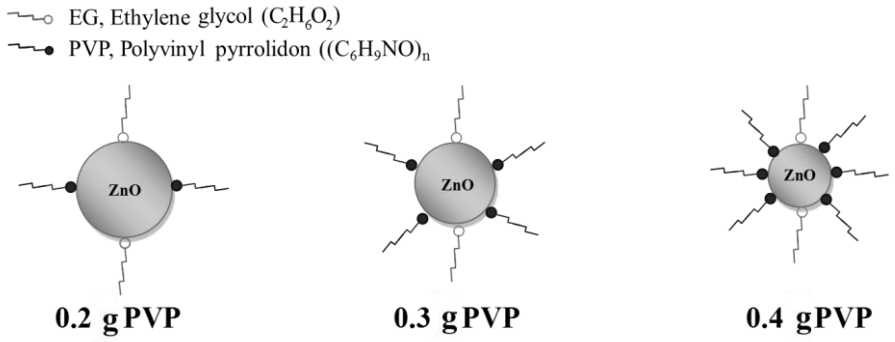

Figure 4.13. A schematic representation of the effect of PVP concentration on size of spherical ZnO nanoparticles prepared at 25 °C.

4.4.3 The effect of solvent type on size and morphology of ZnO particles

The solvent mainly affects the agglomeration tendency of ZnO nanoparticles. In the presence of EG, polar planes (0001) and nonpolar $\{01\bar{1}0\}$ planes of ZnO nuclei are associated with EG and PVP, respectively. This preferential coordination is due to distinctly highly polarized nature of EG as compared with PVP. These interactions reduce the surface free energy of these particular planes and depress any directional growth of ZnO nuclei. This eventually leads to equiaxed/spherical particle morphology (Figure 4.3 and Figure 4.5). However, using water instead of EG resulted in triangular shaped ZnO agglomerates (Figure 4.10). This can be explained by different stabilization ability of the solvent on specific crystallographic planes of the growing crystal [34]. When water was used, polar PVP molecules weakly link nonpolar $\{01\bar{1}0\}$

planes of ZnO nuclei, as well with the polar (0001) planes that readily available in the absence EG. However, considering presence of same amount of PVP both in EG- and water-based precipitation systems, the additional molecular coordination of PVP with polar (0001) planes results in less effective association with nonpolar lateral planes of larger area; in other words, in water-containing system the nonpolar planes were less effectively covered by PVP. As a result of limited reduction of the surface free energy of the lateral planes, ZnO crystals tend to form multi nuclei aggregates in triangular form.

In addition, the XRD data (Figure 4.8) suggests a possible morphological variation for the primary ZnO particles within agglomerates obtained in water. The diffraction peak intensities of the ZnO products prepared from EG-based precipitation solution at 25 °C show a complete match with the standard card in terms of intensity order for the diffraction events. This is a sign for formation of the energetically most favorable form, spherical morphology, of ZnO nanoparticles. On the other hand, the XRD pattern of ZnO particles synthesized at 25 °C in DI-water show a distinct deviation from the standard intensity order for the (0002) and $(10\bar{1}1)$ diffractions. The reason for such differences is the anisotropic growth of ZnO nanostructures during precipitation reaction. The preferential growth orientation of ZnO is [0002] direction in terms of energy considerations. Therefore, particles should tend to grow along [0002] direction and relative intensity of (0002) peak increases in the absence of any additives that can prevent to grow particles through this direction. Yao et al. [35] reported that higher relative intensity of $(10\bar{1}1)$ diffraction increases due to the preferential orientation along this direction by the formation of many $\{10\bar{1}1\}$ sides, which causes the formation of triangular ZnO nanoparticles. According to XRD pattern of ZnO structures synthesized in the DI-water based precipitation system, relatively higher intensities of these peaks [(0002) and $(10\bar{1}1)$] point out growth of recently formed ZnO nanostructures into agglomerated triangular ZnO structures.

FTIR investigation also provides some insights about the physical and chemical events between ZnO precipitates in their respective parent solutions (Figure 4.8). The ZnO particles prepared in EG shows the main absorption bands of ZnO stretching mode

located at around 400 cm^{-1}. This spectrum also exhibits bands around 1573, 1420 and 880 cm^{-1} associated with C═N stretching vibration and CH_2 bending vibration of PVP and NO stretching mode but not contains bands around 1650 and 1288 cm^{-1} associated with C═O and C–N stretching vibration bands of PVP, respectively [22, 36]. The presence of peaks related with PVP indicates that there should be an interaction between PVP and resultant ZnO particles. However, weak intensities of bands located at 1573 and 1420 cm^{-1} indicate that chemical adsorption between PVP and ZnO is recessive and the existence of relatively higher intensities of band at 880 cm^{-1} shows physical adsorption between nitrogen atoms of PVP and oxygen atoms of ZnO. Therefore, main adsorption between PVP and ZnO crystal in EG should be physical adsorption and particle morphology mostly depends on chemical adsorption with EG and physical adsorption with PVP. FTIR spectra of particles prepared in DI-water on the other hand exhibits two additional bands at 1660 and 1288 cm^{-1} which indicate that dominant resonant structure of PVP is >N-Ċ═O [21]. Presence of these bands shows that both chemical and physical adsorption between PVP and ZnO may occur. However, the shift of C═O stretching vibration band of PVP from 1650 to 1660 cm^{-1} indicates that chemical adsorption between PVP and ZnO is dominant [36]. Due to absence of interaction between water and ZnO, inhibition of growth of ZnO crystal along preferential growth direction depresses and particle morphology only depends on adsorption of PVP. Therefore, particle growth occurs on certain directions and triangular ZnO forms.

Optical properties of ZnO nanoparticles simultaneously depend on two main characteristics of particles; size and defect structure. Independent of the solvent type, the absorption spectra for both ZnO particles exhibit the main absorption band related with wurtzite type of ZnO (Figure 4.11(a)) [39]. However, the positions of bands are slightly different, at ~353 nm for EG and ~358 nm for DI-water, both showing a blue shift compared to values that of bulk ZnO (~373 nm) [40]. Moreover, the absorption band wavelength of particles prepared in EG illustrates a more distinct blue shift with respect to particles prepared in the DI-water. This difference is due to smaller size of particles synthesized in EG. This is also reflected by the band gap values. Upon a decrease in particle size resulting in a positional shift in the adsorption wavelengths to

the relatively lower values, band gap value increases [41]. The band gap of ZnO prepared in EG (Eg=3.22 eV) with relatively smaller size is higher than that of in water (Eg=3.16 eV). The presence of defects in ZnO nanostructure is another important factor determined to optical properties of particles because they will diminish band gap and deteriorate optical properties of ZnO nanoparticles. According to literature, ZnO powders mainly exhibit three emission bands: UV emission (~380 nm) which is attributed to the direct recombination of excitons [42], green emission (~530 nm) associated with oxygen vacancies [43] and orange emission (~640 nm) which is attributed to oxygen interstitials [44]. According to results of the current study, although both samples prepared with different solvents exhibit UV and orange emissions, particles prepared in DI-water show very high intensity of orange emission (Figure 4.11(b)). This is due to the high number of oxygen interstitials and may be attributed to high extent of chemical coordination between oxygen atoms of PVP and polar surfaces of ZnO crystals.

4.5 Conclusions

Low temperature synthesis of size and morphology controlled highly crystalline ZnO nanoparticles were performed via precipitation method. The size of spherical ZnO nanoparticles decreased with increasing precipitation temperature as a result of increase in the number of nuclei formation and enhancement chemical and physical adsorption between ZnO crystals and organic molecules. Furthermore, when higher amount of chelating agent was used, the size of spherical ZnO particles decreased due to combined chemical adsorption of EG and PVP with ZnO crystal, and physical adsorption between PVP and ZnO. Hence, the proposed solution precipitation system is advantageous for obtaining size controlled ZnO nanoparticles with narrow size distribution. Moreover, variation in ZnO morphology from spherical to isosceles triangular is achieved by changing solvent from EG to DI-water due to different adsorption abilities of the solvents. Results of this study indicate that the suggested precipitation method provides a simple approach for tailoring the size and morphology of the ZnO nanoparticles at low precipitation temperatures and short processing periods by an easy wet chemical route.

4.6 References

1. Gupta T.K., Journal of the American Ceramic Society, **1990** 73(7) p. 1817-1840.

2. Singhai M., Chhabra V., Kang P., and Shah D.O., Materials Research Bulletin, **1997** 32(2) p. 239-247.

3. Gao T. and Wang T.H., Applied Physics A: Materials Science & Processing, **2005** 80(7) p. 1451-1454.

4. Liao L., Lu H.B., Li J.C., He H., Wang D.F., Fu D.J., Liu C., and Zhang W.F., The Journal of Physical Chemistry C, **2007** 111(5) p. 1900-1903.

5. Li Y.B., Bando Y., and Golberg D., Applied Physics Letters, **2004** 84(18) p. 3603-3605.

6. Cheng C.-L., Chao S.-H., and Chen Y.-F., Journal of Crystal Growth, **2009** 311(19) p. 4381-4384.

7. Ramamoorthy K., Sanjeeviraja C., Jayachandran M., Sankaranarayanan K., Bhattacharya P., and Kukreja L.M., Journal of Crystal Growth, **2001** 226(2-3) p. 281-286.

8. Choopun S., Tubtimtae A., Santhaveesuk T., Nilphai S., Wongrat E., and Hongsith N., Applied Surface Science, **2009** 256(4) p. 998-1002.

9. Liu B. and Zeng H.C., Journal of the American Chemical Society, **2003** 125(15) p. 4430-4431.

10. Pal U. and Santiago P., Journal of Physical Chemistry B, **2005** 109(32) p. 15317-15321.

11. Ayouchi R., Martin F., Leinen D., and Ramos-Barrado J.R., Journal of Crystal Growth, **2003** 247(3-4) p. 497-504.

12. Htay M.T., Hashimoto Y., Momose N., and Ito K., Journal of Crystal Growth, **2009** 311(20) p. 4499-4504.

13. Ristic M., Music S., Ivanda M., and Popovic S., Journal of Alloys and Compounds, **2005** 397(1-2) p. L1-L4.

14. Li J., Srinivasan S., He G.N., Kang J.Y., Wu S.T., and Ponce F.A., Journal of Crystal Growth, **2008** 310(3) p. 599-603.

15. Ahmad T., Vaidya S., Sarkar N., Ghosh S., and Ganguli A.K., Nanotechnology, **2006** 17(5) p. 1236-1240.

16. Yildirim O.A. and Durucan C., Journal of Alloys and Compounds, **2010** 506(2) p. 944-949.

17. Tao D., Qian W., Huang Y., and Wei F., Journal of Crystal Growth, **2004** 271(3-4) p. 353-357.

18. Wang J.M. and Gao L., Journal of Materials Chemistry, **2003** 13(10) p. 2551-2554.

19. Wang C.L., Shen E.H., Wang E.B., Gao L., Kang Z.K., Tian C.G., Lan Y., and Zhang C., Materials Letters, **2005** 59(23) p. 2867-2871.

20. Xie R.G., Li D.S., Zhang H., Yang D.R., Jiang M.H., Sekiguchi T., Liu B.D., and Bando Y., Journal of Physical Chemistry B, **2006** 110(39) p. 19147-19153.

21. Sui X.M., Liu Y.C., Shao C.L., Liu Y.X., and Xu C.S., Chemical Physics Letters, **2006** 424(4-6) p. 340-344.

22. Gao P.X. and Wang Z.L., Journal of Physical Chemistry B, **2004** 108(23) p. 7534-7537.

23. Silva R.F. and Zaniquelli M.E.D., Colloids and Surfaces a-Physicochemical and Engineering Aspects, **2002** 198 p. 551-558.

24. Wahab R., Kim Y.S., Lee K., and Shin H.S., Journal of Materials Science, **2010** 45(11) p. 2967-2973.

25. Drelinkiewicz A., Hasik M., Quillard S., and Paluszkiewicz C., Journal of Molecular Structure, **1999** 511-512(0) p. 205-215.

26. Studenikin S.A., Golego N., and Cocivera M., Journal of Applied Physics, **1998** 84(4) p. 2287-2294.

27. Yang C.L., Wang J.N., Ge W.K., Guo L., Yang S.H., and Shen D.Z., Journal of Applied Physics, **2001** 90(9) p. 4489-4493.

28. Wang Z.L., Journal of Physics-Condensed Matter, **2004** 16(25) p. R829-R858.

29. Zhang L. and Zhu Y.J., Applied Physics a-Materials Science & Processing, **2009** 97(4) p. 847-852.

30. Harunar Rashid M., Raula M., Bhattacharjee R.R., and Mandal T.K., Journal of Colloid and Interface Science, **2009** 339(1) p. 249-258.

31. Ghoshal T., Kar S., and Chaudhuri S., Crystal Growth & Design, **2006** 7(1) p. 136-141.

32. Wei S.F., Lian J.S., and Jiang Q., Applied Surface Science, **2009** 255(15) p. 6978-6984.

33. Zhang J., Liu H., Wang Z., and Ming N., Journal of Crystal Growth, **2008** 310(11) p. 2848-2853.

34. Pacholski C., Kornowski A., and Weller H., Angewandte Chemie International Edition, **2002** 41(7) p. 1188-1191.

35. Yao C.W., Wu H.P., Ge M.Y., Yang L., Zeng Y.W., Wang Y.W., and Jiang J.Z., Materials Letters, **2007** 61(16) p. 3416-3420.

36. Muta H., Ishida K., Tamaki E., and Satoh M., Polymer, **2002** 43(1) p. 103-110.

37. Bai J., Li Y.X., Zhang C.Q., Liang X.F., and Yang Q.B., Colloids and Surfaces a-Physicochemical and Engineering Aspects, **2008** 329(3) p. 165-168.

38. Zhang Z.Y., Shao C.L., Gao F., Li X.H., and Liu Y.C., Journal of Colloid and Interface Science, **2010** 347(2) p. 215-220.

39. Wahab R., Ansari S.G., Kim Y.S., Seo H.K., Kim G.S., Khang G., and Shin H.-S., Materials Research Bulletin, **2007** 42(9) p. 1640-1648.

40. Haase M., Weller H., and Henglein A., The Journal of Physical Chemistry, **1988** 92(2) p. 482-487.

41. Singla M.L., Shafeeq M M., and Kumar M., Journal of Luminescence, **2009** 129(5) p. 434-438.

42. Willander M., Nur O., Sadaf J.R., Qadir M.I., Zaman S., Zainelabdin A., Bano N., and Hussain I., Materials, **2010** 3(4) p. 2643-2667.

43. Kang H.S., Kang J.S., Kim J.W., and Lee S.Y., Journal of Applied Physics, **2004** 95(3) p. 1246-1250.

44. Liu M., Kitai A.H., and Mascher P., Journal of Luminescence, **1992** 54(1) p. 35-42.

CHAPTER 5

ROOM TEMPERATURE SYNTHESIS OF SILVER-DOPED ZINC OXIDE (ZnO:Ag) NANOPARTICLES: STRUCTURAL, OPTICAL AND PHOTOCATALYTIC PROPERTIES

5.1 Introduction

ZnO nanostructures have attracted a great attention for their potential applications in variety fields such as varistors [1], gas sensors [2], field emitters [3] and solar cells [4]. Recently, there is an ever increasing interest in the photocatalytic applications of ZnO. Although TiO_2 and ZnO have been recognized as the two most effective catalysts [5, 6] and widely used in the removal of toxic or hazardous organic pollutants [7], ZnO got more attention due to its stronger luminescent properties, broader ultraviolet light absorption and lower cost than TiO_2. Photocatalytic activity of ZnO nanoparticles can be determined by the ability of electron-hole ($e^-/h^\bullet$) pair formation under illumination. When a ZnO crystal absorbs a photon, which has equal or greater energy than the bandgap of ZnO, an electron (e^-) is promoted from the valence band (VB) to the conduction band (CB) and a hole ($h^\bullet$) forms in the VB. If $e^-/h^\bullet$ charge separations are maintained and they reach the catalyst surface, electrons form highly active superoxide radicals and holes oxidize the organic molecules [8].

However, pure ZnO nanoparticles do not meet the practical needs as a photocatalytic material, as activation of ZnO catalyst necessitate high energy UV light, leading to low efficiency in the visible and near infrared regions. The rapid recombination of the photogenerated $e^-/h^\bullet$ pairs is another limiting factor that impedes the photocatalytic activity of ZnO nanoparticles. In order to solve these problems, considerable efforts have been spent on the improvement of the photocatalytic ability by means of semiconductor combination [9], transition metal doping [10] or noble metal deposition

[11]. Among these techniques, noble metal deposition seems to be the most promising method due to excellent enhancement of the photocatalytic properties of semiconductors. Doping ZnO with various noble metals such as gold, palladium and silver (Ag) could significantly improve their photocatalytic activity [12-14]. Recently, synthesis of silver-doped ZnO (ZnO:Ag) nanoparticles has become an exciting area in research and different photocatalytic mechanisms for ZnO:Ag nanoparticles have been proposed. In the photochemical reactions, Ag can trap the photogenerated electrons from the ZnO and form the holes to create hydroxyl radicals providing the degradation reaction of organic species. In addition, Ag can improve the photocatalytic activity of ZnO nanoparticles by creating a local electric field and enhance electrical properties by the optical vibration of surface plasmon [15]. Surface properties such as oxygen vacancies and crystal defects are also responsible for the enhancement of the photocatalytic activity of particles [11, 16]. Moreover, higher light scattering of Ag also improves the photocatalytic properties of ZnO nanoparticles [17].

A variety of techniques have been exploited to synthesize ZnO:Ag nanostructures like electrochemical [18], photochemical [19], sol–gel [20], hydrothermal [21], microwave [22] and flame spray pyrolysis [23]. In spite of the successful synthesis and good photocatalytic properties of ZnO:Ag nanostructures, the above listed methods require high synthesis temperature or harsh synthesis conditions like rigorous experimental conditions/sophisticated equipments. Therefore, low temperature synthesis with simple synthesis procedure is desirable for the large-scale production. Solution approaches are appealing as more suitable. However, room temperature synthesis without any subsequent heat treatment has still remained as a challenge because, to the best of our knowledge, there are no exhaustive studies on the room temperature synthesis of ZnO:Ag nanoparticles. Here, ZnO:Ag nanostructures have been successfully synthesized at room temperature with simple precipitation technique and detailed structural/optical analyses were done with Rietveld refinement, microscopic/stereoscopic techniques. Furthermore, effect of Ag content on photocatalytic characteristics of ZnO nanoparticles was investigated.

5.2 Experimental methods

5.2.1 Materials

The chemicals used during synthesis of Ag doped ZnO nanoparticles are listed in Table 5.1. All reagents were used without further purification. Ultrapure deionized (DI) water used during reactions was obtained by using Human Corporation Zeneer Power I water purification system.

Table 5.1. Materials used in the experimental part of the synthesis of Ag doped ZnO nanoparticles, their formulas and sources.

Material	Chemical Formula	Grade	Source
Zinc acetate dihydrate	$C_4H_6O_4Zn{\cdot}2H_2O$	99.5%, powder	Fluka
Silver Acetate	$C_2H_3AgO_2$	99.99%, powder	Aldrich
Polyvinyl pyrrolidone	$(C_6H_9NO)_n$	MW ~55000, powder	Aldrich
Sodium hydroxide	NaOH	97%, pellets	Merck
Ethylene glycol	$C_2H_6O_2$	99%, solution	Merck

5.2.2 Experimental procedures

A quantity of 0.1 M zinc acetate dihydrate solution was prepared in 40 mL EG at 25°C. In the meantime, the required amounts of silver acetate were dissolved in 20 mL DI-water at 25 °C to obtain Ag:Zn ratio as 0.3, 1 and 8 at. %. Then, Ag-containing solution was added into zinc acetate dihydrate solution using an automated injection pump (Top-5300 model syringe pump) at a rate of 20 mL/h. once injection was completed, the solution was further stirred at 700 rpm for 1 h to achieve complete homogeneity. Following the homogenization, the mixture was drop wise added into PVP solution (0.8 g PVP in 40 mL EG) and stirred for 15 min. Finally, 2 M NaOH solution was added into the solution mixture (at a rate of 20mL/h) until the pH of the final solution was measured as 12.7. Following the addition of NaOH solution for precipitation, the parent solution was aged at room temperature for 30 min. The powder products were

collected by centrifugation at 10000 rpm (using Eppendorf 5804 model, with a rotor radius of 115 mm) for 10 min and washed five times with DI-water. The obtained powders were dried at 70 °C for 3 h in a vacuum dryer and no further thermal treatment was performed. In addition to ZnO:Ag nanoparticles, for comparison, pure ZnO nanoparticles were also synthesized through the same experimental procedure with a small exception, where the initial aqueous silver acetate solution was replaced with equal amount of pure DI-water (20 mL). This sample will be referred as 0 at.% hereafter. A schematic representation of the experimental procedure are shown in Figure 5.1.

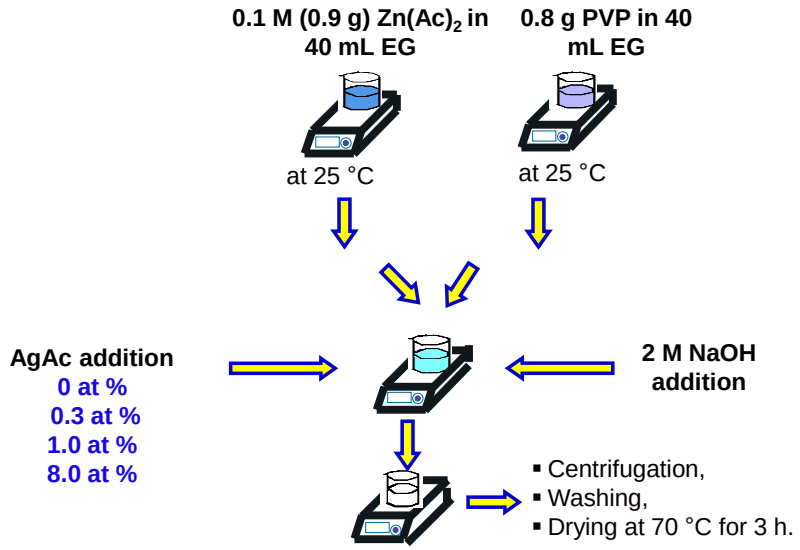

Figure 5.1. A schematic representation of experimental procedure for synthesis of Ag doped ZnO nanoparticles with precipitation method.

5.2.3 Materials characterization

X-ray diffraction (XRD) analyses were performed for phase identification and precise lattice parameter determination. A Rigaku D/Max-2000 PC diffractometer was employed, using Cu-Kα radiation (λ=1.54 Å) and X-ray source operating voltage of 40 kV. The typical XRD scans were performed in a 2θ range of 5-92° and at a rate of 2°/min. The Rietveld refinement was conducted on XRD patterns obtained at a rate of 0.5°/min in a 2θ range of 30-60°.

X-ray photoelectron spectroscopy (XPS) analyses were performed for chemical identification and evaluation of the chemical state of the constituent elements. XPS spectra were collected using a PHI 5000 spectrometer. The quantitative analyses for chemical identification were performed using high resolution scans of the O(1s), Zn(2p) and Ag(3d) spectral regions. The binding energies and charge corrections were referenced to the C(1s) line at 284.6 eV.

The size and morphology of the samples were examined with JEOL 2100 F model transmission electron microscope (TEM). The representative TEM samples were prepared simply by drop casting ultrasonically dispersed aqueous powder suspensions onto holey carbon coated copper grids.

The optical properties of the particles were investigated by ultraviolet-visible (UV-Vis) absorption double beam spectrophotometer (Varian-Cary100 Bio) in a wavelength range of 300-550 nm. Samples were dispersed in DI-water by 10 min ultrasonication for complete dispersion of the powders. The background contribution was evaluated using DI-water as reference.

The photocatalytic activities of pure and ZnO:Ag nanoparticles were determined through time dependent photodegradation studies of an aqueous dye (methylene orange, MO) solution. The dye stock solution was prepared by dissolving 50 mg MO in 50 mL DI-water. In a typical photocatalytic activity measurement, 50 mg powder sample was added to the MO stock solution and dispersion was continuously stirred under UV illumination generated by a 100W UV lamp enclosed in a dark box. Then, 4 mL of the sample solution was collected using a disposable syringe in every 30 min intervals. The samples were filtrated through nylon membranes and the aliquots were analyzed using an Optima SP-300 model UV–Vis spectrophotometer. The absorption spectra were recorded in the range of 300-600 nm and photocatalytic degradation of the MO was monitored based on the intensity of the characteristic absorbance band of the dye at 465 nm. The background contribution was evaluated using DI-water reference. The percentage of remaining MO dye as a function of UV-illumination time

was determined by normalizing the measured absorbance intensity (at 465 nm of MO dye) to the initial (pre-irradiation) one of the MO stock solution.

The decomposition efficiency rate of MO was normalized to the initial (pre-irradiation) absorbance of MO and calculated using the following equation;

$$R\ (\%) = (A_0 - A)/A_0 * 100 \qquad 5.1$$

where A_0 and A are the equilibrium concentration of MO before and after UV irradiation, respectively. For the photocatalytic measurements of the different samples, 0.05 g sample was dispersed into MO solution.

5.3 Results and discussion

5.3.1 Phase and crystal structure analyses

Figure 5.2 illustrates the wide range XRD diffractograms of the ZnO:Ag nanoparticles synthesized through the precipitation method with varying amount of Ag incorporation (at. % Ag range from 0.1 at. % to 10 at. %) at 25 °C precipitation temperatures. XRD pattern for the undoped ZnO nanoparticles is also provided for comparison. The diffractograms are representative for the samples in as-precipitated condition (dried at 70 °C) without any subsequent thermal treatment. The XRD pattern of the undoped sample can be indexed using wurtzite crystal structure of ZnO (hexagonal wurtzite structure, with JCPDS card no: 36-1451) and no other crystalline phases were detected.

The XRD diffractograms reveal that for low concentration of silver addition (0.1 and 0.3 at.% Ag), all of the diffraction peaks belong to crystalline ZnO. For higher Ag addition (1 at.% Ag), appearance of a very low-intensity peak at $2\theta = 38.11°$ was observed. Addition of high concentration silver solution (equal and higher than 2 at.% Ag) leads to appearance of new peaks located at $2\theta = 44.28°$, 64.43° and 77.47° which are for metallic silver (JCPDS card no: 4-0783). Increase in silver amount results in higher intensity for silver diffraction peaks. Although there are many studies reporting

the formation of metallic silver by thermal reduction of ionic silver at high temperatures (T>300 °C), formation of metallic silver here occurred without any calcination treatments.

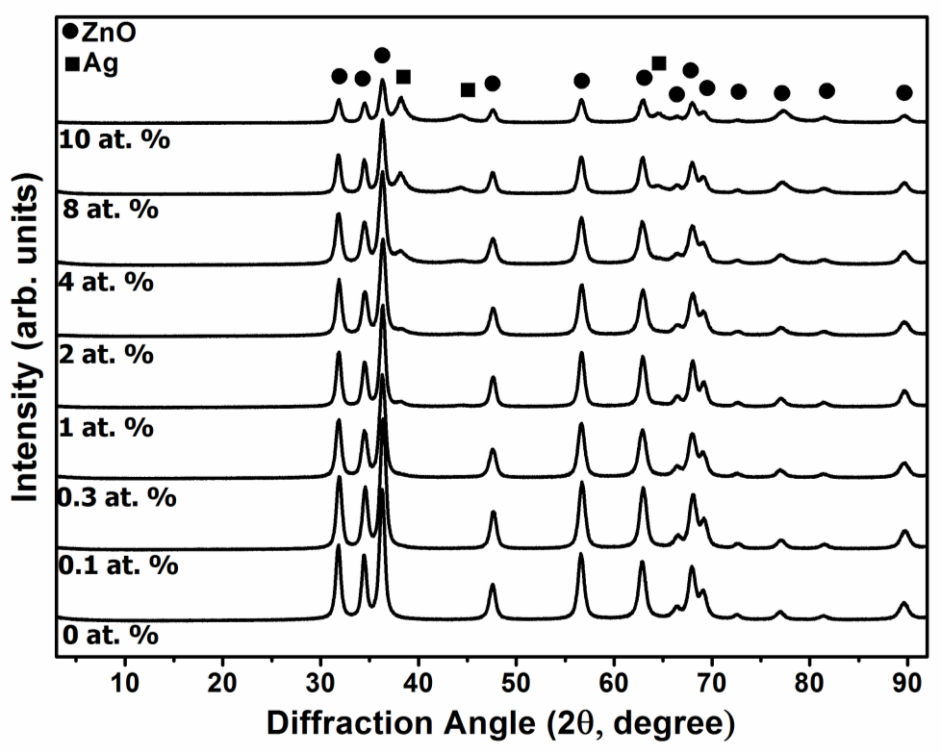

Figure 5.2. XRD patterns of precipitation products synthesized with different concentration of silver acetate.

In order to investigate the effect of the heat treatment on the formation of metallic silver, 0.3 and 1 at.% Ag incorporated ZnO samples were calcined for 3 h at 500 °C. Figure 5.3(a) and (b) show the XRD diffractograms of the reaction products for samples prepared with addition of 0.3 and 1 at.% Ag incorporated ZnO samples silver acetate in *as-prepared* condition and *after calcination* for 3 h at 300 °C. Figure 5.3(a) indicates crystalline ZnO for both samples in *as-prepared* condition and *after calcination.* Heat treatment does not have an important influence on the pure ZnO samples. However, for 1 at.% Ag incorporated ZnO samples (Figure 5.3(b)), heat treatment results in an increase in the intensity of both ZnO and metallic silver diffraction peaks so increase in the crystallite of both phases.

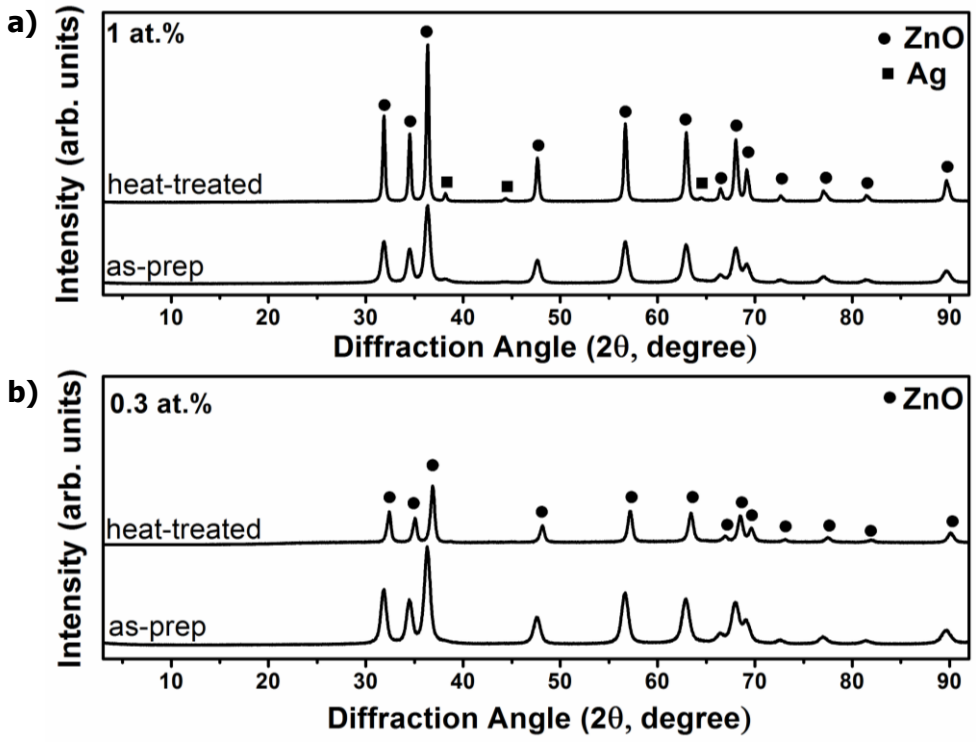

Figure 5.3. XRD patterns of precipitation products of as-prep condition and after calcined at 500 °C for 3h (a) 0.3 at.% Ag and (b) 1 at.% Ag addition.

In this present investigation, a wide concentration range of silver addition were studied. However, it is worth to mention that this ionic substitution occurs up to a limited extent. According to XRD results, up to 0.3 at. % Ag addition, all Ag are substitute into ZnO crystal. For the higher amount of the Ag addition (1 at. % Ag), presence of the metallic Ag peaks indicates that there is a critical Ag addition limit for the substitution of Ag into ZnO crystal which is between 0.3-1 at. % Ag. Extensively high silver incorporation (8 at.% Ag) leads to metallic silver formation most likely together with some ionic incorporation. Therefore, a more detailed structural analyses was performed on the samples with ionic silver incorporation (i.e. 0.3, and 1 at.% Ag) and metallic silver incorporated (8 at.% Ag) samples.

The possible incorporation of Ag into the ZnO lattice and the effect of the Ag doping on the crystal structure can be examined by monitoring the peak positions of ZnO diffractions. According to previous reports, segregation of Ag to the grain boundaries

of ZnO crystal resulted in no positional shift in the XRD diffractograms [20, 24]. On the other hand, substitutional or interstitial incorporation of the Ag into the ZnO lattice leaded to measurable peak shifts to relatively lower [25] or higher [26] 2θ values, respectively. Figure 5.4 shows the enlarged regional XRD patterns of the samples within the 2θ range of 30-40° acquired at a relatively slow scan rate of 0.5°/min. The vertical drop lines were added for visual guidance and they correspond to peak positions in the JCPDS card of ZnO.

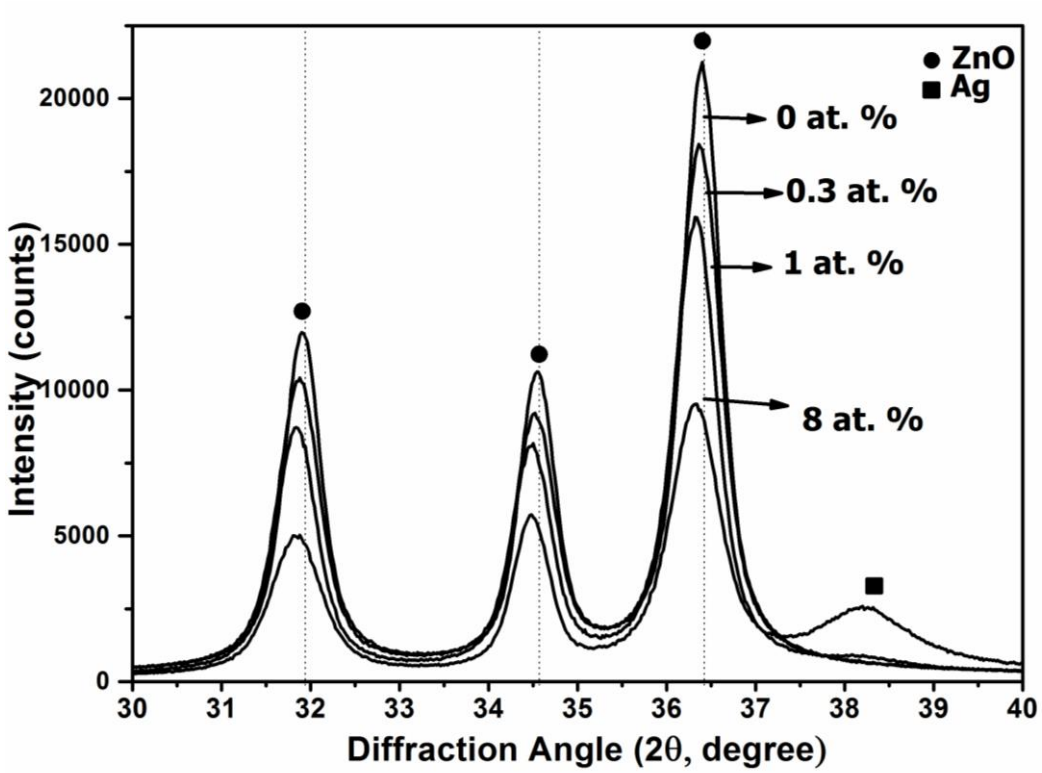

Figure 5.4. Enlarged region of the XRD patterns of ZnO:Ag nanoparticles with different Ag contents (0.3, 1, and 8 at.% Ag). The pattern of pure ZnO (0 at.% Ag) is given for comparison purposes.

It is clear that, ZnO peak positions shift to relatively lower 2θ values with an increase in Ag concentration, suggesting substitution of Ag^{+} ions into the ZnO lattice. The diffraction angles for $(10\bar{1}1)_{ZnO}$ are listed in the Table 5.2. The positional shift to lower 2θ values is reasonable, as a lattice enlargement was expected due to ionic size

difference between Ag^{+} (1.26Å) and Zn^{2+} (0.74Å) ions [27]. However, it is worth to mention again that this ionic substitution occurs up to a limited extent. According to XRD results, up to 0.3 at. % Ag addition, all Ag are substitute into ZnO crystal (without any Ag diffraction). For the higher amount of Ag addition (1 at. % Ag), coexistence of the very low intensity metallic Ag peaks and positional shift of the ZnO peaks indicates the presence of both Ag clusters and substitution of the Ag^{+} ions into the ZnO lattice. Thus, it can be concluded that there is a critical Ag addition limit for the substitution of Ag into ZnO crystal which is between 0.3-1 at. % Ag.

Table 5.2. $(10\bar{1}1)_{ZnO}$ peak positions, c lattice parameters, Zn occupancy values, XRD crystallite size estimated from Rietveld analyses and average particle size determined from TEM images of pure ZnO and ZnO:Ag nanoparticles.

Silver Acetate (at %)	$(10\bar{1}1)$ **Peak Position (degree of 2θ)**	**Lattice Parameter (c)**	**Occupancy (Zn)**	**XRD Crystallite Size (nm)**	**TEM Particle Size (nm)**
0	36.39	5.240	1.00	22.1	21.2 ± 3.3
0.3	36.37	5.246	0.895	20.3	19.1 ± 2.9
1.0	36.35	5.258	0.866	19.6	18.0 ± 3.0
8.0	36.33	5.262	0.819	18.4	14.2 ± 1.7

In order to obtain more detailed structural analyses, Rietveld refinement method was applied to XRD data. The Rietveld refinement analyses were done using General Structural Software [28] with the EXPGUI graphical user interface [29]. Figure 5.5 indicates Rietveld refinement applications of the XRD diffractograms for the samples. The refinements were done using the $P6_3mc$ space group with (1/3, 2/3, 0) the atomic position of Zn and (1/3, 2/3, 0.3817) atomic position of O [30] and *Fm-3m* space group with (0, 0, 0) atomic position of Ag. The lattice parameter variation with increasing Ag amount was determined from the Rietveld refinement results and is also listed in the Table 5.2.

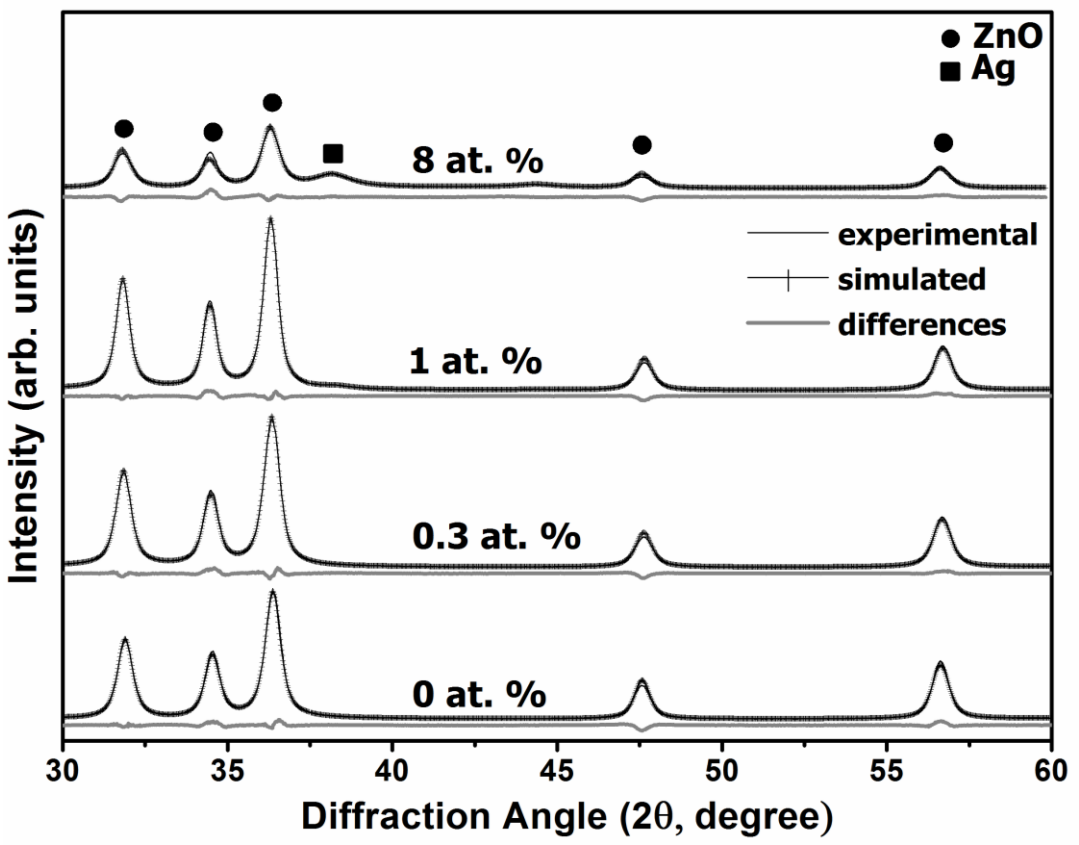

Figure 5.5. Rietveld refinement analyses of ZnO:Ag nanoparticles with different Ag contents (0.3, 1, and 8 at.% Ag). The pattern of pure ZnO (0 at.% Ag) is given for comparison purposes.

The change in the c lattice parameter from 5.240 Å for pure ZnO (0 at. % Ag) to 5.262 Å for highest amount of Ag incorporated sample (8 at. % Ag) clearly indicates the increase in the lattice size upon doping. Thus, the Rietveld refinement results are in good agreement with the previous conventional XRD data and relevant interpretations, indicating a possible expansion of ZnO lattice due to substitution of larger Ag^{+} ions with the Zn^{2+} ions in the lattice.

In order to determine the exact atomic sites for Ag^{+} ions, the atomic occupancies for Ag were varied for the Zn and O sites. The best fits were achieved when Ag^{+} ions occupy the Zn^{2+} sites. The occupancy values of Zn are also listed in the Table 5.2. According to occupancy values, increasing amount of Ag addition leads to a decrease

in the Zn occupancy. Therefore, it can be assumed that O vacancies were created due to charge differences between Ag^{+} and Zn^{2+} ions. Similar findings have also been reported by Singhal et al. [31] and Wang et al. [11]. These occupancy correlations verify the extensive incorporation of the Ag^{+} ions into Zn^{2+} sites with the increasing amount of Ag. Meanwhile, the average crystallite size for ZnO particles estimated from Rietveld refinement results are also presented in the Table 5.2. The results indicate that the particle size vary in the range of 18-22 nm, yet decreasing with Ag content.

Figure 5.6 shows the EDX data and elemental mapping images Zn, O and Ag elements of ZnO particles synthesized with 1 at.% Ag addition. An approximate chemical composition of ZnO powders was also determined with the EDX analysis accompanied with elemental mapping analysis. EDX data revealed that the particles were composed of Zn, O and Ag elements. Meanwhile, the elemental mapping images confirmed homogenous distribution of zinc, oxygen and silver suggesting homogeneous distribution of silver.

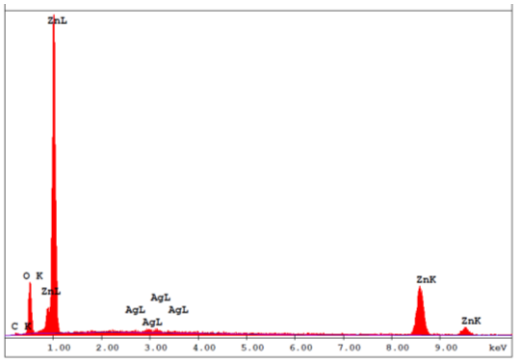

Element	Weight %	Atomic %
O	22.54	52.35
Zn	73.10	41.54
Ag	2.68	0.92
C	1.68	5.19
Total	100.00	100.00

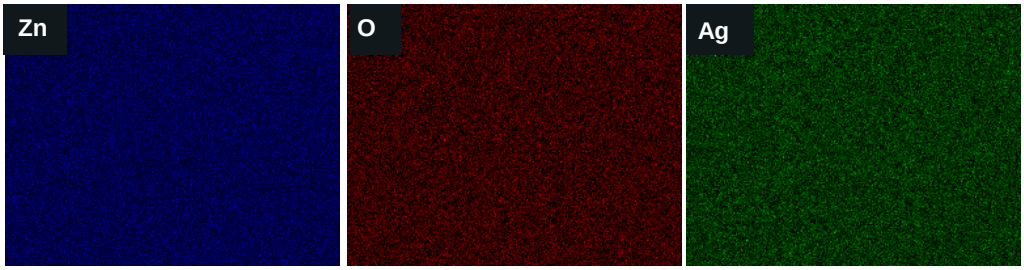

Figure 5.6. EDX data and elemental mapping images Zn, O and Ag elements of ZnO particles synthesized with 1 at.% Ag addition.

5.3.2 Spectroscopic analyses of ZnO and ZnO:Ag nanoparticles

The chemical composition and defect chemistry of ZnO:Ag nanoparticles were also investigated through XPS analyses. The XPS spectra ZnO:Ag nanoparticles (0.3, 1 and 8 at. % Ag) are shown in Figure 5.7. The spectrum for pure ZnO (0 at. % Ag) is also provided for comparison. The major signals in survey spectra shown in Figure 5.7 (a) confirmed the presence of Zn, O and C in all samples and Ag in the highest amount of Ag incorporated sample (8 at. % Ag). The low intensity C signal is most likely due to trace amount of PVP remains or simply due to adsorption of organic contaminants during handling.

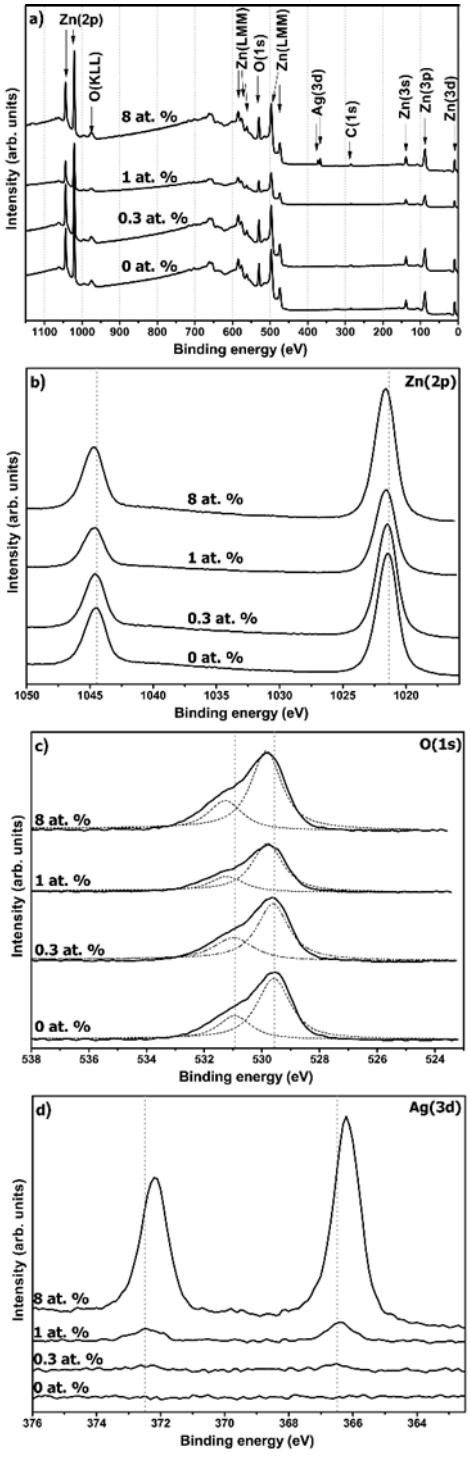

Figure 5.7. XPS spectra of ZnO:Ag nanoparticles with different Ag contents (0.3, 1 and 8 at. % Ag) (a) survey XPS spectrum, high resolution regional XPS spectra of (b) Zn(2*p*), (c) O(1*s*) and (d) Ag(3*d*). The spectrum of pure ZnO (0 at. % Ag) is given for comparison purposes.

The informative Zn, O and Ag spectral portions of the survey analyses are presented by the accompanying high resolution regional spectra shown Figure 5.7. (b), (c) and (d), respectively. The corresponding binding energies (BE in eV) for the Zn(2*p*), O(1*s*) and Ag(3*d*) signals, as determined from these high resolution scans are summarized in Table 5.3. According to Figure 5.7. (b), due to strong spin orbit coupling, Zn(2*p*) signal splits into two symmetrical peaks as Zn($2p_{3/2}$) and Zn($2p_{1/2}$). For pure ZnO nanoparticles (0 at. % Ag), these peaks are located at 1021.41 and 1044.48 eV, respectively. These are in agreement with the previously reported binding energies for stoichiometric ZnO [32]. Locations of these peaks slightly shift to higher BE values, with Ag doping.

Table 5.3. Binding energy values (in eV) of Zn($2p_{3/2}$), Zn($2p_{1/2}$), O(1*s*) (lattice and chemisorbed oxygen), Ag($3d_{5/2}$) and Ag($3d_{3/2}$) for pure ZnO and ZnO:Ag nanoparticles.

Silver Acetate (at %)	**Binding energy (eV)**					
	Zn ($2p_{3/2}$)	**Zn ($2p_{1/2}$)**	**O(1*s*)***	**O(1*s*)****	**Ag($3d_{5/2}$)**	**Ag($3d_{3/2}$)**
0	1021.41	1044.48	529.57	530.95	-	-
0.3	1021.48	1044.60	529.62	531.01	366.50	372.51
1.0	1021.57	1044.63	529.78	531.23	366.39	372.47
8.0	1021.59	1044.69	529.83	531.27	366.20	372.18

* *: lattice oxygen*
** *: chemisorbed oxygen*

Figure 5.7. (c) indicates asymmetric O(1*s*) signals which can be divided into two symmetrical signals. For pure ZnO (0 at. % Ag), the lower energy of O(1*s*) signal at 529.57 eV was attributed to lattice oxygen atoms and the high energy portion of O(1*s*) signal located at 530.95 eV was associated with the chemisorbed oxygen, such as surface hydroxyl groups [33]. The O(1*s*) binding energies are also in agreement with the ones reported for stoichiometric ZnO [34]. Ag addition results in the positional shift in O(1*s*) spectra to higher BE values as shown in the Table 5.3.

The binding energies of Zn(2*p*) and O(1*s*) signals increase gradually with the Ag content for doped samples and more significantly deviates from that of stoichiometric ZnO values. This can be due to the changes in the charge transfer mechanism from Zn^{2+} to O^{2-} ions that can be affected by the vacancies, as also proposed by Sahu et al. [35]. This signifies that the number of vacancies increase with the dopant addition. This is in agreement with the Rietveld analyses, suggesting an increase in the number of oxygen vacancies with Ag addition.

A thorough investigation of Ag(3*d*) signals in high resolution spectra (Figure 5.7. (d)) provide additional insights into the chemical nature of doping. The Ag($3d_{5/2}$) and Ag($3d_{3/2}$) peaks at ~366 and ~372 eV, respectively, were observed for the samples 1 and 8 at. % Ag, yet the peaks were hardly visible for the low amount of Ag containing sample (0.3 at. % Ag). The BE's for Ag(3*d*) signals are also summarized in Table 5.3. The signals for the Ag(3d) spectra for the sample with the highest amount of Ag (8 at. % Ag) are well defined. The splitting in the BE's of Ag($3d_{5/2}$) and Ag($3d_{3/2}$) signals in 6 eV shows that Ag were mainly in the metallic state (Ag^0) [6, 36]. Another observation from the XPS spectra of Ag is the shift in Ag(3*d*) peak positions towards lower BE's with the increasing Ag addition. This shift can be attributed to the interaction between Ag and ZnO crystal, which leads to the adjustment of their Fermi level to same value [17, 37]. During the interaction, the free electrons on the new Fermi level of the Ag could tunnel through the empty region within the conduction band of the ZnO crystal. Therefore, the interaction between Ag and ZnO crystal results in the formation of a higher valance for Ag [35, 38]. The positional shift to lower BE's indicates the formation of an oxide layer on Ag particle surface, which is most likely below the detection limit of XRD.

The chemical nature of the precipitation products containing various Ag amounts were also investigated with FTIR spectroscopy. The spectra of PVP and ZnO:Ag nanoparticles are shown in Figure 5.8. The spectrum of pure ZnO nanoparticles (0 at. % Ag) is also provided for comparison.

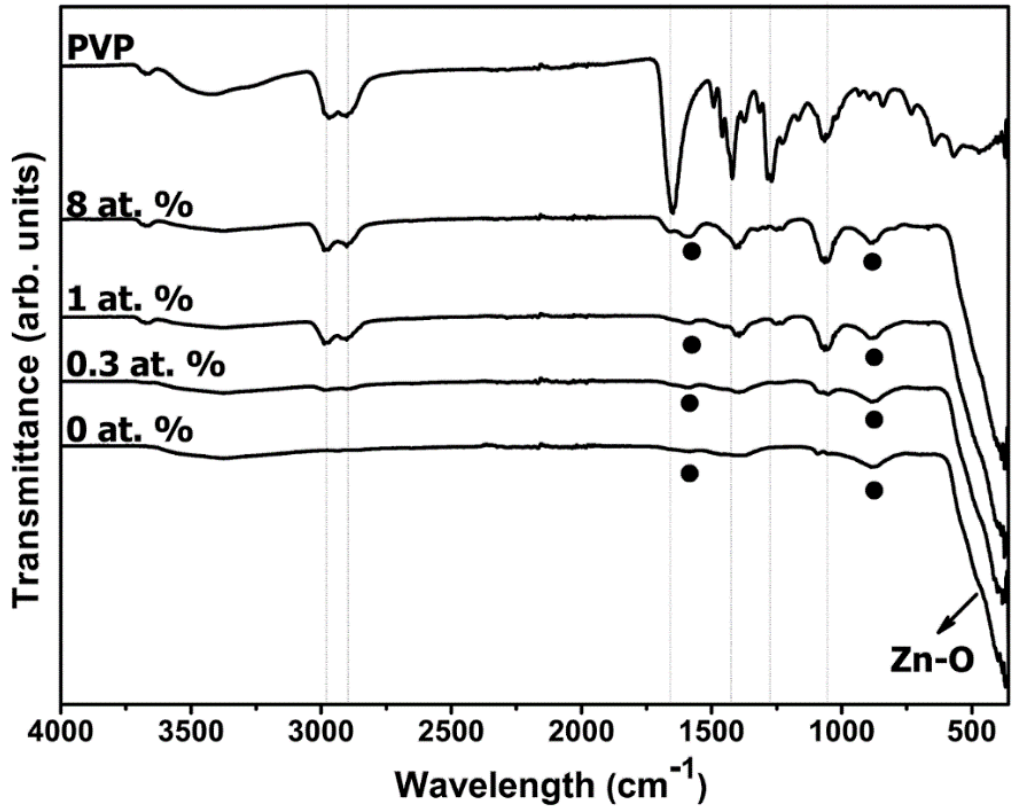

Figure 5.8. FTIR spectra of ZnO:Ag nanoparticles with different Ag contents (0.3, 1 and 8 at. % Ag). The spectra of pure ZnO (0 at. % Ag) and PVP are also given for comparison purposes.

The bands in PVP spectra located at 3667-3420 (O-H stretching vibration), 2967-2905 (CH_2 unsymmetrical stretching vibration), 1650 (C═O stretching vibration), 1420 (CH_2 bending vibration), 1280 (C-N stretching vibration) and 1065 cm^{-1} (C-O stretching vibration) are marked with dashed drop lines [39, 40].

In FTIR spectra of ZnO samples, besides the ZnO band (at ~400 cm^{-1}), the presence of weak absorption bands related with PVP shows that some organic molecules were remained/absorbed on the precipitation products. Moreover, in the spectra of the ZnO samples, two additional peaks marked with circles and located at 1580 cm^{-1} (C=N stretching vibration) and 880 cm^{-1} (N-O deformation vibration) appear. They indicate that the dominant structure of PVP is >N=C-O [40]. The FTIR spectra can be further

resolved to investigate the effect of Ag doping. For instance, FTIR spectra show no absorption bands related with AgO or Ag_2O [41]; therefore, Ag must be in metallic form and there is no chemical bonding between Ag-O and Ag-ZnO. These results support the XRD related comments on Ag incorporation into the ZnO lattice; Ag+ ions substitutionally dope the ZnO lattice for the samples 0 and 0.3 at. % Ag, whereas metallic Ag clusters form for the sample 8 at. % Ag. It is worth to mention that the silver oxide formation suggested by XPS data is somewhat contradictory with the FTIR results. This could be attributed to surface sensitive nature of XPS measurements and indicates that silver oxide forms only on the surface of the ZnO nanoparticles, most probably due to poor oxidation resistance of Ag under ambient conditions.

5.3.3 Microstructure and optical properties of ZnO and ZnO:Ag nanoparticles

The low magnification TEM images of synthesized ZnO nanoparticles are shown in Figure 5.9. Particle sizes obtained from TEM analyses are provided in Table 5.2. It is clear that the average particle size decreases with the increase in the Ag amount. These results are in agreement with the crystallite sizes obtained from Rietveld refinement. The change in the ZnO particle size with Ag addition implies that Ag clusters act as nucleation sites for the ZnO crystals. In addition, high resolution TEM images of same samples are shown in Figure 5.10. Fringes of individual planes are clearly visible in the images suggesting the single crystalline nature of the nanoparticles. Inverse fast Fourier transform (IFFT) patterns are shown in Figure 5.11 and they show lattice spacing of single crystal ZnO nanoparticles. For the pure ZnO nanoparticles, distance between adjacent fringes measured as 0.16 nm, is in good agreement with the interplaner spacing of $(11\bar{2}0)$. For the IFFT pattern of samples 0.3 and 1 at. % Ag, the spacing between adjacent fringes is measured as 0.19 and 0.21 nm, respectively. They are quite close to the d spacing of the $(10\bar{1}2)$ plane. IFFT pattern of sample 8 at. % Ag indicates a lattice spacing of 0.26 nm corresponding to the (0002) plane of the ZnO crystal.

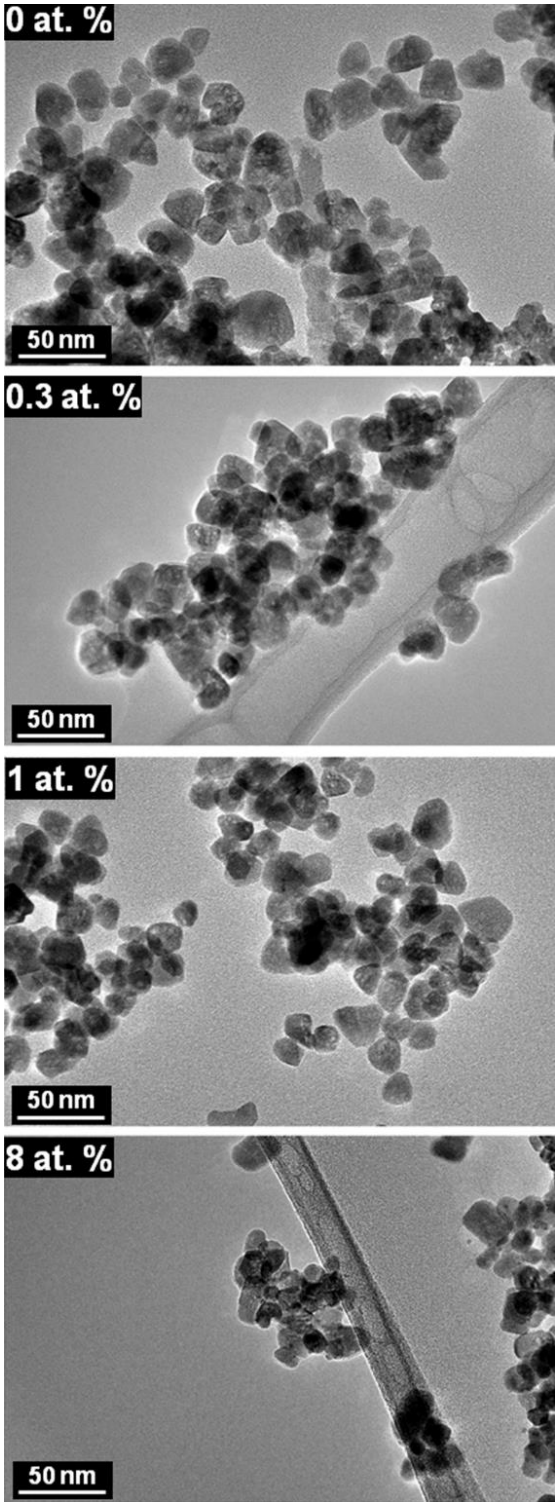

Figure 5.9. The low magnification TEM images of ZnO:Ag nanoparticles with different Ag contents (0.3, 1 and 8 at. % Ag). The image of pure ZnO (0 at. % Ag) is given for comparison purposes.

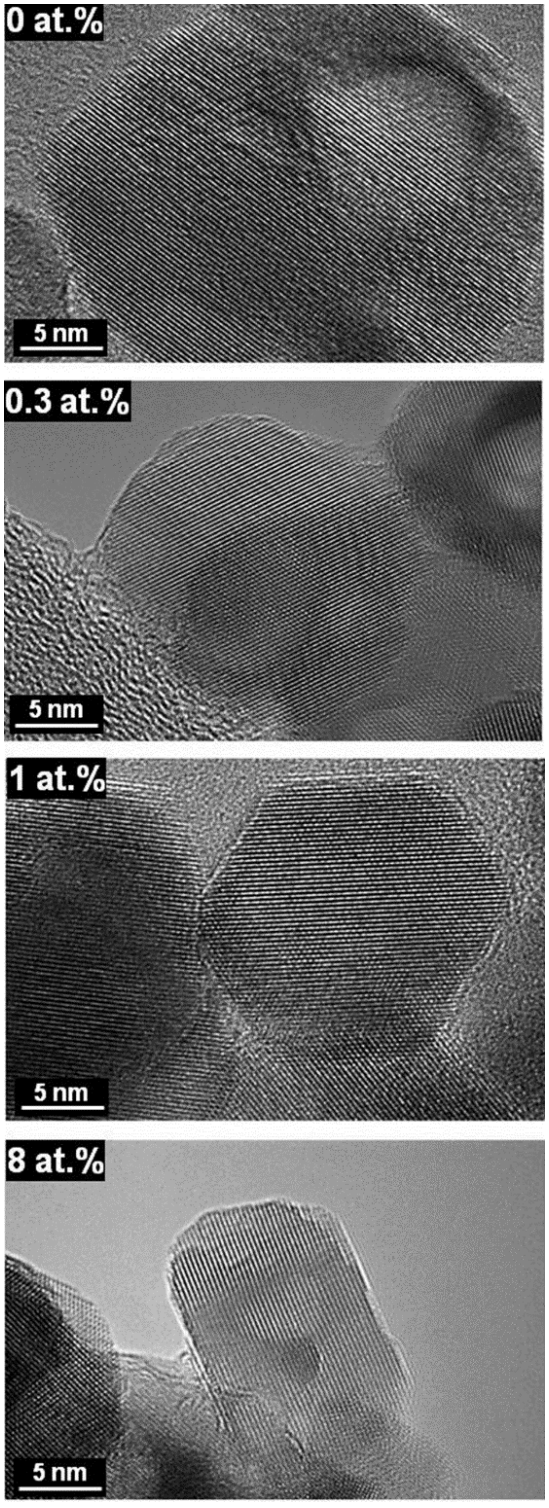

Figure 5.10. The high resolution TEM images of ZnO:Ag nanoparticles with different Ag contents (0.3, 1 and 8 at. % Ag). The image of pure ZnO (0 at. % Ag) is given for comparison purposes.

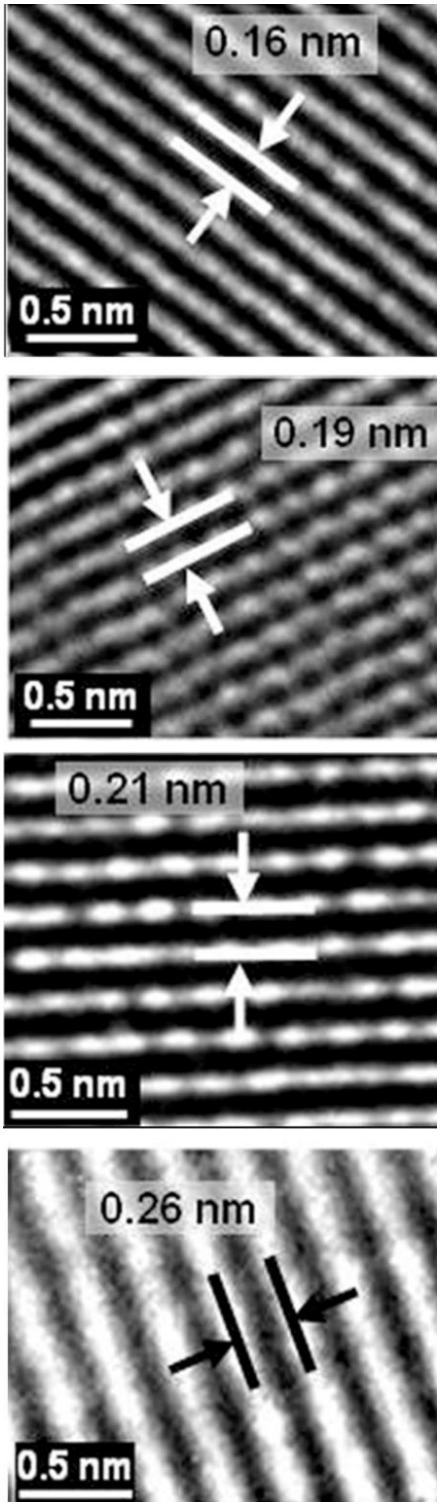

Figure 5.11. IFFT patterns of ZnO:Ag nanoparticles with different Ag contents (0.3, 1 and 8 at. % Ag). The patterns of pure ZnO (0 at. % Ag) are also given for comparison purposes.

UV–Vis spectroscopy analyses were performed to determine the effect of Ag amount on the optical properties of the ZnO nanoparticles. Figure 5.12 shows the UV-Vis spectra of the ZnO:Ag nanoparticles. Spectrum for the pure ZnO (0 at. % Ag) nanoparticles is also provided for comparison. Pure ZnO nanoparticles show UV absorption edge at 346 nm related with the wurtzite crystal structure of ZnO [42]. Ag addition to the ZnO nanoparticles red shifts the location of the absorption edge, as labeled in Figure 5.12. Upon the reduction of particle size, blue shift should occur [43], on the contrary to the results obtained from the UV-Vis analyses. This contradiction can be explained through the substitution of Ag^{+} ions into the Zn^{2+} sites of the ZnO lattice, compensating for the particle size effect. A similar change has been reported in the literature [44, 45].

Absorption edge shift also shows the variation of the direct bandgap of the particles. The direct bandgap energies (E_g) of ZnO nanoparticles are obtained by plotting the absorption coefficient (α)–photon energy graph (hυ) and extrapolating the straight-line portion of this plot to the hυ axis as shown an inset in the Figure 5.12. For the pure ZnO nanoparticles (0 at. % Ag), E_g was determined as 3.241 eV, which decreases to 3.237, 3.229 and 3.207 eV for the ZnO:Ag nanoparticles for the samples 0.3, 1 and 8 at. % Ag, respectively. Absorption edges and thus E_g values of the ZnO nanoparticles depend on the size, shape, defect state and dopant content of the particles. It has been reported by *Zheng et al*. that in the presence of oxygen vacancies, electrons excited from the valance band (VB) to conduction band (CB) can easily transform to oxygen vacancies, resulting in the reduction of the bandgap energy [17, 46]. Previously presented Rietveld analyses were suggesting the formation of oxygen vacancies for the doped samples due to the charge differences between Ag^{+} and Zn^{2+} ions. Furthermore, the CB electrons excited from the VB move through the Fermi level of the Ag clusters. The electron transfer will continue until the overall Fermi level of Ag and CB value of ZnO come to same value. As Ag content increases, more electron transfer should be expected, corresponding to lower E_g values. Therefore, increasing Ag content provides the formation of the higher number of oxygen vacancies leading to a decrease in the E_g value. In addition, the UV-Vis spectra for the samples 0, 0.3 and 1 at. % Ag only have one absorption peak that is related to ZnO. However, the

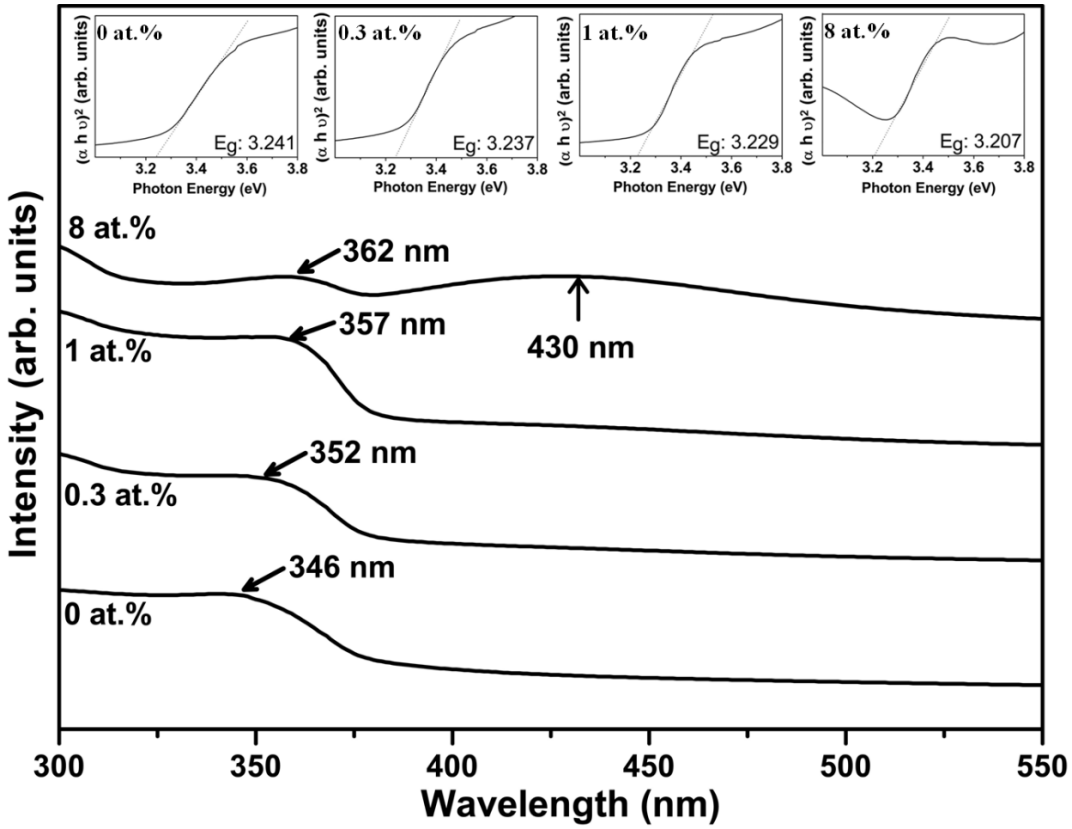

Figure 5.12. The UV-Vis spectra of ZnO:Ag nanoparticles with different Ag contents (0.3, 1 and 8 at. % Ag). The spectrum of pure ZnO (0 at. % Ag) is given for comparison purposes. Band edge locations of samples are also given in the figure. The insets in Figure 5.12 show plots of $(\alpha h\nu)^2$ as a function of photon energy (E_g) for all samples (the solid lines are for the visual help).

spectrum of the sample 8 at. % Ag is dominated with absorption band centered at 430 nm. This band is associated with the surface plasmon resonance of metallic Ag particles [47]. This result is in agreement with the XRD results shown in Figure 5.12, in which metallic Ag clusters formation was observed for the sample containing 8 at. % Ag.

5.3.4 Photocatalytic activity of ZnO and ZnO:Ag particles

Figure 5.13 shows absorption spectra of MO solutions under the UV irradiation 0.3, 1 and 8 at.% Ag incorporated ZnO nanoparticles. Photocatalytic results of the MO without sample and pure ZnO nanoparticles are also provided for comparison. The photodegradation of the control solution (MO solution in the absence of ZnO nanoparticles) after 120 min was determined as 3%. Pure ZnO nanoparticles exhibited some photocatalytic activity. The remaining dye was 15.9% of its initial amount after 120 min of UV-irraditaion. The photocatalytic activity of ZnO nanoparticles was improved by the Ag addition. For the sample containing 0.3 at. % Ag, the complete decomposition of MO dye was achieved after 90 min of UV irradiation. The time for the complete decomposition decreased to only 60 min for the samples containing 1 and 8 at. % Ag.

Temporal profile of MO degradation of ZnO:Ag nanoparticles with different Ag contents (0.3, 1 and 8 at. % Ag) under the UV illumination are provided in Figure 5.14. Degradation profile of pure ZnO (0 at. % Ag) and MO control solution are also given for comparison purposes. In literature, better photocatalytic activities for ZnO:Ag nanoparticles were reported [17, 18]. Leaner photocatalytic ability of ZnO:Ag nanoparticles in our case may originate from PVP molecules absorbed on the ZnO:Ag particles (Figure 5.8).

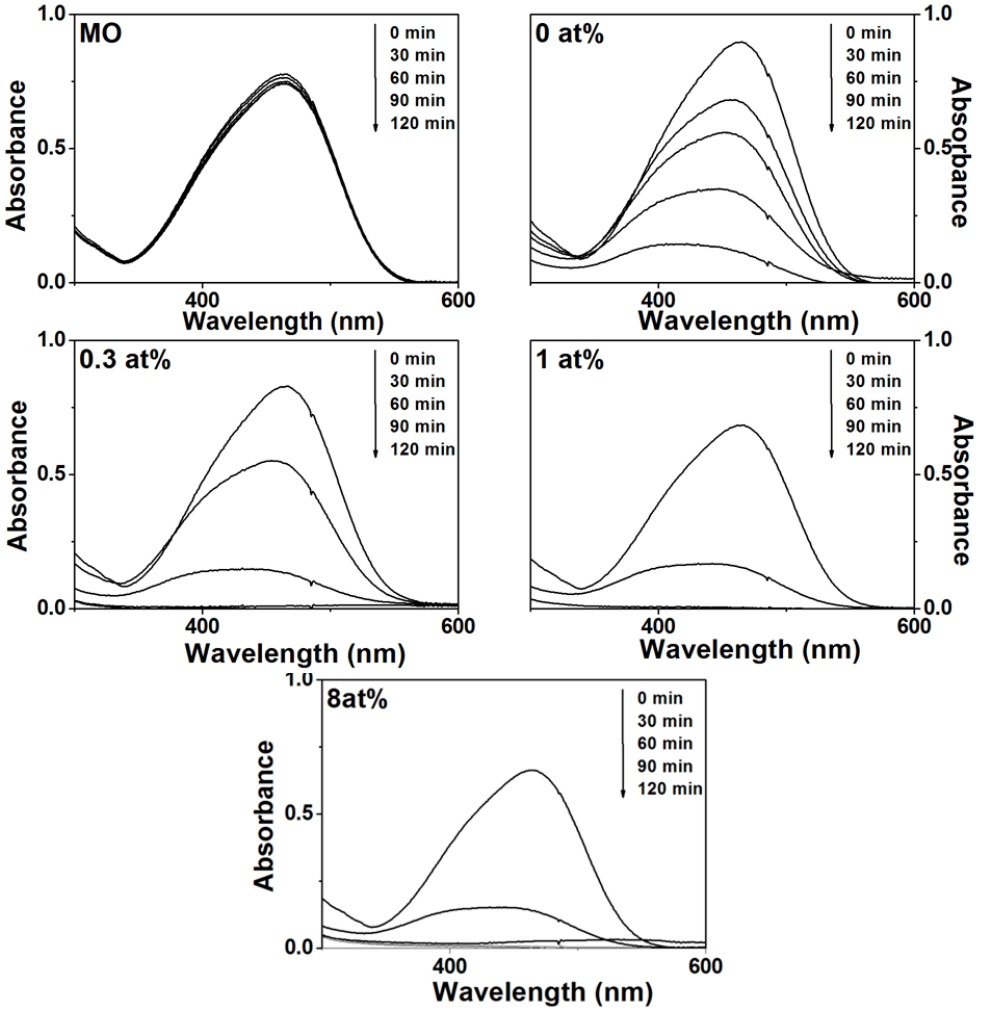

Figure 5.13. Absorption spectra of MO solutions under the UV irradiation in the presence of any sample and pure ZnO and 0.3, 1 and 8 at.% Ag incorporated ZnO nanoparticles.

There are several mechanisms accounted for improving the photocatalytic activities of the semiconductor materials. Georgekutty et al. reported that mechanism of the photocatalytic reactions in the presence of a dye is based on the electron transfer from dye to both CB of ZnO and Fermi level of Ag, which also simultaneously makes electron transfer from CB of ZnO [21]. Thus, in the presence of both ZnO:Ag and dye molecules, active oxygen species form as a result of the reaction between CB electrons and dissolved oxygen in the solution. These active oxygen species are responsible for the dye degradation and their number increases with Ag content.

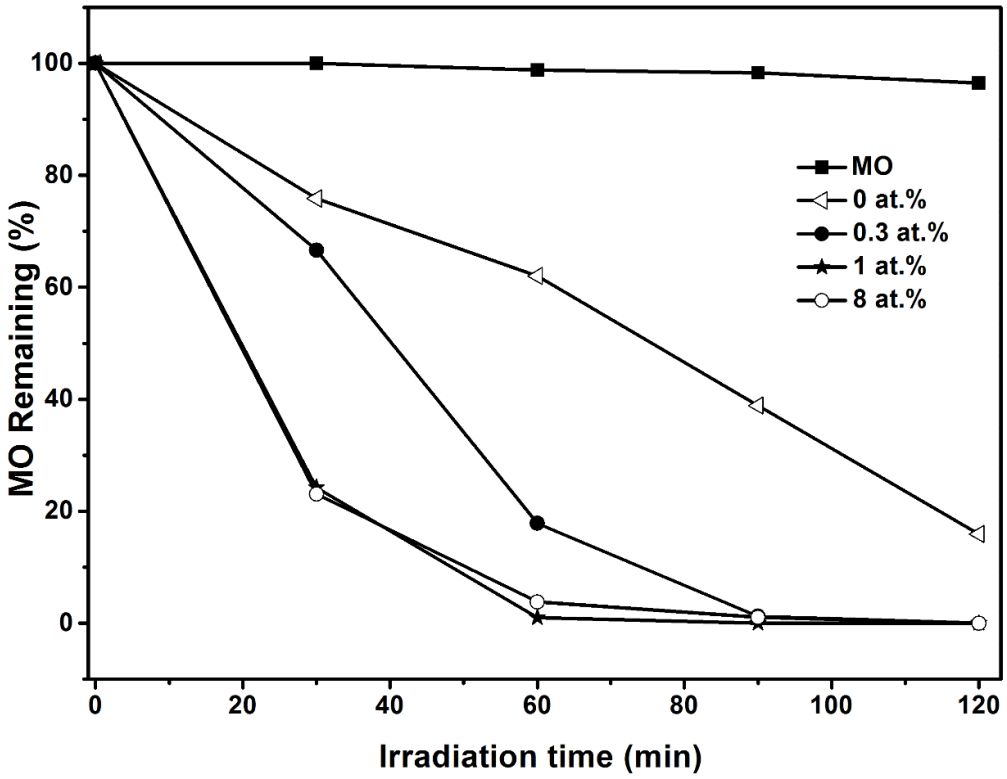

Figure 5.14. Temporal profile of MO degradation of ZnO:Ag nanoparticles with different Ag contents (0.3, 1 and 8 at. % Ag) under the UV illumination. Degradation profile of pure ZnO (0 at. % Ag) and MO control solution are also given for comparison purposes.

Consequently, increasing Ag content provides an improvement in the photocatalytic activity of the ZnO nanoparticles. Sun et al. also reported a correlation between particle size and photocatalytic ability of ZnO:Ag nanoparticles [48] since the decrease in the particle size results in the reduction of the recombination chances of the $e^-/h^\bullet$ pairs. Furthermore, Zheng et al. reported that the higher photocatalytic efficiency can be associated with oxygen defects which provide the transformation of the photogenerated electrons to the dye in solution [16]. On the basis of the these discussion, it can be concluded that in our case, photocatalytic activities of the ZnO nanoparticles increase with Ag content, this results in a decrease in the particle size thus, an increase in the surface area and also results in an increase in the oxygen defects. This result agrees with the accepted mechanisms for the enhancement of the photocatalytic activities of ZnO nanoparticles.

However, there is saturation in the photocatalytic activity, since sample with the smallest particle size and highest amount of Ag (8 at. % Ag) shows very similar activity with the sample containing 1 at. % Ag in degrading MO dye. This can be explained by several means. First, as Ag appears as metallic nanoparticles in this sample, these particles may limit the amount of available free surface area of ZnO to interact with light and adsorb the dye molecules [49]. In addition, small particle sizes correspond to a large specific surface area and large number of surface active sites to react with the adsorbed molecules. This enables the formation of active radicals. However, very fine particles may enhance recombination, as the charge carriers would be generated very close to the particle surface. Thus, recombination becomes faster than the interfacial charge transfer decreasing the photocatalytic activity of the particles [50]. Obtained results clearly indicated that there is an optimum amount of Ag that needs to be doped to ZnO and a critical particle size for the improved photocatalytic performance, such as sample containing 1 at. % Ag used in the experiments.

5.4 Conclusions

ZnO:Ag nanoparticles were synthesized at room temperature via precipitation and photocatalytic activity was investigated. A systematic study on the effect of silver content on the structural/optical properties and photocatalytic activities of ZnO nanoparticles has been performed. It was found that Ag addition shifts the XRD peak positions of wurtzite ZnO to lower diffraction angle values, designating an expansion in the lattice parameter (c). Silver presence also decreases the bandgap of ZnO as revealed by the change in the absorption edge to longer wavelengths. These results showed that Ag+ ions substitute into Zn^{2+} sites within the ZnO lattice. Increasing Ag content up to a critical value leads to an enhancement in the photocatalytic activity of ZnO:Ag nanoparticles while excessive addition were found to decrease the photocatalytic activity.

5.5 References

1. Gupta T.K., Journal of the American Ceramic Society, **1990** 73(7) p. 1817-1840.

2. Saito S., Miyayama M., Koumoto K., and Yanagida H., Journal of the American Ceramic Society, **1985** 68(1) p. 40-43.

3. Li Y.B., Bando Y., and Golberg D., Applied Physics Letters, **2004** 84(18) p. 3603-3605.

4. Choopun S., Tubtimtae A., Santhaveesuk T., Nilphai S., Wongrat E., and Hongsith N., Applied Surface Science, **2009** 256(4) p. 998-1002.

5. Jang Y.H., Kochuveedu S.T., Cha M.-A., Jang Y.J., Lee J.Y., Lee J., Lee J., Kim J., Ryu D.Y., and Kim D.H., Journal of Colloid and Interface Science, **2010** 345(1) p. 125-130.

6. Wu M., Yang B., Lv Y., Fu Z., Xu J., Guo T., and Zhao Y., Applied Surface Science, **2010** 256(23) p. 7125-7130.

7. Hoffmann M.R., Martin S.T., Choi W., and Bahnemann D.W., Chemical Reviews, **1995** 95(1) p. 69-96.

8. Karunakaran C., Rajeswari V., and Gomathisankar P., Materials Science in Semiconductor Processing, **2011** 14(2) p. 133-138.

9. Serpone N., Maruthamuthu P., Pichat P., Pelizzetti E., and Hidaka H., Journal of Photochemistry and Photobiology A: Chemistry, **1995** 85(3) p. 247-255.

10. Ekambaram S., Iikubo Y., and Kudo A., Journal of Alloys and Compounds, **2007** 433(1-2) p. 237-240.

11. Wang R., Xin J.H., Yang Y., Liu H., Xu L., and Hu J., Applied Surface Science, **2004** 227(1-4) p. 312-317.

12. Li Q.H., Liang Y.X., Wan Q., and Wang T.H., Applied Physics Letters, **2004** 85(26) p. 6389-6391.

13. Gouvea C.A.K., Wypych F., Moraes S.G., DurÃ¡n N., Nagata N., and Peralta-Zamora P., Chemosphere, **2000** 40(4) p. 433-440.

14. Liqiang J., Baiqi W., Baifu X., Shudan L., Keying S., Weimin C., and Honggang F., Journal of Solid State Chemistry, **2004** 177(11) p. 4221-4227.

15. Wu J.-J. and Tseng C.-H., Applied Catalysis B: Environmental, **2006** 66(1-2) p. 51-57.

16. Seery M.K., George R., Floris P., and Pillai S.C., Journal of Photochemistry and Photobiology A: Chemistry, **2007** 189(2-3) p. 258-263.

17. Zheng Y., Zheng L., Zhan Y., Lin X., Zheng Q., and Wei K., Inorganic Chemistry, **2007** 46(17) p. 6980-6986.

18. Zheng Y., Chen C., Zhan Y., Lin X., Zheng Q., Wei K., and Zhu J., The Journal of Physical Chemistry C, **2008** 112(29) p. 10773-10777.

19. Wu J.Z., Tu J.P., Yuan Y.F., Ma M., Wang X.L., Zhang L., Li R.L., and Zhang J., Journal of Alloys and Compounds, **2009** 479(1-2) p. 624-628.

20. Alammar T. and Mudring A.-V., Journal of Materials Science, **2009** 44(12) p. 3218-3222.

21. Georgekutty R., Seery M.K., and Pillai S.C., Journal of Physical Chemistry C, **2008** 112(35) p. 13563-13570.

22. Karunakaran C., Rajeswari V., and Gomathisankar P., Solid State Sciences, **2011** 13(5) p. 923-928.

23. Zhang Y. and Mu J., Journal of Colloid and Interface Science, **2007** 309(2) p. 478-484.

24. Height M.J., Pratsinis S.E., Mekasuwandumrong O., and Praserthdam P., Applied Catalysis B: Environmental, **2006** 63(3-4) p. 305-312.

25. Karunakaran C., Rajeswari V., and Gomathisankar P., Journal of Alloys and Compounds, **2010** 508(2) p. 587-591.

26. Jin Y., Cui Q., Wang K., Hao J., Wang Q., and Zhang J., Journal of Applied Physics, **2011** 109(5) p. 053521.

27. Ahn B.D., Kang H.S., Kim J.H., Kim G.H., Chang H.W., and Lee S.Y., Journal of Applied Physics, **2006** 100(9) p. 093701-093701-6.

28. Larson A. C. and Dreele R.B.V., LANSCE, MS-H805, **1994** Los Alamos National Laboratory p. NM 87545.

29. Toby B., Journal of Applied Crystallography, **2001** 34(2) p. 210-213.

30. Kisi E.H. and Elcombe M.M., Acta Crystallographica Section C, **1989** 45(12) p. 1867-1870.

31. Singhal R.K., Samariya A., Xing Y.T., Kumar S., Dolia S.N., Deshpande U.P., Shripathi T., and Saitovitch E.B., Journal of Alloys and Compounds, **2010** 496(1-2) p. 324-330.

32. Tam K.H., Cheung C.K., Leung Y.H., Djurisic A.B., Ling C.C., Beling C.D., Fung S., Kwok W.M., Chan W.K., Phillips D.L., Ding L., and Ge W.K., The Journal of Physical Chemistry B, **2006** 110(42) p. 20865-20871.

33. Koudelka M., Monnier A., Sanchez J., and Augustynski J., Journal of Molecular Catalysis, **1984** 25(1-3) p. 295-305.

34. Jing L., Xu Z., Shang J., Sun X., Cai W., and Guo H., Materials Science and Engineering: A, **2002** 332(1-2) p. 356-361.

35. Sahu R.K., Ganguly K., Mishra T., Mishra M., Ningthoujam R.S., Roy S.K., and Pathak L.C., Journal of Colloid and Interface Science, **2012** 366(1) p. 8-15.

36. Thongsuriwong K., Amornpitoksuk P., and Suwanboon S., Journal of Sol-Gel Science and Technology, **2012** 62(3) p. 304-312.

37. Habibi M. and Sheibani R., Journal of Sol-Gel Science and Technology, **2010** 54(2) p. 195-202.

38. Arabatzis I.M., Stergiopoulos T., Bernard M.C., Labou D., Neophytides S.G., and Falaras P., Applied Catalysis B: Environmental, **2003** 42(2) p. 187-201.

39. Drelinkiewicz A., Hasik M., Quillard S., and Paluszkiewicz C., Journal of Molecular Structure, **1999** 511-512(0) p. 205-215.

40. Sui X., Liu Y., Shao C., Liu Y., and Xu C., Chemical Physics Letters, **2006** 424(4-6) p. 340-344.

41. Waterhouse G.I.N., Bowmaker G.A., and Metson J.B., Physical Chemistry Chemical Physics, **2001** 3(17) p. 3838-3845.

42. Wahab R., Ansari S.G., Kim Y.S., Seo H.K., Kim G.S., Khang G., and Shin H.-S., Materials Research Bulletin, **2007** 42(9) p. 1640-1648.

43. Yanhong L., Dejun W., Qidong Z., Min Y., and Qinglin Z., The Journal of Physical Chemistry B, **2004** 108(10) p. 3202-3206.

44. Jeong S.H., Park B.N., Lee S.B., and Boo J.H., Surface and Coatings Technology, **2007** 201(9â€“11) p. 5318-5322.

45. Sahu D.R., Microelectronics Journal, **2007** 38(12) p. 1252-1256.

46. Lany S. and Zunger A., Physical Review B, **2008** 78(23) p. 235104.

47. Lassaletta G., González-Elipe A.R., Justo A., Fernández A., Ager F.J., Respaldiza M.A., Soares J.C., and Da Silva M.F., Journal of Materials Science, **1996** 31(9) p. 2325-2332.

48. Sun T.J., Qiu J.S., and Liang C.H., Journal of Physical Chemistry C, **2008** 112(3) p. 715-721.

49. Wang J., Fan X.M., Zhou Z.W., and Tian K., Materials Science and Engineering B-Advanced Functional Solid-State Materials, **2011** 176(13) p. 978-983.

50. Dodd A., McKinley A., Saunders M., and Tsuzuki T., Journal of Nanoparticle Research, **2006** 8(1) p. 43-51.

CHAPTER 6

ROOM TEMPERATURE FERROMAGNETISM IN COPPER-DOPED ZnO NANOPARTICLES: STRUCTURAL, OPTICAL AND MAGNETIC PROPERTIES

6. 1 Introduction

There is an intense research interest on various transition metal (TM) doped semiconductor metal oxides given to their room temperature ferromagnetism (RTFM). These semiconductors referred as diluted magnetic semiconductors (DMSs) attract great attention for their potential applications in spintronics devices [1]. Most of the earlier work on DMSs has been on III-V type semiconductors, which have low solubility for TM [2, 3]. More recently, II-VI type TM-doped semiconductors have been explored, as they allow high dopant concentrations and exhibit potential in achieving magnetic ordering at around ambient temperatures [4, 5]. Among various II-VI type semiconductor metal oxides, ZnO has provoked great interest as a DMS due to its wide band gap (3.37 eV) and large exciton binding energy (60 meV) [6]. In addition, both the theoretical predictions and experimental studies indicated that TM-doped ZnO has RTFM property with a curie temperature above room temperature (300 K) [7, 8].

The role of the TM doping in ZnO based DMSs is of considerable significance because the origin of the RTFM was claimed to be based on two controversies; ferromagnetism (i) is an external property and comes from impurities like TM clusters [9, 10] or (ii) is an intrinsic property and originates from the spin-polarized carries [11, 12]. Therefore, many studies have been performed to elucidate the underlying mechanism for RTFM. Up to now, various TMs such as manganese [13], cobalt [14], and iron [15] have been doped into ZnO structure to achieve RTFM property. The major drawback of these

TM is that the dopant atoms can form clusters or precipitates directly affecting the ferromagnetic properties and such impurities impede the use of DMSs for spintronics applications [6]. Recently, researchers have focused on copper doped ZnO (ZnO:Cu) nanostructures [16-18] instead of traditional DMSs doped with other TMs since metallic copper is not magnetic, and neither Cu_2O nor CuO is ferromagnetic. However, the origin of the RTFM behavior of the ZnO:Cu is not well understood due to confliction between experimental and theoretical studies. Thus, it is important to clarify the nature of the RTFM with detailed experimental study.

The magnetic properties of the ZnO:Cu systems strongly depend on the synthesis procedure [19]. Hence, it is important to define the experimental parameters for obtaining particles with reproducible characteristics. In addition, a low temperature synthesis with simple procedure is desirable for the large-scale production. In the present work, room temperature synthesis of ZnO:Cu nanoparticles by precipitation is reported, based on our previous work for preparation of ZnO:Ag nanostructures [20]. The effect of Cu amount on the structural and magnetic properties of ZnO:Cu nanoparticles was investigated experimentally and the origin of the RTFM was discussed.

6.2 Experimental Methods

6.2.1 Materials

The chemicals used during synthesis of doped ZnO nanoparticles with Cu are listed in Table 6.1. All reagents were used without further purification. Ultrapure deionized (DI) water used during reactions was obtained by using Human Corporation Zeneer Power I water purification system.

Table 6.1. Materials used in the experimental part of the synthesis of Cu doped ZnO nanoparticles, their formulas and sources.

Material	Chemical Formula	Grade	Source
Zinc acetate dihydrate	$C_4H_6O_4Zn{\cdot}2H_2O$	99.5%, powder	Fluka
Copper (II) acetate monohydrate	$(CH_3COO)_2Cu.H_2O$	99%, powder	Merck
Polyvinyl pyrrolidone	$(C_6H_9NO)_n$	MW ~55000	Aldrich
Sodium hydroxide	NaOH	97%, pellets	Merck
Ethylene glycol	$C_2H_6O_2$	99%, solution	Merck

6.2.2 Experimental procedures

For synthesis of the ZnO:Cu nanoparticles, first a zinc-containing solution (0.1 M, 100 mL) was prepared by dissolving zinc acetate dihydrate in EG. This solution was added drop-wise into PVP solution (0.5 g PVP, in 100 mL EG) using an automated injection pump (Top-5300 model syringe pump) at a rate of 50 mL/h and stirred for 15 min. Then, 2 M $NaOH_{aq}$ was added (at a rate of 20 mL/h) into this mixture until the pH was reached to 12.7. In the same time, three 50 mL aqueous copper acetate solutions of varying concentration which is selected according to final solution composition corresponding to a Cu:Zn ratio of 1.25, 2.5 and 5 at. % Cu were prepared. Each Cu-solution was added into a separate zinc-containing parent solutions at a rate of 20 mL/h right after pH adjustment. Once injection was completed, the final solutions were homogenized for 15 min at 900 rpm. The powder products were collected by centrifugation at 10000 rpm (using Eppendorf 5805 model (Eppendorf AG, Hamburg, Germany)) for 10 min and subsequently washed thoroughly (five times) with DI-water. The powders were then dried at 70 °C for 3 h in a vacuum dryer and no further thermal treatment was performed. In addition to ZnO:Cu nanoparticles, pure ZnO nanoparticles were also synthesized according to the same experimental procedure, by substituting equal amount of pure DI-water (50 mL) for aqueous copper acetate solution. . A schematic representation of the experimental procedure are shown in Figure 6.1.

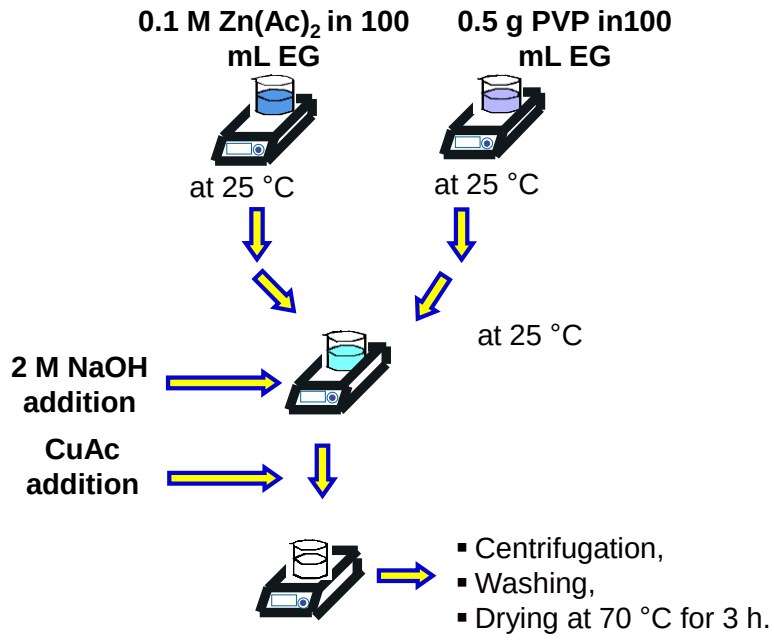

Figure 6.1. A schematic representation of experimental procedure for synthesis of Cu doped ZnO nanoparticles with precipitation method.

6.2.3 Materials characterization

The phase identification was conducted by x-ray diffraction (XRD) analyses using a Rigaku D/Max-2000 PC (Rigaku Corporation, Tokyo, Japan) diffractometer. Typical data acquisition was performed in a diffraction angle (2θ) range of 25-92° with a step size of 0.5°/min, using Cu-Kα radiation. The detailed crystal structure investigation was conducted by Rietveld refinement analyses using General Structural Software [21] with the EXPGUI graphical user interface [22].

The chemical identification and evaluation of the chemical state of the constituent elements were accomplished by x-ray photoelectron spectroscopy (XPS) analyses using a PHI 5000 VersaProbe (Physical Electronics, MN, USA). The quantitative analyses for chemical identification were performed using high-resolution scans of the Cu(2p), O(1s) and Zn(2p) spectral regions. The binding energies and charge corrections have been calibrated by taking the C(1s) line (285.0 eV) as reference.

JEOL 2100 F model (JEOL Ltd., Tokyo, Japan) transmission electron microscope (TEM) at an accelerating voltage of 200 kV was used to determine the size and morphology of the nanoparticles. The representative TEM samples were prepared simply by drying out ultrasonically dispersed aqueous powder suspensions on holey carbon coated copper grids.

The magnetic properties of the samples were investigated using a vibrating sample magnetometer (ADE Magnetics EV9, MicroSense LLC, MA, USA). All measurements were performed at room temperature with a maximum field of 4 kOe. Saturation magnetization and coercivity values of the each sample were obtained from the hysterisis curves.

The band gap values were determined based optical spectroscopy analyses performed using a double beam spectrophotometer (Cary100 Bio; Agilent Technologies Pty Ltd., Mulgrave, VIC, Australia) in a wavelength range of 250-800 nm. The powder samples were dispersed in DI water by 10 min ultrasonication. The background contribution was evaluated using DI-water as reference.

6.3 Results and Discussion

6.3.1 Crystal structure analyses and properties

The XRD analyses of the ZnO:Cu nanoparticles have been mainly employed in investigating the effects of Cu addition/incorporation on crystal structure of ZnO and in interpreting the relevant changes. Figure 6.2, 6.3, 6.4 and 6.5 show the XRD diffractograms of pure ZnO and 1.25, 2.5 and 5 at.% Cu doped ZnO:Cu nanoparticles, respectively. The XRD patterns match with wurtzite type ZnO crystal structure (JCPDS card no: 36-1451). These data indicate no trace for presence of any additional phase of copper, copper oxide(s) or any binary Zn-Cu phase. Although XRD technique has limited sensitivity for the detection of very small amount phases, it is reasonable to assume absence of secondary phases due to small Cu dopant amount lower than the solubility limit of Cu in ZnO as determined by others [23-25].

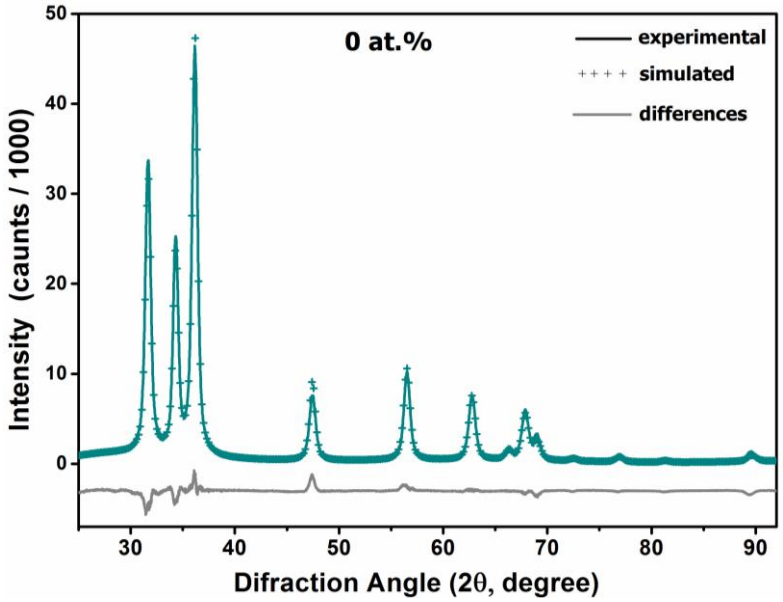

Figure 6.2. The experimental XRD diffractogram, Rietveld refinement simulation result and difference between experimental and simulated data of pure ZnO nanoparticles.

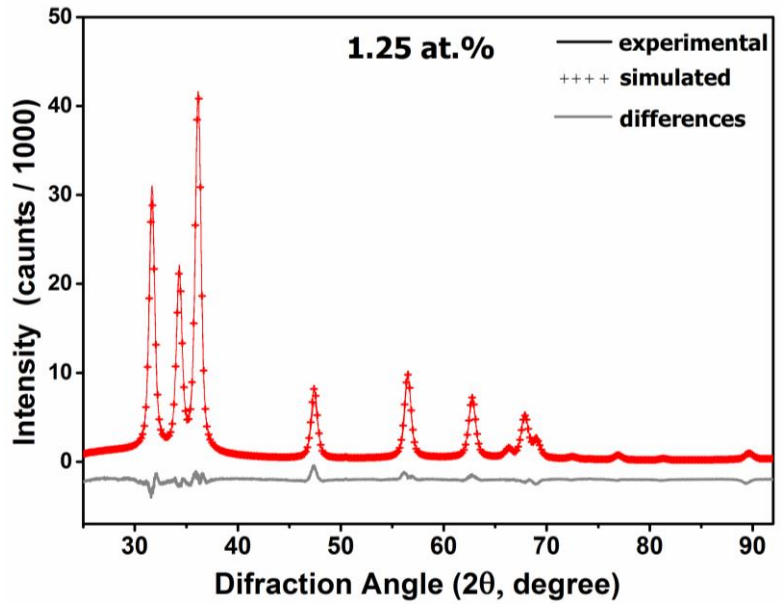

Figure 6.3. The experimental XRD diffractogram, Rietveld refinement simulation result and difference between experimental and simulated data of 1.25 at.% Cu doped ZnO:Cu nanoparticles.

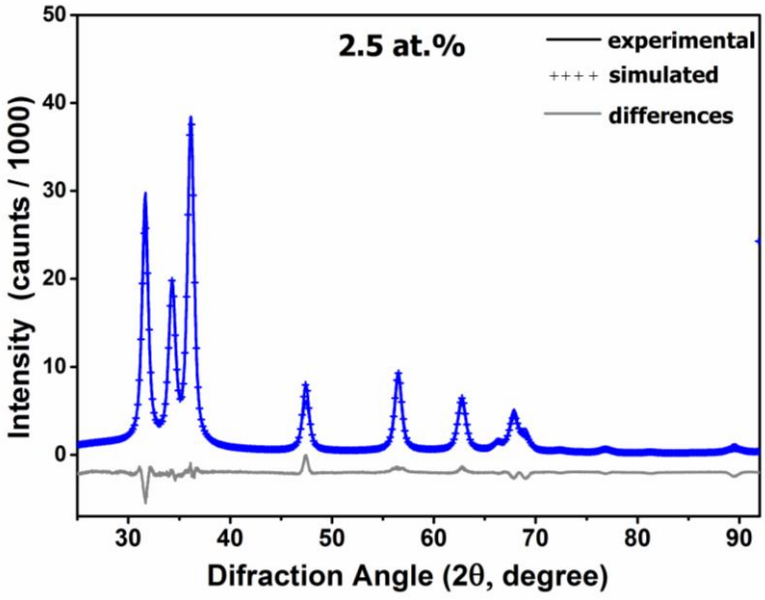

Figure 6.4. The experimental XRD diffractogram, Rietveld refinement simulation result and difference between experimental and simulated data of 2.5 at.% Cu doped ZnO:Cu nanoparticles.

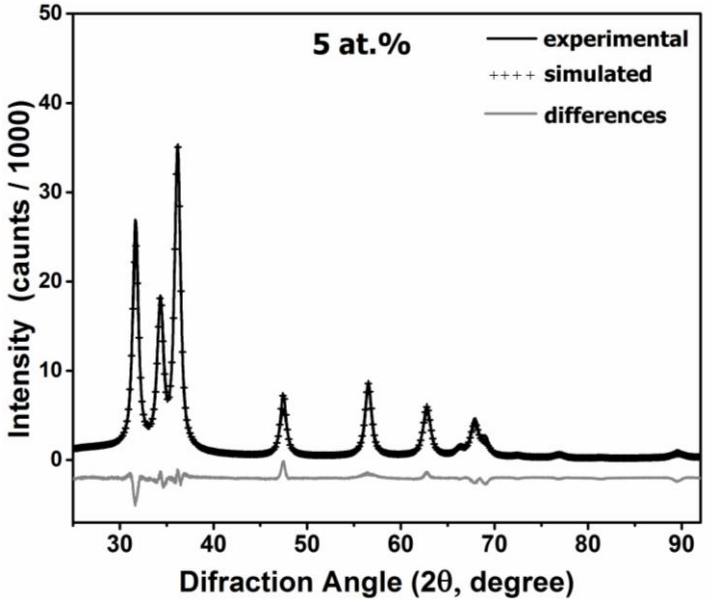

Figure 6.5. The experimental XRD diffractogram, Rietveld refinement simulation result and difference between experimental and simulated data of 5 at.% Cu doped ZnO:Cu nanoparticles.

Figure 6.2, 6.3, 6.4 and 6.5 also indicate the results of Rietveld refinements of pure and Cu- doped ZnO nanoparticles. The diffractogram for each sample is composed of two overlapping sets; the actual experimental data, R_{exp}, presented with solid lines and also the simulated counterpart, R_{wp}, obtained from the Rietveld refinement indicated with cross signs. The gray-colored patterns (on the bottom) show the differences between the experimental data and simulated results of the Rietveld analyses. R_{exp} and R_{wp} values for all samples are listed in Table 6.2. The Chi-squared values, X^2 ($X^2=(R_{wp}/R_{exp})^2$), were obtained as 1.34, 1.40, 1.45 and 1.42; for pure, 1.25, 2.5 and 5 at.% Cu incorporated ZnO powders. The low R factors and X^2 figures at around a value of 1 suggest that refinements are relatively reliable [26]. All the diffraction events for ZnO nanoparticles fit to that of with wurtzite structure confirming $P6_3mc$ space group with atomic position of (1/3, 2/3, 0) for Zn and (1/3, 2/3, 0.3817) for O, respectively [27].

As shown in the Figure 6.6 the full width at half maximum (FWHM) of the diffraction peaks increase with Cu addition, meanwhile the peak positions slightly shift to higher 2θ values. The 2θ positions for $(10\bar{1}1)$ diffractions extracted from Figure 6.6 are listed in the Table 6.2. For ZnO:Cu particles with increasing Cu amount, a 2θ shift in the range 0.02-0.04° was observed. Table 6.2 also lists the precise figures for the lattice parameter (c) as determined by the Rietveld refinement analyses. The lattice parameters decrease with Cu doping and reach a minimum value of 5.20 Å in the case of the 5 at.% Cu- dopted sample, which is 5.26 Å for pure ZnO. A change in the lattice size with Cu substitution is expected due the ionic size differences between Cu (Cu^{2+}: 0.57Å) and Zn (Zn^{2+}: 0.60Å) ions for the same coordination (four-fold coordination) [28]. Thus, the Rietveld refinement results are in good agreement with the conventional XRD data and relevant interpretations indicate a possible lattice *contraction* due to selective/specific substitution of Cu^{2+} with Zn^{2+} in the lattice as also reported by others [24, 29].

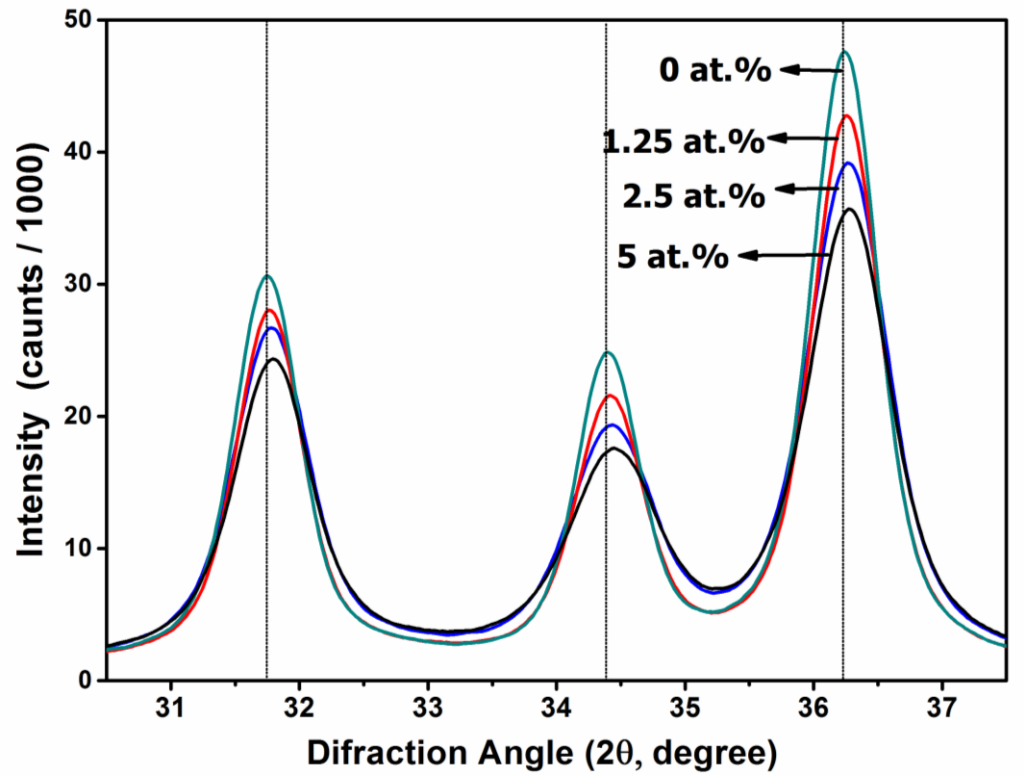

Figure 6.6. Enlarged region (2θ=30.5-37.5) of the experimental XRD diffractograms of pure ZnO and ZnO:Cu nanoparticles with different Cu contents (1.25, 2.5 and 5 at.% Cu).

The Rietveld refinement analyses of XRD data also allow determination of quantitative occupancy values for Zn sites. The percent occupancy values of Zn sites were listed in the Table 6.2. The calculated Zn occupancy values were slightly lower than the theoretical values. The marginal differences between initially available Cu content and actual substitution extent suggest that most of the Cu ions in solution readily substitute into ZnO during precipitation of ZnO crystals.

Table 6.2. R_{exp} and R_{wp} values, $(10\bar{1}1)_{ZnO}$ peak positions, lattice parameters (c), Zn occupancy values, XRD crystallite size obtained from Rietveld analyses and average crystalline size determined from TEM analyses for pure ZnO and ZnO:Cu nanoparticles with different Cu contents (1.25, 2.5 and 5 at.% Cu).

Cu:Zn ratio (at.%)	**R_{exp}-R_{wp} (%)**	**$(10\bar{1}1)_{ZnO}$ Peak Position* (degree of 2θ)**	**Lattice Parameter (c, Å)**	**Occupancy, Zn (%)**	**XRD Crystallite Size (nm)**	**TEM Particle Size (nm)**
0	5.58-7.50	36.25	5.26	100	20.9	17.3 ± 2.5
1.25	5.56-7.78	36.27	5.25	99.2	19.6	17.1 ± 2.7
2.5	5.58-8.07	36.28	5.21	98.3	16.8	16.1 ± 2.5
5	5.59-7.94	36.29	5.20	96.8	13.7	13.9 ± 2.5

***:** $(10\bar{1}1)$ *peak position of JCPDS card of ZnO (36-1451).*

The deviation in the occupancy values is more significant for higher amount of Cu-containing precipitation formulations, suggesting an increasing yet certainly limited incorporation of the copper ions into Zn^{2+} sites with the higher amount of the Cu addition. Both experimental [30] and theoretical [31] studies indicate that substitution of Cu^{2+} ions into ZnO lattice is more favorable than that of Cu^{1+} and Cu^{0}, as there would not be any change in the net charge upon substitution of Cu^{2+} for Zn^{2+} for stoichiometric ZnO. Furthermore, Ye et al. proposed that Cu has a tendency to occupy the Zn sites in the crystal structure, instead of interstitial positions [11]. Therefore, substitutional incorporation of Cu occurs with replacement of host Zn^{2+} with Cu^{2+} ions.

The average crystallite size for the ZnO nanoparticles estimated by Rietveld refinements are also presented in the Table 6.2. The particle size decreases from 20.9 nm (pure ZnO) to 13.7 nm in the case of 5 at.% Cu dopıng. A decrease in the crystallite size with increasing Cu content is probably due to the change in the precipitation mechanism in the presence of excessive Cu ions.

6.3.2 Microstructural analyses and properties

Figure 6.7 shows low magnification TEM micrographs of ZnO nanoparticles. All ZnO nanoparticles have equiaxed/spherical morphology. The average particle sizes determined from TEM analyses (given in Table 6.2) are agreement with the crystallite sizes obtained from Rietveld refinement. High-resolution TEM images of selected ZnO nanoparticle(s) are shown in Figure 6.8. The fringes of individual planes are clearly visible in the micrographs suggesting the single crystal nature for ZnO nanoparticles. The lattice spacing values of pure ZnO and ZnO:Cu nanoparticles are also shown in Figure 6.8. The spacing between adjacent fringes was measured as 0.281 nm for pure ZnO nanoparticles which is in good proximity for the interplanar spacing of $(10\bar{1}0)$. The spacing between adjacent fringes of the ZnO:Cu samples were measured as 0.278, 0.276 and 0.273 nm for the 1.25, 2.5 and 5 at.% Cu-added ZnO:Cu samples, respectively. This indicates a lattice contraction due to replacement of smaller sized Cu^{2+} with Zn^{2+}.

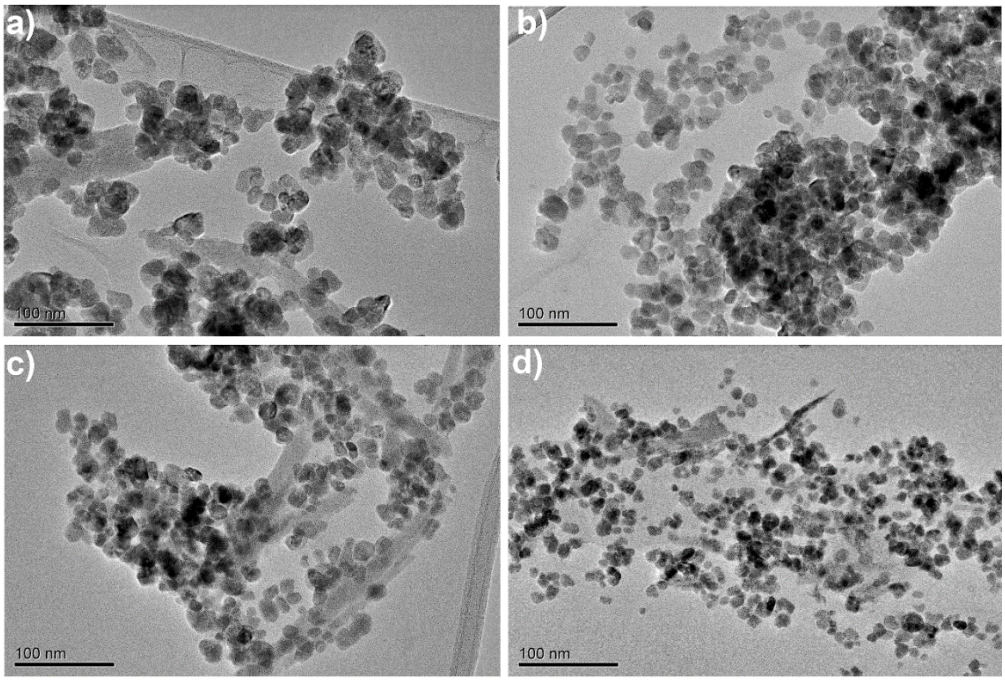

Figure 6.7. The low magnification TEM images of pure ZnO and ZnO:Cu nanoparticles with different Cu contents (1.25, 2.5 and 5 at.% Cu).

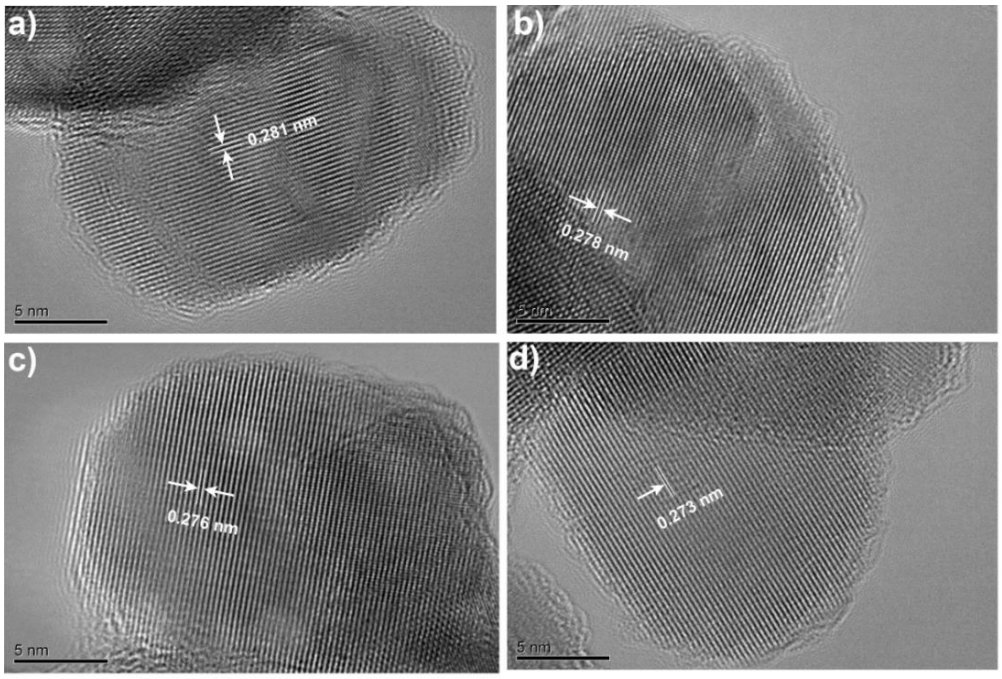

Figure 6.8. The high resolution TEM images of pure ZnO and ZnO:Cu nanoparticles with different Cu contents (1.25, 2.5 and 5 at.% Cu).

6.3.3 Chemical analyses and properties

The chemical composition and chemical state of the constituents for ZnO:Cu nanoparticles were investigated by XPS analyses. The survey spectra of pure ZnO and ZnO:Cu nanoparticles are shown in Figure 6.9. The major signals for pure ZnO nanoparticles were assigned to Zn, O and C elements and no signal for other element was detected. The low intensity C signal is most likely due to remaining PVP or simply due to the adsorption of organic contaminants during handling. In the survey spectra of the ZnO:Cu samples, additional signals for Cu(2*p*) were detected.

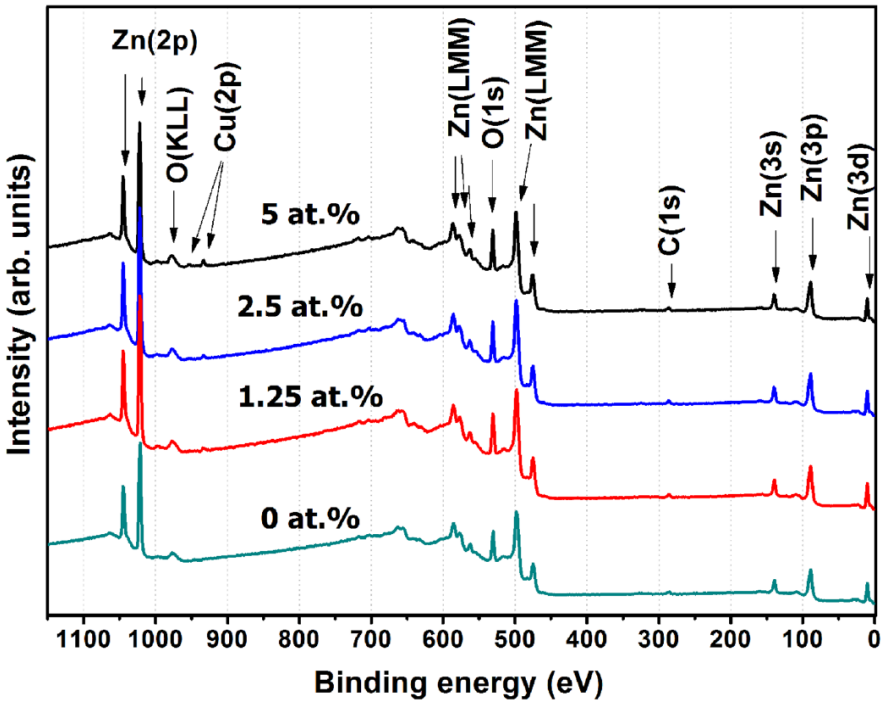

Figure 6.9. Survey analyses of XPS spectra for pure ZnO and ZnO:Cu nanoparticles with different Cu contents (1.25, 2.5 and 5 at.% Cu).

The informative spectral positons of the survey analyses of Cu(2*p*), Zn(2*p*) and O(1*s*) regions are also presented with the accompanying high resolution regional spectra in Figure 6.10, 6.11 and 6.12, respectively. The corresponding binding energies (BE) in eV for the Cu(2*p*), Zn(2*p*) and O(1*s*) signals determined from the high resolution scans are summarized in Table 6.3.

The details of high resolution Cu(2*p*) signals (Figure 6.10) provide additional insights about the chemical state of Cu in ZnO lattice. The XPS can clearly distinguish the state of Cu due to measurable differences in BE of the signals for metallic and ionic entities. Metallic Cu (Cu^0) produces a sharp well-defined Cu($2p_{3/2}$) and Cu($2p_{1/2}$) signals centering at 932.6 eV and 952.5 eV, respectively. Monovalent Cu (Cu^{1+}) produces also sharp and well-defined Cu(2*p*) signals centering at the same BE values, but slightly narrower signal peak widths. Meanwhile, divalent Cu ion (Cu^{2+}) characteristically exhibit considerably broader Cu(2*p*) signals with an ~1.0 eV shift to higher BE and centering at 933.6 eV and 953.5 eV for Cu($2p_{3/2}$) and Cu($2p_{1/2}$), respectively [32-34]. The high resolution XPS spectra of ZnO:Cu, with Cu($2p_{3/2}$) and Cu($2p_{1/2}$) signals corresponding that of Cu^{2+} oxidation state, indicate that Cu is mainly incorporated as Cu^{2+}. Furthermore, the positions of Cu(2*p*) signals shift toward the higher BE's values with the increasing Cu addition. This can be explained with a decrease in Cu–O bond separation as a result of lattice parameter change with increasing dopant amount.

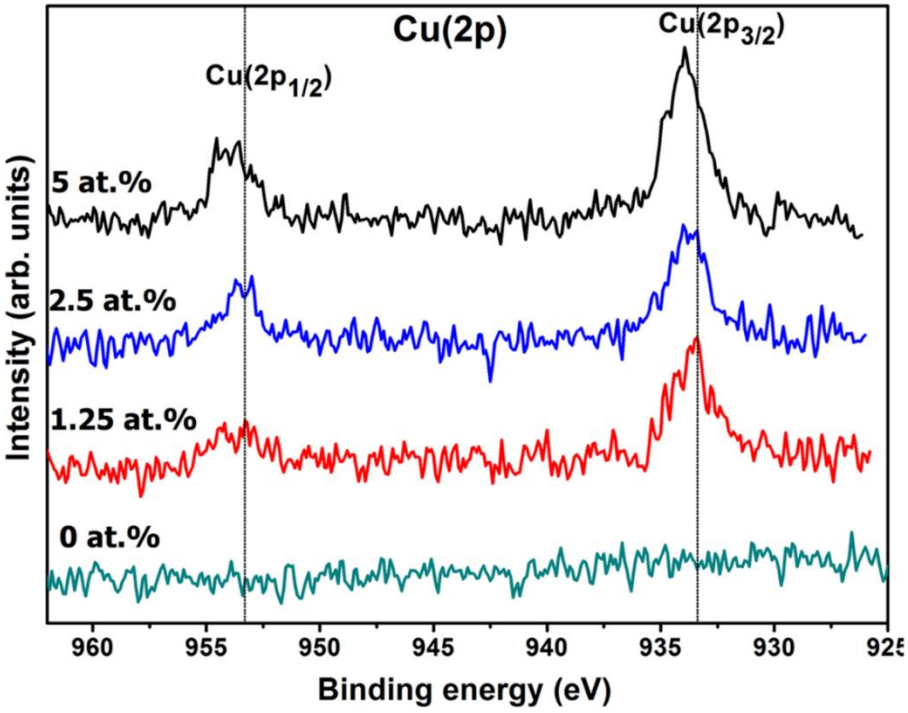

Figure 6.10. High resolution regional XPS spectra of Cu(2p) signals for pure ZnO and ZnO:Cu nanoparticles with different Cu contents (1.25, 2.5 and 5 at.% Cu).

Figure 6.11 shows the features of Zn(2*p*) signal for all samples. For pure ZnO nanoparticles, Zn($2p_{3/2}$) and Zn($2p_{1/2}$) signals, originating from strong spin orbit coupling, appear at 1021.19 and 1044.21 eV, respectively. These energy values well agree with the previously reported BE values for stoichiometric ZnO [35]. The positions of these signals shift slightly to higher BE values for ZnO:Cu nanoparticles. This change can be analyzed/explained by considering the differences in O(1*s*) signal characteristics for pure and Cu-doped ZnO as shown in Figure 6.12. The O(1*s*) signals were deconvoluted using Gaussian fit with XPS PEAK41 software. For pure ZnO, the lower BE side of the O(1*s*) signal centering at 529.91 eV is attributed to lattice oxygen ions neighboring with Zn^{2+} ions in the hexagonal ZnO lattice. The higher BE component of the O(1*s*) signal centering at 531.51 eV is associated with either presence of loosely bound oxygen or the chemisorbed oxygen, such as surface hydroxyl groups [36]. The O(1s) BE values are also in agreement with the those reported for stoichiometric ZnO [37].

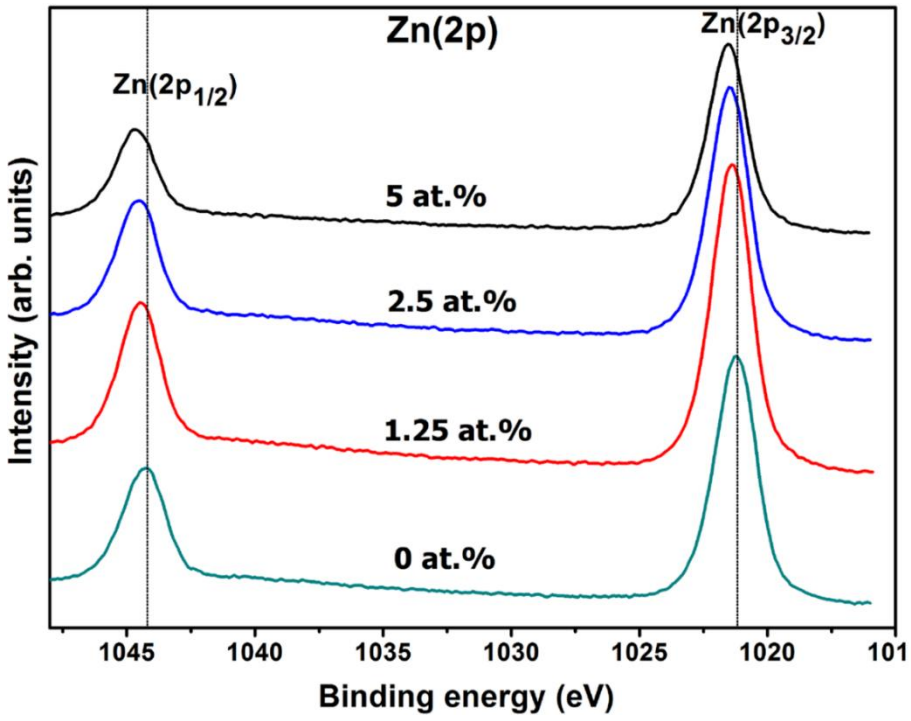

Figure 6.11. High resolution regional XPS spectra of Zn(2p) signals for pure ZnO and ZnO:Cu nanoparticles with different Cu contents (1.25, 2.5 and 5 at.% Cu).

For Cu-containing ZnO nanoparticles; the lower BE O(1*s*) signal is attributed to lattice oxygen neighbors with Zn^{2+} or Cu^{2+} ions. This signal appears at relatively higher BE values than pure ZnO, as can be seen by the vertical drop line placed in Figure 6.12 for visual aid and also by BE values listed in the Table 6.3. This positional shift may be due to change in the ionic character of O–X bonds (X=Zn^{2+} for pure ZnO, and X=Zn^{2+} or Cu^{2+} for Cu-incorporated ZnO) originating from electronegativity difference for the specific ion associating with oxygen. According to the Paulings principle, the negativity difference of a Cu–O bond is smaller than that of a Zn–O bond [38]. Therefore, in presence of Cu, the relatively poor ionic association of Cu–O pairs compared those for Zn–O bonds results in a higher valance electron density [35]. As a result of higher valance electron density with increasing Cu amount, enhanced electron transfer from conduction band of ZnO to 3*d* band level of Cu provide BE of Zn(2*p*) and O(1*s*) signals shift towards to higher value.

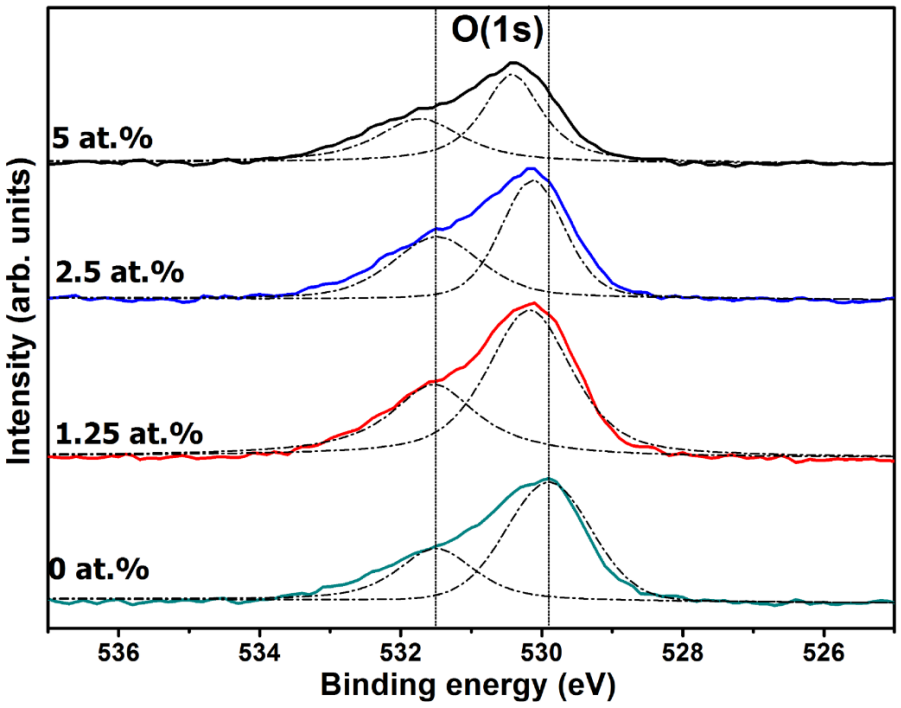

Figure 6.12. High resolution regional XPS spectra of O(1s) signals for pure ZnO and ZnO:Cu nanoparticles with different Cu contents (1.25, 2.5 and 5 at.% Cu).

Therefore, the chemical shift in the BE of Zn(2*p*) and O(1*s*) signals to higher energy values with increasing Cu addition also support the extensive substitution of Cu^{2+} ions into ZnO lattice and in agreement with the Rietveld refinement results.

Table 6.3. Binding energy values (in eV) of Cu($2p_{3/2}$), Cu($2p_{1/2}$), Zn($2p_{3/2}$), Zn($2p_{1/2}$) and O(1s) (lattice and chemisorbed oxygen) for pure ZnO and ZnO:Cu nanoparticles with different Cu contents (1.25, 2.5 and 5 at.% Cu).

Cu:Zn ratio (at.%)	**Binding energy (eV)**					
	Cu ($2p_{3/2}$)	**Cu ($2p_{1/2}$)**	**Zn ($2p_{3/2}$)**	**Zn ($2p_{1/2}$)**	**O (1*s*)***	**O (1*s*)****
0	-	-	1021.19	1044.21	529.91	531.51
1.25	933.46	953.21	1021.32	1044.32	530.08	531.58
2.5	933.69	953.36	1021.45	1044.46	530.13	531.61
5	933.92	954.16	1021.58	1044.58	530.37	531.74

* *: lattice oxygen, ** : chemisorbed oxygen*

6.3.4 Magnetic analyses and properties

Magnetization *vs.* magnetic field (M-H) curves of ZnO:Cu nanoparticles are shown in Figure 6.13. The diamagnetic terms arising from the sample holder have been subtracted in plotting these loops. M-H curves of ZnO:Cu nanoparticles indicate that RTFM ordering with distinct S shaped hysteresis loops. It is well known that pure ZnO nanoparticles exhibit diamagnetic property at room temperature [39]. Therefore, the observed RTFM can be attributed to incorporation of Cu ions into ZnO structure. Although the coercivity (H_c) values for all Cu-doped ZnO nanoparticles were nearly same, the saturation magnetization (M_s) values increase with increasing doped Cu amount. M_s and H_c values for ZnO:Cu samples are given in Table 6.4. The largest M_s value was observed as 0.862 μ_B/Cu for 5 at.% Cu doped sample. This value is higher than previously reported experimental values [40], but smaller than the theoretically calculated value, 0.96 μ_B/Cu [41].

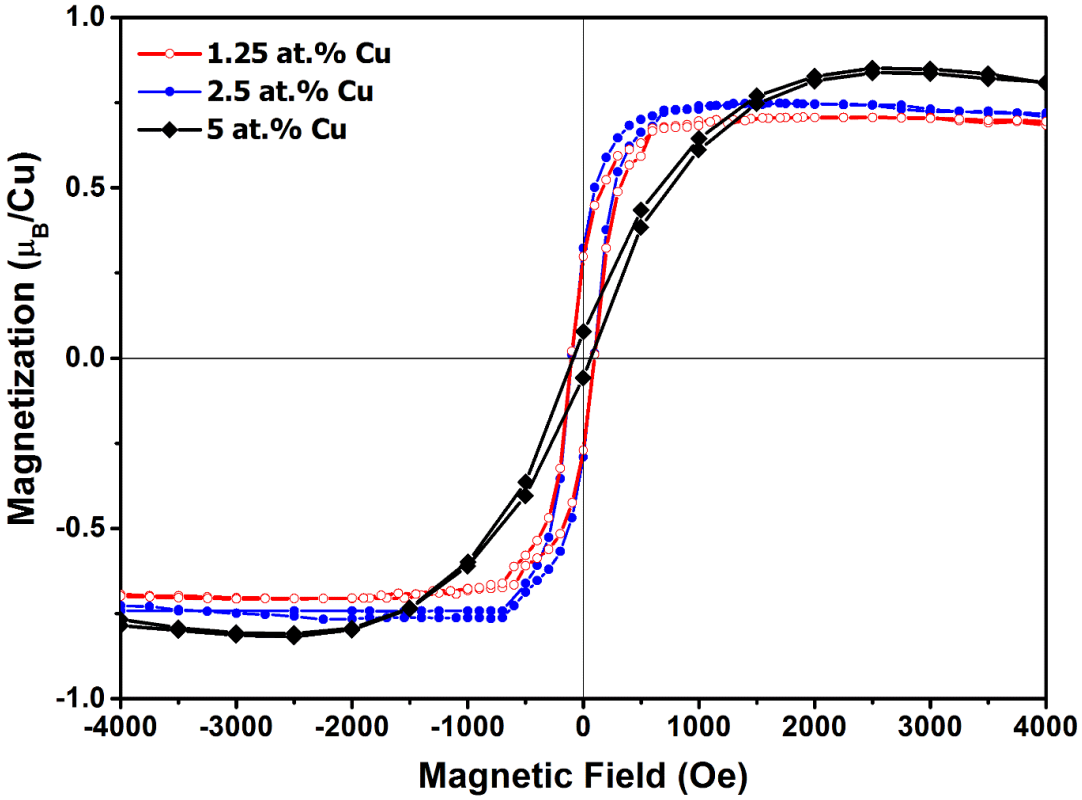

Figure 6.13. M-H curves of ZnO:Cu nanoparticles with different Cu contents (1.25, 2.5 and 5 at.% Cu).

Table 6.4. Saturated magnetization (M_s) and coercive fields (H_c) for pure ZnO and ZnO:Cu nanoparticles with different Cu contents (1.25, 2.5 and 5 at.% Cu).

Cu:Zn ratio (at.%)	Saturated magnetization (M_s, μ_B/Cu)	Coarcive fields (H_c, Oe)
1.25	0.637	100
2.5	0.716	100
5	0.862	90

The reason of the RTFM for transition metal-doped DMSs still remains controversial in the relevant literature. The discussion is mainly on the origin of ferromagnetism; whether it is origination from the magnetic interactions between the dopant atoms, or due to the intrinsic behavior of dopant atoms present in the ZnO lattice. In regard to the former possibility, although theoretical predictions support that Cu atoms tend to occupy well-separated positions in ZnO crystal [11], some experimental investigations report the formation of Cu precipitates or clusters with increasing Cu amount. In this case, antiferromagnetic matchup between Cu pairs destroys the ferromagnetic ordering and results lower magnetic moments [5, 42]. However, the result of current study indicated an increase in M_s value upon Cu doping. Similar findings have been also reported for Co- and Mn-doped ZnO nanostructures [8, 43]. Therefore, in our study, formation of the Cu clusters is not observed even at highest amount of the Cu addition (here 5 at.% Cu). The analytical finding of this study- XRD and TEM- confirmed that Cu ions do not form any clusters or additional phases, and copper doping takes place by ionic substitution of Cu into ZnO crystal. This means that the distance between adjacent magnetically active ions in all Cu-incorporated ZnO samples is still in the range of ferromagnetic ordering. The conservation of short range magnetic ordering through the magnetic interaction provides improvement of the RTFM with higher amount of Cu addition. Thus, the apparent ferromagnetic nature of the ZnO:Cu nanoparticles does not seem to commence due the magnetic interactions of the dopants atoms.

6.3.5 Optical analyses and properties

The main objective of this work was to draw a conclusion for the origin of RTFM in ZnO:Cu systems. All findings in this study suggest that RFTM behavior is due substitutional incorporation of Cu^{2+} ions in the ZnO lattice. In that respect, the electronic configuration and related band gap information ZnO:Cu becomes a critical piece of information. Figure 6.14 shows UV-Vis absorption spectra for pure and Cu-incorporated ZnO. All spectra exhibit the absorption band which is characteristic to wurtzite type ZnO crystal. The absorption spectrum of pure ZnO has distinct absorption band edge at 340 nm. However, the positions of absorption band edge of ZnO:Cu

particles change with increasing Cu amount and show red shift to higher wavelength. An important consequence of the red shift in the absorption band edge is the reduction in the direct band gap energies (E_g) of ZnO nanoparticles. E_g values of ZnO nanoparticles are obtained by plotting the absorption coefficient (α)–photon energy (hυ) graph and extrapolating the straight-line portion of this plot to the hυ axis shown as an inset in the Figure 6.14. For pure ZnO, Eg was determined as 3.341 eV and it decreases to 3.276, 3.268, and 3.256 eV for the samples incorporated with 1.25, 2.5 and 5 at.% Cu, respectively. A smaller E_g value with increasing Cu incorporation is somewhat contradictory with particle size characteristics, which found to be decrease with increasing Cu amount.

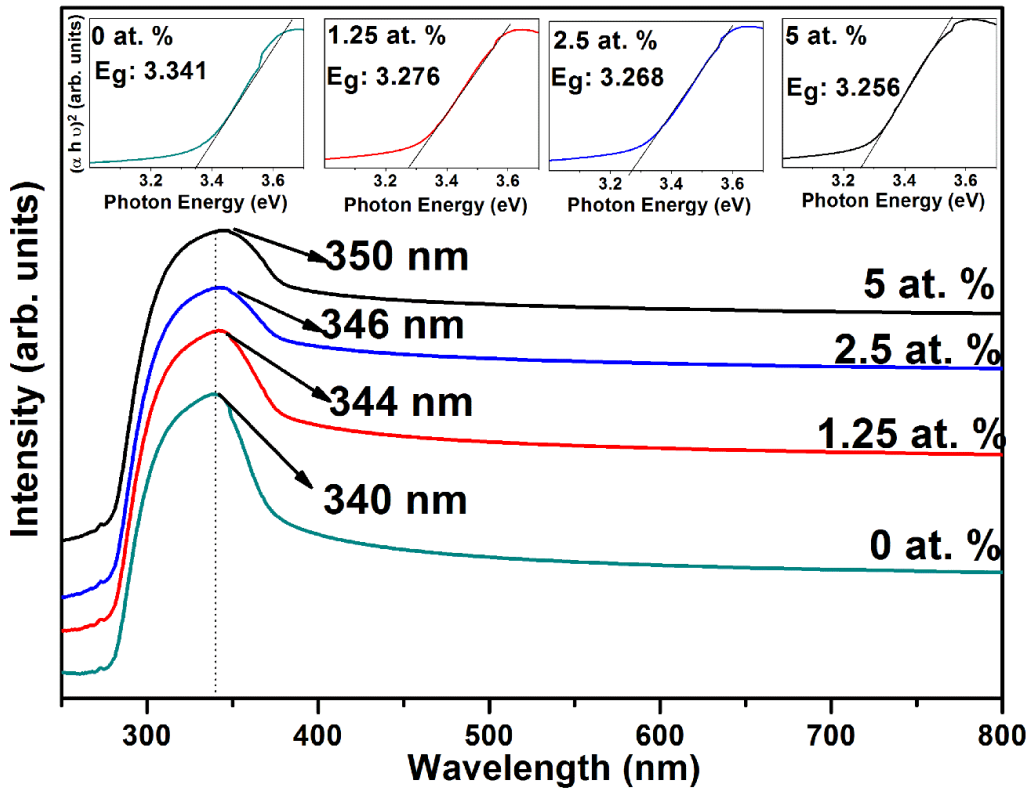

Figure 6.14. The UV-Vis spectra of pure and Cu incorporated ZnO nanoparticles with different Cu contents (1.25, 2.5 and 5 at.% Cu). Band edge locations of samples are also given in the figure. The insets in Figure show plots of $(\alpha h\upsilon)^2$ as a function of photon energy (E_g) for all samples.

The red shift in the absorption band edge so E_g values of the ZnO nanostructures is associated with decreasing conduction band energy of ZnO by exchange interaction of the conduction band electrons of ZnO and localized d electrons of Cu [44-46]. With the half full shell electronic configuration ($3d^9$, $4s^0$), Cu^{2+} ions form an impurity level, which is located near the Fermi level and just below the conduction band of ZnO. This impurity level behaves as a deep acceptor and provides carrier transformation of non-equilibrium holes or electrons by hybridization of O(2*p*) bands electrons with half full Cu(3*d*) electrons. The observed E_g narrowing as a result of the *sp-d* spin exchange interactions confirms substitution of Cu^{2+} ions into ZnO crystal structure. Therefore, they result in the formation of bound magnetic polarization and so responsible for RTFM behavior [44, 47]. From the all above analyses, it can be concluded that Cu^{2+} ions substitute into the ZnO lattice and change the crystal and band structures of host ZnO by varying incorporated Cu amount. As a summary, RTFM property in ZnO:Cu nanoparticles is supposed to be intrinsic behavior due to sp-d spin carrier exchange interaction.

6.4 Conclusions

Pure and Cu-doped ZnO nanoparticles were synthesized through a simple room temperature precipitation technique. The effects of the Cu amount on the crystal structural, microstructural and magnetic properties of the ZnO nanoparticles have been reported. The results indicated that the Cu doping occurs by substitutional incorporation of Cu^{+2} ions in the ZnO lattice as revealed by extensive crystallographic analyses of the XRD data by Rietveld refinement. The chemical state analysis by XPS also supports such chemical modification in the ZnO structure. The magnetic measurements showed that Cu addition obviously enhances RTFM property of ZnO nanoparticles. In addition to a reduction of the absorption band edge, smaller band gap energies were observed for Cu-doped ZnO, evidenced by optical spectroscopy. According RTFM seems to be an intrinsic behavior and it is due to substitution of Cu^{2+} into ZnO crystal. This work describes a correlation between crystal and band structure, and RTFM behavior of the ZnO nanostructures.

6.5 References

1. Wolf S.A., Awschalom D.D., Buhrman R.A., Daughton J.M., von Molnar S., Roukes M.L., Chtchelkanova A.Y., and Treger D.M., Science, **2001** 294(5546) p. 1488-1495.

2. Koshihara S., Oiwa A., Hirasawa M., Katsumoto S., Iye Y., Urano C., Takagi H., and Munekata H., Physical Review Letters, **1997** 78(24) p. 4617-4620.

3. Ohno H., Science, **1998** 281(5379) p. 951-956.

4. Dietl T., Ohno H., Matsukura F., Cibert J., and Ferrand D., Science, **2000** 287(5455) p. 1019-1022.

5. Buchholz D.B., Chang R.P.H., Song J.H., and Ketterson J.B., Applied Physics Letters, **2005** 87(8) p. 082504-3.

6. Pearton S.J., Heo W.H., Ivill M., Norton D.P., and Steiner T., Semiconductor Science and Technology, **2004** 19(10) p. R59-R74.

7. Shuai M., Liao L., Lu H.B., Zhang L., Li J.C., and Fu D.J., Journal of Physics D: Applied Physics, **2008** 41(13) p. 135010.

8. Sharma P., Gupta A., Rao K.V., Owens F.J., Sharma R., Ahuja R., Guillen J.M.O., Johansson B., and Gehring G.A., Nature Materials, **2003** 2(10) p. 673-677.

9. Shim J.H., Hwang T., Lee S., Park J.H., Han S.-J., and Jeong Y.H., Applied Physics Letters, **2005** 86(8) p. 082503-082503-3.

10. Kane M.H., Shalini K., Summers C.J., Varatharajan R., Nause J., Vestal C.R., Zhang Z.J., and Ferguson I.T., Journal of Applied Physics, **2005** 97(2) p. 023906-6.

11. Ye L.-H., Freeman A.J., and Delley B., Physical Review B, **2006** 73(3) p. 033203.

12. Ueda K., Tabata H., and Kawai T., Applied Physics Letters, **2001** 79(7) p. 988-990.

13. Muthukumaran S. and Gopalakrishnan R., Journal of Materials Science: Materials in Electronics, **2012** 23(7) p. 1393-1401.

14. Bylsma R.B., Becker W.M., Kossut J., Debska U., and Yoder-Short D., Physical Review B, **1986** 33(12) p. 8207-8215.

15. Yu X., Meng D., Liu C., Xu K., Chen J., Lu C., and Wang Y., Journal of Materials Science: Materials in Electronics, **2014** 25(9) p. 3920-3923.

16. Hou D.L., Ye X.J., Meng H.J., Zhou H.J., Li X.L., Zhen C.M., and Tang G.D., Appl. Phys. Lett., **2007** 90 p. 142502.

17. Owens F.J., Gladczuk L., Szymczak R., Dluzewski P., Wisniewski A., Szymczak H., Golnik A., Bernhard C., and Niedermayer C., Journal of Physics and Chemistry of Solids, **2011** 72(6) p. 648-652.

18. Owens F.J., Journal of Magnetism and Magnetic Materials, **2009** 321(22) p. 3734-3737.

19. Pearton S.J., Norton D.P., Ivill M.P., Hebard A.F., Zavada J.M., Chen W.M., and Buyanova I.A., Journal of Electronic Materials, **2007** 36(4) p. 462-471.

20. Yildirim O.A., Unalan H.E., and Durucan C., Journal of the American Ceramic Society, **2013** 96(3) p. 766-773.

21. Larson A. C. and Dreele R.B.V., LANSCE, MS-H805, **1994** Los Alamos National Laboratory p. NM 87545.

22. Toby B., Journal of Applied Crystallography, **2001** 34(2) p. 210-213.

23. Singhal S., Kaur J., Namgyal T., and Sharma R., Physica B: Condensed Matter, **2012** 407(8) p. 1223-1226.

24. Shukla G., Applied Physics A, **2009** 97(1) p. 115-118.

25. Thakur P., Bisogni V., Cezar J.C., Brookes N.B., Ghiringhelli G., Gautam S., Chae K.H., Subramanian M., Jayavel R., and Asokan K., Journal of Applied Physics, **2010** 107(10).

26. Toby B.H., Powder Diffraction, **2006** 21(1) p. 67-70.

27. Kisi E.H. and Elcombe M.M., Acta Crystallographica Section C, **1989** 45(12) p. 1867-1870.

28. Shannon R., Acta Crystallographica Section A, **1976** 32(5) p. 751-767.

29. Zhang Z., Yi J.B., Ding J., Wong L.M., Seng H.L., Wang S.J., Tao J.G., Li G.P., Xing G.Z., Sum T.C., Alfred Huan C.H., and Wu T., The Journal of Physical Chemistry C, **2008** 112(26) p. 9579-9585.

30. Klier K., Applications of Surface Science, **1984** 19(1-4) p. 267-297.

31. Rodriguez J.A. and Campbell C.T., The Journal of Physical Chemistry, **1987** 91(27) p. 6648-6658.

32. Poulston S., Parlett P.M., Stone P., and Bowker M., Surface and Interface Analysis, **1996** 24(12) p. 811-820.

33. Xing G.Z., Yi J.B., Tao J.G., Liu T., Wong L.M., Zhang Z., Li G.P., Wang S.J., Ding J., Sum T.C., Huan C.H.A., and Wu T., Advanced Materials, **2008** 20(18) p. 3521-3527.

34. Liu H.L., Yang J.H., Zhang Y.J., Wang Y.X., Wei M.B., Wang D.D., Zhao L.Y., Lang J.H., and Gao M., Journal of Materials Science: Materials in Electronics, **2009** 20(7) p. 628-631.

35. Futsuhara M., Yoshioka K., and Takai O., Thin Solid Films, **1998** 322(1-2) p. 274-281.

36. Mass J., Bhattacharya P., and Katiyar R.S., Materials Science and Engineering: B, **2003** 103(1) p. 9-15.

37. Jing L., Xu Z., Shang J., Sun X., Cai W., and Guo H., Materials Science and Engineering: A, **2002** 332(1-2) p. 356-361.

38. Pauling L., 3d ed. The George Fisher Baker non-resident lectureship in chemistry at Cornell University. **1960**, Ithaca, N.Y.: Cornell University Press. p. 644 p.

39. Xu Q., Zhou S., and Schmidt H., Journal of Alloys and Compounds, **2009** 487(1–2) p. 665-667.

40. Herng T.S., Lau S.P., Yu S.F., Yang H.Y., Ji X.H., Chen J.S., Yasui N., and Inaba H., Journal of Applied Physics, **2006** 99(8).

41. Chien C.H., Chiou S.H., Guo G.Y., and Yao Y.D., Journal of Magnetism and Magnetic Materials, **2004** 282 p. 275-278.

42. Hou D.L., Ye X.J., Meng H.J., Zhou H.J., Li X.L., Zhen C.M., and Tang G.D., Applied Physics Letters, **2007** 90(14).

43. Cheng X.M. and Chien C.L., Journal of Applied Physics, **2003** 93(10) p. 7876-7878.

44. Elilarassi R. and Chandrasekaran G., Journal of Materials Science: Materials in Electronics, **2010** 21(11) p. 1168-1173.

45. Xu C.X., Sun X.W., Zhang X.H., Ke L., and Chua S.J., Nanotechnology, **2004** 15(7) p. 856-861.

46. Ullah R. and Dutta J., Journal of Hazardous Materials, **2008** 156(1–3) p. 194-200.

47. Furdyna J.K., Journal of Applied Physics, **1988** 64(4) p. R29-R64.

CHAPTER 7

CONCLUSIONS

Low temperature routes for synthesis of ZnO nanostructures with size and morphology control have been presented. Synthesis of ZnO nanostructures was carried out using different aqueous routes; microemulsion and precipitation techniques. The effect of processing parameters on the physical, structural and optical properties of ZnO nanostructures were examined. Functional properties of nanostructures were improved by ion incorporations into ZnO structure. The general findings of the thesis are summarized as followings;

7.1 Synthesis of ZnO nanoparticles via microemulsion method

ZnO nanoparticles were synthesized by a reverse microemulsion system formed from sodium bis(2-ethylhexyl) sulfosuccinate (AOT):glycerol:n-heptane. The zinc precursor was zinc acetate dihydrate. The formation of ZnO nanoparticles was achieved by calcination of premature zinc glycerolate microemulsion product in air at various calcination temperatures. Microemulsion products were characterized using XRD, TG-DSC, SEM and PL spectroscopy. The results showed that both surfactant concentrations in the initial microemulsion formulation and the calcination temperature influenced the morphology and size of the ZnO nanoparticles. The surfactant concentration –AOT– in the initial microemulsion formulation and the calcination temperature influenced the morphology and size of the ZnO nanoparticles. Low surfactant concentrations (5:5:90, AOT:glycerol:n-heptane, wt.%) lead to formation of spherical ZnO nanoparticles, whose average particle size changed from 15±1 nm (300 °C) to 24±1 nm (500 °C), increasing with calcination temperature, while preserving their spherical morphology at all temperatures. Microemulsion system containing higher surfactant amount (30:5:65, AOT:glycerol:n-heptane, wt.%)

resulted in rod-like ZnO nanostructures after calcination at 300 °C and 400 °C, with a radius of 22±3 and 28±1 nm; and with a length of 66±3 nm and 72±1 nm. Further increase in the calcination temperature to 500 °C initiated a rod-to-sphere shape transformation of the ZnO nanoparticles produced using this particular microemulsion formulation. For all ZnO microemulsion products, the photoluminescence measurements suggested a high defect concentration degenerated at higher calcination temperature. Optical characterization also implied a chemically activated surface for ZnO nanoparticles.

7.2 Low temperature synthesis of ZnO nanoparticles via precipitation method

Synthesis of ZnO nanoparticles was also achieved by low temperature precipitation method. The precipitation system was formed using zinc acetate dihydrate as zinc source, ethylene glycol (EG) as solvent and polyvinyl pyrrolidone (PVP) as chelating agent. Precipitation products were characterized using XRD, SEM, TEM, FTIR, PL and UV-Vis spectroscopy. The effects of processing parameters including precipitation temperature (25, 60, 70 and 80 °C), amount of chelating agent (0.2, 0.3 and 0.4 g PVP) and solvent type (EG or DI-water) on the size and morphology of resultant ZnO nanoparticles are reported. The size of spherical ZnO nanoparticles was manipulated by the choice of precipitation temperature (13.0±1.9 nm at 25 °C and 9.0±1.3 nm at 80 °C), which essentially changes the nature of adsorption events between ZnO crystals and organic molecules. The particle size can also be regulated by the amount of chelating agent (13.0±1.9 nm in 0.2 g PVP and 5.3±0.3 nm in 0.4 g PVP) as a result of further enhancement in adsorption between ZnO crystals and organic additives. A change in morphology of ZnO nanostructures from spherical to isosceles triangle was observed when different solvent was employed; specifically, by substituting DI-water for EG which has different adsorption ability. Accordingly, a formation and growth mechanism for size and morphology controlled ZnO nanoparticles by low temperature aqueous precipitation routes have been proposed.

7.3 Room temperature synthesis of Ag-doped ZnO nanoparticles: structural, optical and photocatalytic properties

Synthesis of functionalized ZnO nanoparticles (silver-doped, ZnO:Ag) was also performed through room temperature precipitation method without any subsequent thermal treatment. ZnO nanoparticles were characterized by XRD, TEM, XPS, FTIR and UV-Vis spectroscopy. Detailed crystallographic investigation was accomplished through Rietveld refinement. The effect of silver content on structural and optical properties of resultant ZnO nanoparticles has been investigated. It was found that silver doping results in positional shifts for the XRD peaks and the absorption band edge of ZnO. These were attributed to the substitutional incorporation of Ag^{+} ions into Zn^{2+} sites within the ZnO crystal. It was found that silver incorporation resulted in the substitutional incorporation of Ag^{+} ions into Zn^{2+} sites within the ZnO crystal. In addition, the photocatalytic activity of the ZnO:Ag nanoparticles was determined by methylene orange (MO) degradation studies and compared to that of undoped ZnO. The complete decomposition of MO dye was achieved after 90 min of UV irridation for 0.3 at. % Ag incorporated sample, while this time decreased to 60 min for 1.0 at. % Ag incorporated ZnO nanostructures. Improved photocatalytic activity was obtained for ZnO:Ag nanoparticles. It has been shown that an optimum amount of silver dopant (1 at.% Ag) is required to obtain maximum photocatalytic activity. Moreover, higher silver incorporation resulted in smaller size for ZnO nanoparticles (19.14±2.92 nm in 0.3 at.% Ag, 18.02±3.02 nm in 1.0 at.% Ag and 14.24±1.67 nm in 8.0 at.% Ag).

7.4 Room temperature ferromagnetism in Cu-doped ZnO nanoparticles; structural, optical and magnetic properties

ZnO nanoparticles were also functionalized with copper (Cu) to achieve room temperature ferromagnetic behavior (RTFM). Cu-doped ZnO (ZnO:Cu) nanoparticles with various Cu concentration (Cu:Zn ratio at.% of 1.25, 2.5 and 5) were synthesized by room temperature precipitation method without any subsequent post thermal treatment. Pure ZnO nanoparticles were also synthesized for direct structural and

property-related comparison purposes. ZnO:Cu nanoparticles were thoroughly characterized by XRD, XPS, TEM, VSM and UV-Vis spectroscopy. Detailed crystallographic investigation was accomplished through Rietveld refinement. The evidences for substitutional incorporation of Cu^{2+} ions into ZnO lattice have been demonstrated with the positional changes in the XRD data of ZnO and accompanying precise lattice parameter analyses by Rietveld refinement. XPS analyses revealed incorporation of copper as Cu^{2+} ions. Magnetization measurements performed by VSM showed an enhanced RTFM for ZnO:Cu nanoparticles in the presence of higher amount of Cu. RTFM of ZnO nanostructures was attributed to the substitutional incorporation of Cu^{2+} ions and so narrowing band gap of ZnO. M_s value of ZnO:Cu nanoparticles increases with Cu amount (M_s: 0.637 for 1.25 at.% Cu, 0.716 for 2.5 at.% Cu and 0.862 for 5.0 at.% Cu). These results suggest that RTFM characteristics is an intrinsic property of ZnO:Cu nanoparticles. In addition, particle size of ZnO:Cu nanoparticles decreases with Cu dopant amount (17.01±2.7 nm in 1.25 at.% Cu, 16.1±2.5 nm in 2.5 at.% Cu and 13.9±2.5 nm in 5.0 at.% Cu).

CURRICULUM VITAE

PERSONAL INFORMATION

Surname, Name: ALTINTAŞ YILDIRIM, Özlem
Nationality: Turkish (TC)
Date and Place of Birth: 20 October 1979, Ankara
Marital Status: Married
Phone: +90 312 210 2521
Fax: +90 312 210 2518
e-mail: altintas@metu.edu.tr

EDUCATION

2013-2014 Visiting Scientist in Materials Science Division, Argonne National Laboratory, Il, USA.

2006-2014 PhD Student, Integrated PhD, -Metallurgical and Materials Engineering, Middle East Technical University

1. GPA of 3.43/4.00
2. Thesis title: *Synthesis of zinc oxide nanoparticles by aqueous methods and effect of metal incorporation on the structural/functional properties of nanoparticles*" Supervisor: Prof. Dr. C. Durucan

2003–2005 M.S. – Department of Chemistry, Selçuk University

1. GPA of 89.62/100
2. Thesis title: *Removal of nitrate from water*, Supervisor: Prof. Dr. Y. Çengeloğlu.

1999-2003 B.S.– Department of Chemistry, Selçuk University

GPA of 3.09/4.00

PUBLICATIONS

1. **O.A. Yildirim** and C. Durucan, "*The origin of room temperature ferromagnetism in copper-doped zinc oxide (ZnO:Cu) nanoparticles*"in preperation.
2. **O.A. Yildirim,** Yuzi Liu, and Amanda K Petford-Long, "*Facile synthesis of zinc oxide (ZnO) nanonail structure*" in preparation.
3. **O.A. Yildirim,** Yuzi Liu, and Amanda K Petford-Long, "*Synthesis of uniformly distributed single- and double-sided zinc oxide (ZnO) nanocombs*" submitted to Langmuir.
4. **O.A. Yildirim,** H.E. Unalan and C. Durucan, "*Highly Efficient Room Temperature Synthesis of Silver-Doped Zinc Oxide (ZnO:Ag) Nanoparticles: Structural, Optical, and Photocatalytic Properties*", (2013) Journal of the American Ceramic Society, 96 (3), 766-773.
5. **O.A. Yildirim** and C. Durucan, "*Effect of precipitation temperature and organic additives on size and morphology of ZnO nanoparticles*" (2012) Journal of Materials Research, 27 (11), 1452-1461 (*Cover Article*).
6. **O.A. Yildirim** and C. Durucan, "*Synthesis of zinc oxide nanoparticles elaborated by microemulsion method*" (2010) Journal of Alloy and Compounds, 506, 944-949.
7. **O. Altintas**, A. Tor, Y. Cengeloglu, M. Ersoz "*Removal of nitrate from the aqueous phase by Donnan dialysis*" (2009) Desalination, 239, 276-282.

ABSTRACTS & PROCEEDINGS

1. **O.A. Yildirim** and C. Durucan, "S*ilver-added ZnO nanoparticles: synthesis and assesment of photocatalytic activity*", 16th International Metallurgy & Materials Congress (IMMC 2012), UCTEA Chamber of Metallurgical Engineers, 13-15 September 2012, Istanbul, Turkey, Congress e-Book, pp 1091-1097.
2. **O.A. Yildirim** and C. Durucan, "*Synthesis of zinc oxide nanoparticles by microemulsion method and effect of microemulsion formulation on particle morphology*", 15th International Metallurgy & Materials Congress (IMMC 2010), UCTEA Chamber of Metallurgical Engineers, 11-13 November 2010, Istanbul, Turkey, Congress e-Book, pp 92-99.

3. **O.A. Yildirim** and C. Durucan, "*Çinko oksit nano parçacıkların çökeltme tekniği kullanılarak düşük sıcaklıklarda sentezlenmesi*", 13th International Materials Symposium (IMSP 2010), Pamukkale University Engineering Faculty, 13-15 October 2010, Denizli, Turkey, Proceedings of 13th International Materials Symposium, pp. 342-347.
4. **O.A. Yildirim** and C. Durucan, *Low temperature Synthesis of Zinc Oxide (ZnO) Nanoparticles by Precipitation*, 6th Nanoscience and Nanotechnology Conference on (NANOTR-VI), IZTECH Izmir Institute of Technology, 15-18 June 2010, Izmir, Turkey, Abstract Book, p 4.
5. **O. Altintas** and C. Durucan, "*Synthesis of morphologically controlled ZnO nanoparticles by microemulsion technique*", 13th International Metallurgy & Materials Congress (IMMC 2008), UCTEA Chamber of Metallurgical Engineers, 16-18 October 2008, Istanbul, Turkey, Congress e-Book, pp 729-737.
6. **O. Altintas** and C. Durucan, "*Development of ZnO nanoparticle doped coatings on textiles*", 3rd International Technical Textiles Congress, 1-2 Dec. 2007, İstanbul, Turkey, Proceedings of 3rd International Technical Textiles Congress, pp. 391-398.
7. **O. Altintas** and C. Durucan, "*Low temperature synthesis of zinc oxide (ZnO) nanoparticles by precipitation method*", International Conference on Nanostructures Materials, 13-17 Sep. 2010, Roma, Italy, Abstract Book, p. 180.
8. **O. Altintas** and C. Durucan, "*Synthesis of Size and Morphology Controlled Zinc Oxide (ZnO) Nanoparticles*", Materials Research Society Symposium Proceedings Series (2008) Boston MA, USA, pp 68.
9. **O. Altintas** and C. Durucan, "*Synthesis of Size- and Morphology-controlled ZnO Nanoparticles by Microemulsion Techniques*", Somer Symposium Series,14-15 May 2007 Ankara, Turkey, Abstract Booklet of Somer-M-29, p.66.

AWARD

1. 14th International Metallurgy and materials Congress (2008) Istanbul, TURKEY Young Researcher Award (Synthesis of Morphologically Controlled ZnO Nanoparticles by Microemulsion Technique).

SCHOLARSHIPS

2007–2011 The Scientific and Technological Research Council of Turkey, TUBITAK, National Scholarship Programme for PhD Students.